Experimental Evaluation of JP-8-Based Fire Resistant Fuels

Jason Michael Salyer Dress

Thesis submitted to the faculty of the Virginia Polytechnic Institute and State University in partial fulfillment of the requirements for the degree of

Master of Science
In
Mechanical Engineering

Uri Vandsburger
Brian Y. Lattimer
Shi-Hau Own

November 30th, 2010
Blacksburg, VA

Keywords: Fire Resistant Fuel, Rotary Atomization, Calorimetry, Dynamometer

Experimental Evaluation of JP-8-Based Fire Resistant Fuels

Jason Michael Salyer Dress

ABSTRACT

The Army's Fire Resistant Fuel (FRF) program is currently being used to defend against the threat of vehicle fuel fires resulting from unconventional warfare encountered in the Middle East. Fire Resistant Fuels are based upon JP-8, which is now the primary fuel for the Army ground services. The goal of FRF development is to reduce susceptibility to ignition at standard storage conditions while still serving as a fuel for the Army's diesel vehicles.

Two preliminary tests were conducted to narrow down a field of candidates developed by Luna Innovations to a final set of five FRF. Dynamometer testing was used to determine peak power of the supplied Yanmar 2V750 engine. Fuel fire resistance characteristics were defined and compared using a rotating disk anti-misting characterization system. Fuels were characterized based upon spray characteristics including velocity and droplet diameter as well as through ignition testing. For these tests, FRF were compared to Diesel and Jet-A results.

Results from this testing has shown that two fuels, both JP-8 emulsions, met the basic criteria of a fire resistant fuel. Engine testing trends showed that both fuels surpassed the peak power output of Diesel. Rotary atomization ignition testing resulted in no ignition for both fuels.

As a supplementary study, cone calorimetry testing was performed to determine effective heats of combustion. Results from experimentation demonstrated that the energy content of the FRF is not of primary importance to engine performance or flame resistance. All data, analysis and trends are located in the appendices.

Dedication

This thesis is dedicated to my friends and family, who have provided me with the inspiration to continue my education as well as the much needed support during this adventure. I would, in particular, like to dedicate this thesis to three very special and influential people in my life: my parents, whose support and wisdom have been invaluable, and to Emily who has been extremely understanding, caring and a constant source of inspiration through this whole process.

Acknowledgements

I would like to begin my acknowledgements by thanking Dr. Uri Vandsburger, Dr. Shi-Hau Own and Army TARDEC program monitor Joel Schmitigal for the opportunity to work on this project. It has been a privilege to work on such an interesting subject, while understanding its importance to our nation's armed forces. Since joining the Virginia Tech Combustion Dynamic Systems Laboratory in June 2009, I instantly felt welcome and impressed with the other researchers and projects within the lab.

There are several colleges and friends from within the lab who played a pivotal role in completing this project that I would like to thank. Without their help, the completion of this project would not have been possible. I'd like to thank Steve, Jordan and Chris for being a seemingly infinite source of knowledge and guidance, their unyielding willingness to help, and the countless hours of assistance in the lab.

Dr. Brian Lattimer, a professor at Virginia Tech, a committee member and head of the Extreme Laboratory at the University, has been instrumental in completing calorimeter testing. I want to thank him for letting me use his equipment for this testing as well as for all of his guidance and support during this project.

I would like to acknowledge and thank Brad, Emily, Craig, Jill, Patrick, and Nick for all of their assistance in setting up and running experiments. It should be noted that all images were taken or developed by the author unless otherwise stated.

My graduate experience would definitely not have been the same without my friends. I'd like to extend an acknowledgement to Brad, David, Emily, Jill, Craig, Patrick, Ryan, Jordan and Dragan who have definitely helped to make graduate school a unique experience.

I would lastly like to acknowledge all of the Mechanical Engineering Department machine shop workers who helped to create parts needed for this project. Without their help and their quick turnaround of parts, this project could not have been completed.

Table of Contents

List of Figures

List of Tables

Chapter 1 - Introduction

This chapter provides information on the background, motivation, research deliverables and objectives of this experimentation. The research motivation section will discuss the background of the Army's Fire Resistant Fuel program as well as need for this experimentation. The research deliverables and objectives section will discuss the required end results of this testing, expected outcomes as well as the testing approach for this experimentation.

Research Motivation

Fuel fires in combat vehicles have been a longstanding and difficult problem encountered by the United States Armed Forces. Begun in the 1980's, the United States Army's Fire Resistant Fuel Research (FRF) program initiated development of fire resistant fuel's for army combat vehicles. Initial efforts focused on formulations involving halogenated additives, anti-misting additives, emulsified fuels as well as water-in-fuel emulsions. The latter approach proved the most successful, certain technical as well as logistical issues needed to be resolved before the FRF formulation was to be field tested. By 1987 there was less need to continue research and development of fire resistant fuels, and the program was terminated.

With the United States entrance in the war in the Middle East, the threat of combat vehicle fuel fires has increased once again. Combined, the natural operation of the compression ignition combat vehicles along with the environmental conditions of the Middle East cause the steady state fuel temperatures to rise above their flash point in the fuel tank. The flash point of a fuel is the temperature at which the fuel will ignite and remain burning. The ignition of the fuel requires an ignition source. The unconventional warfare experienced in both Iraq and Afghanistan, which involves the use of Improvised Explosive Devices (IED), could provide such an ignition source potentially resulting in a disastrous fuel fire. In an effort to minimize the effects of the unconventional warfare on their combat vehicles, the Army re-instituted the FRF program beginning in May 2006.

Current efforts to develop fire resistant fuels are focus on JP-8, which is now the primary fuel for most Army ground combat vehicles as directed by DoD Directive 4140.43 for "Fuel Standardization."

Luna Technology Development Division, a division of Luna Innovations Inc., a research and development company based in Roanoke, VA, assists government agencies with their technological developments of, among other things, flame retardant additives. The company received the U.S. Army contract W56HzV-09-C-0033 to develop the FRF based upon three primary criteria; the fuel must be operable in a compression ignition engine, the fuel must display fire resistance characteristics in combat situations and the fuel must be based on JP-8 so that it may be replicated in the field.

The Virginia Tech Combustion Dynamic Systems Laboratory has been contracted by Luna Innovations to conduct testing of the developed fuels. The research focuses on evaluating sample fire resistant fuels based on performance in a compression ignition engine as well as on fire resistant ability. Collected data will support a recommendation for further testing and potential field implementation of a developed fire resistant fuel formulation.

Research Objectives

Due to the nature of the subject, there has been limited information regarding experimental evaluation of fire resistant fuel, especially newly developed versions based on JP-8. Jet-A was used for this testing instead of JP-8 due to its availability as well as the fact that both fuels have very similar properties, such as flash point and energy content. The purpose and primary goal of this research is to provide an assessment of developmental fire resistant fuels and recommendations as to predicted performance in field situations.

Within this goal, there are two primary objectives to complete and deliver to Luna Innovations. The first is to evaluate the FRF candidates as alternative fuels to JP-8 in the field. Since a majority of the vehicles used by the Army have diesel engines, performance tests will be conducted on a small-scale diesel engine. The second objective of this research is to evaluate the FRF on fire resistance. Fire resistance is a very complex term and a very complex problem to address. For the purpose of this experimentation, fire resistant fuels will attempt to susceptibility to ignition at standard storage pressure and temperature. It should be noted that the fuels tested are not fire proof and ultimately, if enough activation energy is applied to these fuels, they will ignite. In order to achieve the project goal and the primary objectives, a comparative study was designed and implemented. This study was comprised of a set of research objectives:

1. Perform preliminary bench-scale testing on first generation developmental fuel candidates. This was used to evaluate performance of fire resistant fuel development approaches. Testing was performed in two stages: Linear propagation testing and swirl flow-stabilized combustion testing. Linear flame propagation rate testing was used as a quantitative measure of each sample fuel's fire resistance potential. Next swirl stabilized combustion tests were designed and run to qualitatively assess each sample fuel's performance in low pressure combustion situations. For each test, the sample FRF results were compared to those of Jet A and Diesel.

2. Perform cone calorimeter testing to determine effective heats of combustion of selected fuels. This will provide supplemental information towards understanding results from other testing.

3. Engine performance testing: Dynamometer testing was designed and performed to place a Yanmar 2V750 compression ignition engine under load. For each fuel, engine torque and power outputs at a set engine rpm level.

4. Fire resistance testing: A rotary atomization testing apparatus was constructed in accordance with Naval Research Laboratory standards in order to test each sample FRF for fire resistance. Modifications were made to the system and testing of the fuels was completed in two stages; spray atomization characterization and fuel ignition characterization.

It should be noted that a fundamental study of these fuels has not been conducted, and the purposes of this experimentation is to apply practical small-scale techniques to compare the FRF to known fuels such as Diesel and Jet-A.

Chapter 2 - Fuel Propagation

Introduction

Propagation testing was conducted as the first half of a preliminary comparison study between various Luna sample fuels and established fuels such as Diesel and Jet-A. This testing was used to determine the linear flame propagation for each fuel, which is the time taken for a flame to travel a fixed path and a set distance. The linear flame propagation rate is a property that is used as a bench-scale test for distinguishing between the relative resistance to ignition of each fuel. The testing of the linear flame propagation rate allowed for a quick and effective means of determining and removing ineffective sample fuels. Ineffective fuels were deemed as having an equivalent or faster linear flame propagation rate as Jet-A. This shake down test provided Luna Innovations with quick feedback as to preliminary success or failure of their FRF developmental approaches. The results for this testing were interpreted by Luna Innovations for use in fuel selection and future fuel generation development and will not be presented in this paper. This testing was used to reduce the number of potential FRF candidates from over forty down to six, to be tested in the swirl flow combustor.

Nomenclature

Symbol	Units	Description
d	mm	The distance between the thermocouples
t	sec	Time interval between the peak temperatures of the two thermocouples

Test Setup

The testing setup and procedures for these experiments conformed to ASTM standard D5306-92 for linear flame propagation rate of lubricating oils and hydraulic fluids [1]. This testing setup can be seen in Figure 1. The base of the testing apparatus is an eighth inch steel frame, which allows the flame to propagate across the string without interference. A ceramic fiber string is

soaked with fuel and used as a means of linear flame propagation. In order to keep the string taught, a weight is placed at each end and allowed to hang from the side of the metal frame. The soaked string, with weights attached at each end, is centered across the long side of the metal frame. Lastly, two thermocouples are placed at set distances along the string length and just above the string body in order to track the flame speed as it propagates.

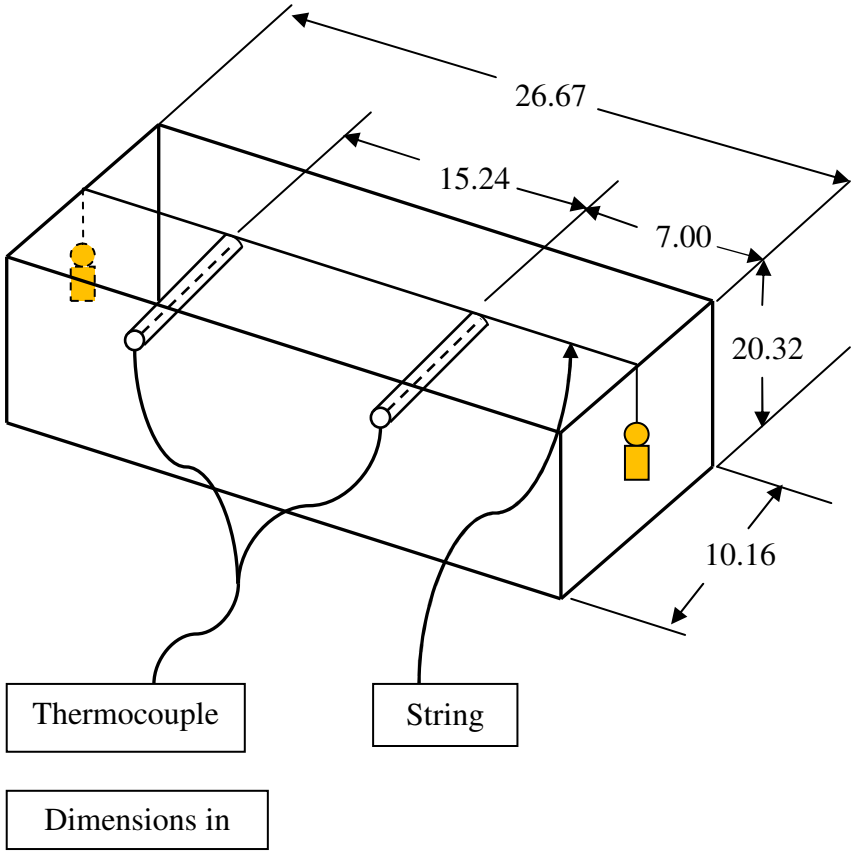

Figure 1. ASTM testing apparatus design for linear flame propagation rate experiment.

Procedure

Tests began by soaking a piece of clean ceramic fiber string in a pool of the fuel. After allowing the fiber string to soak for one minute, it was removed from the fuel and the excess fuel was then removed. The string was then placed over the metal testing frame and made taught with two weights. Thermocouples were set at distances along the string path according to Figure 1. Each test began with a baseline reading of ambient temperature of around the thermocouples for one minute. The string was then lit and the flame propagated along the fuel path to the opposite end

of the string. The data was then analyzed and the propagation rate was calculated using Equation 1.

$$linear\ flame\ propagation\ rate = \frac{d}{t} \quad (1)$$

Results and Conclusions

Several initial fuels were tested and many of them proved to have slower linear propagation rates than Jet-A, and are thus slower burning than Jet-A. Select fuels were chosen to move forward with testing. Those fuels are 737P077, 737P070, 737P183, 767P002, 767P024, 767P028, 737P084 and 737P053.

Chapter 3 - Swirl-Stabilized Combustion

Introduction

The second half of the preliminary bench-scale testing was the swirl flow-stabilized combustion test. This was a qualitative test that determined whether or not sample FRF could obtain and maintain steady-state combustion under low pressure conditions. For this comparative study, Diesel was used as a baseline result. Six sample fire resistant fuels were tested and compared to baseline fuels for visual stability, including fuel ignition, flame sputtering, flame color and flame duration .The six Luna sample fuels were determined using the linear propagation test; 737P077, 737P070, 737P183, 767P002, 767P024 and 767P028.

Test Setup

The testing apparatus used for this experiment has been designed for low pressure atomization and combustion of each fuel. Figure 2 shows the overall layout of the testing setup. Fuel and nozzle air are both supplied to the air assist atomizer used to break up the fuel into droplets. Swirl flow air is supplied into a set of guide vanes around the atomizer to stabilize the flow. To further clarify the term low pressure, the internal pressure of the system near the nozzle exit was on the order of 4 psi ± 1psi depending on the flow of fuel and air input. The volumetric flow rates of nozzle air and fuel were on the order of fractions of a gallon per hour. As seen in Figures 3, 4 and 5, the combustor is designed with both air and fuel input lines to the nozzle as well as a separate swirl air flow. Each input air flow is regulated independently and measured through volumetric flow meters downstream of the control knobs. The flow meter's signals are input to a data acquisition card and monitored on LabView.

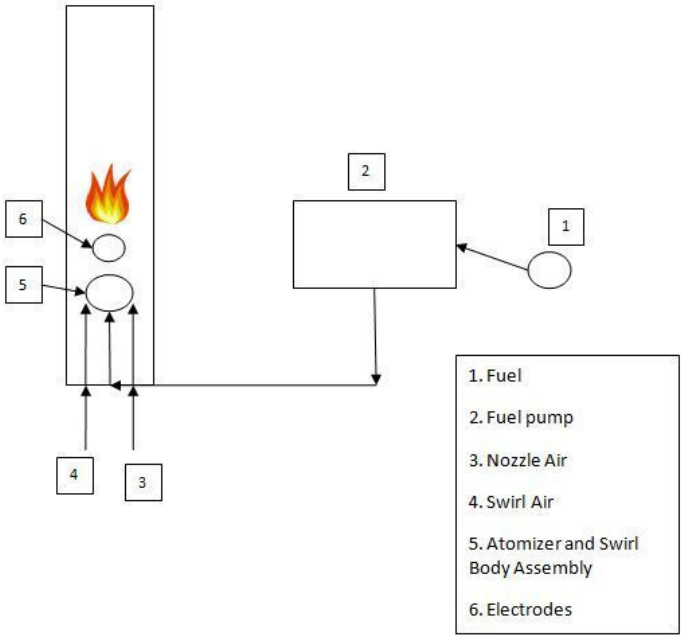

Figure 2. Swirl flow combustor test setup layout.

Data Acquisition

For this testing, a National Instruments PCI 6221 data acquisition card was used to capture the input signals from each air flow meter. Also, a National Instrument CB-68LP terminal block was used in conjunction for input of the signals to the data acquisition card. Using the air and fuel flow rates, an equivalence ratio was determined and displayed continuously using a LabView VI. This equivalence ratio was purely theoretical and used only as a reference because it was calculated assuming that all of the fuel was consumed in the combustion process.

Volumetric Flow Pump

In order to supply fuel to the nozzle, a Masterflex volumetric peristaltic pump was used. The pump is comprised of the three main parts: the console drive, the pump head and the tubing. As seen in Figure 3 a Masterflex HV-77521-40 variable-speed drive was selected as the console, and is capable of speeds from 6 to 600 rpm. Along with the Masterflex HV-77201-60 pump head and size 13 tubing, the peristaltic pump was capable of pumping between 0.36 and 36 mL per minute. During testing the volumetric flow of the fuel varied from approximately 3.6 to 22 mL per minute depending on the viscosity of the fuel tested.

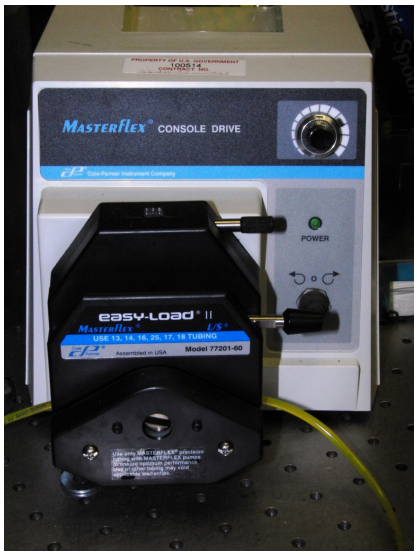

Figure 3. Masterflex peristaltic volumetric flow pump used to supply fuel to the atomizer.

Air Flow

The air for the testing was supplied from a local compressed air supply. The main air supply line was split between two control knobs, which supplied air to both the nozzle air supply as well as the swirl flow air supply. Nozzle air flow rates varied between 4 and 12 standard liters per minute, while the swirl air flow varied between 60 and 300 standard liters per minute depending on the fuel.

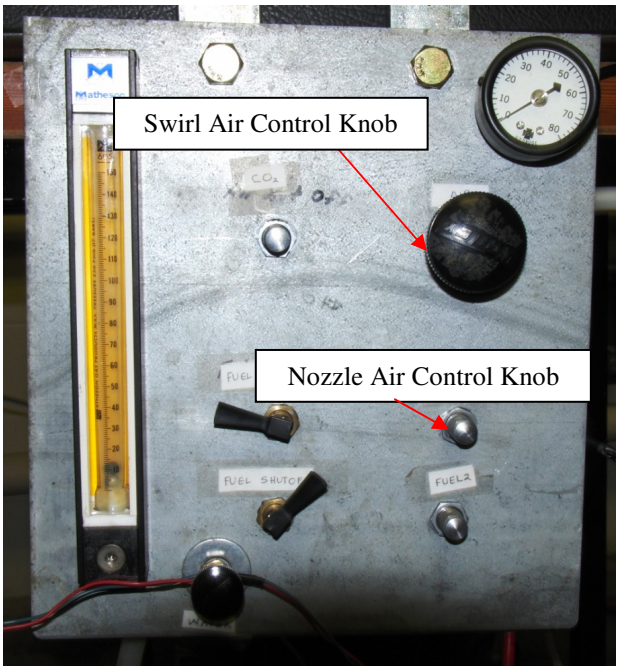

Figure 4. Control panel for swirl stabilized combustor.

Nozzle Design

For this testing, a Danfoss siphon SN609-2 air assist nozzle was used to atomize the fuel prior to ignition. This nozzle is designed to create a fine, well atomized spray at low pressures and is well suited for higher viscous fluids such as waste oil. A cut out of the nozzle, viewable at the Danfoss website, can be seen in Figure 6, the nozzle has four distinct parts; the tip, disc, stem and O-ring. As seen in Figure 5, fuel travels up the stem and the disc and into the mixing chamber between the disk and the outer orifice of the tip. Nozzle air enters through the outer channels into the tip and mixes with the fuel in the mixing chamber. The resulting spray angle is dependent on both the fuel and air flow rates into the mixing chamber. This particular nozzle is designed to output 0.2 GPH of fuel-air spray with an average pressure between 3 and 5 psi based on input flow rates.

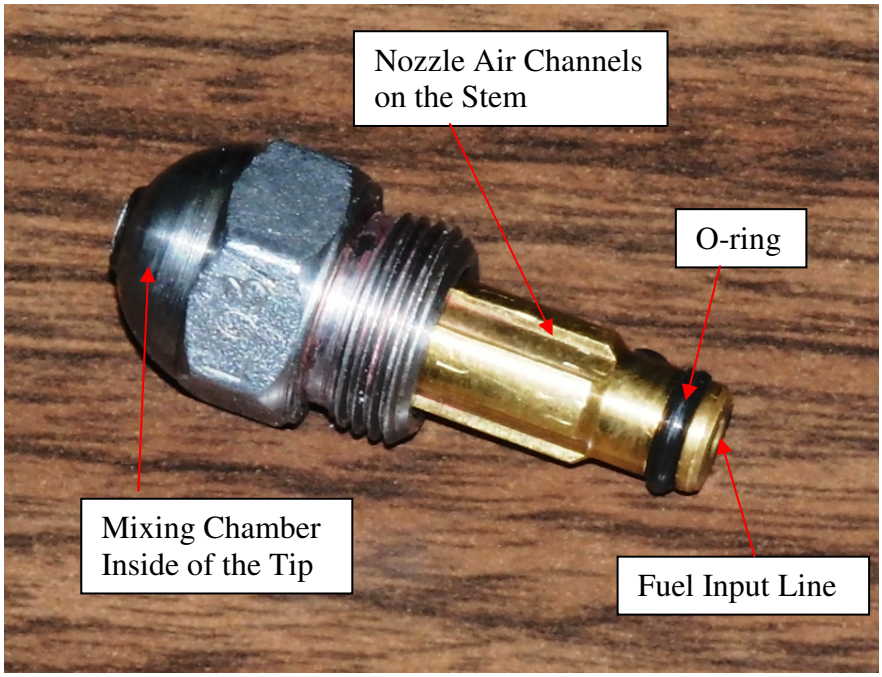

Figure 5. Nozzle used for atomization in swirl stabilized combustor.

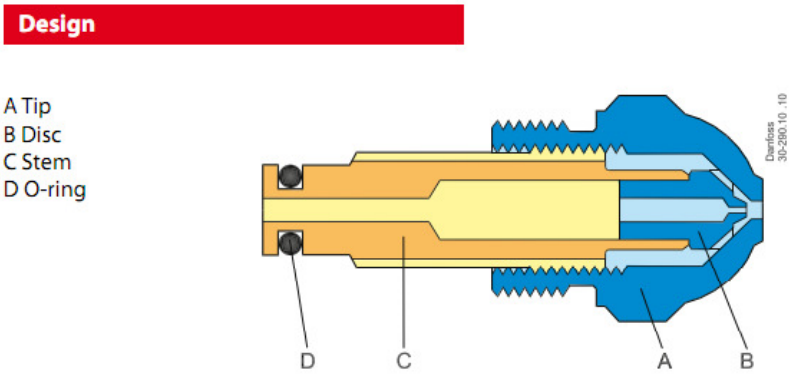

Figure 6. Cut away of nozzle used for atomization in swirl stabilized combustor. Source: http://hago.danfoss.com/PCMPDF/DKBDPD080E122.pdf, December 2010. (under fair use, 2010)

Test Stand

The test stand begins with the pvc housing body, which contains the flow lines for both air inputs as well as the fuel input. Figure 7 illustrates the components within the housing. The fuel flow line directly connects to the stem of the nozzle. The nozzle air line is tied into the nozzle connection housing and is allowed to flow separately up the channels of the nozzle stem. The surrounding air flow enters at the bottom of the housing and flows around the nozzle through a

specially designed set of brass guide vanes. As seen in Figure 8, brass guide vane piece has six vanes, each set at 45 degrees to the horizontal. The guide vane piece rests in the top of the housing surrounding the nozzle, and is surrounded by the electrode mounting plate. Two electrodes are used to ignite the fuel air mixture leaving the nozzle. A glass chimney is placed over the test stand to isolate the flame as well as provide a safety boundary.

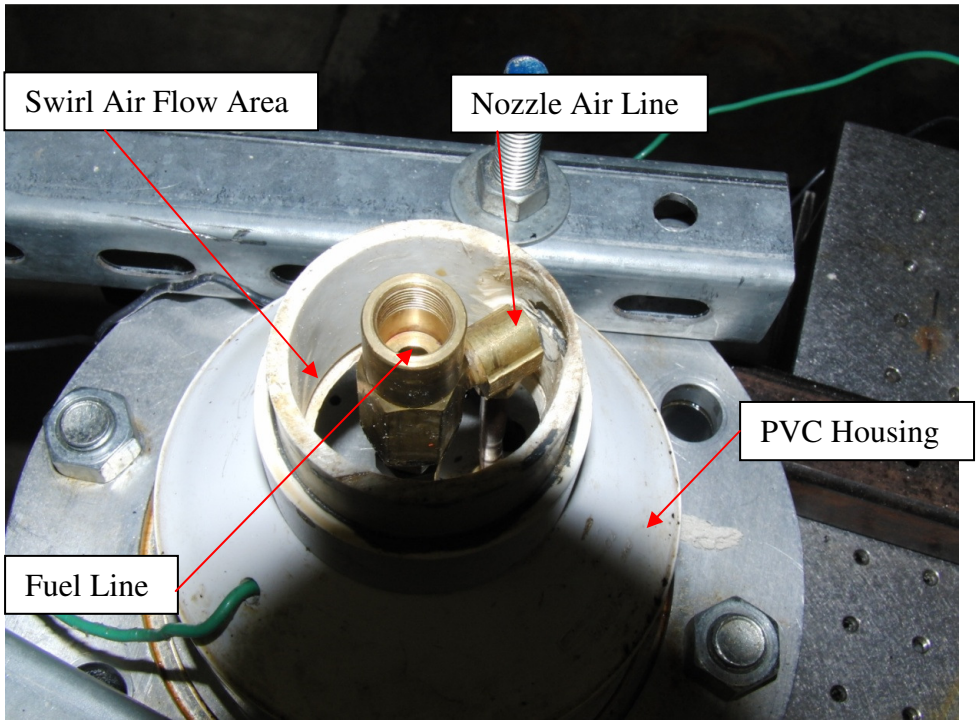

Figure 7. Inside of the swirl stabilized combustor.

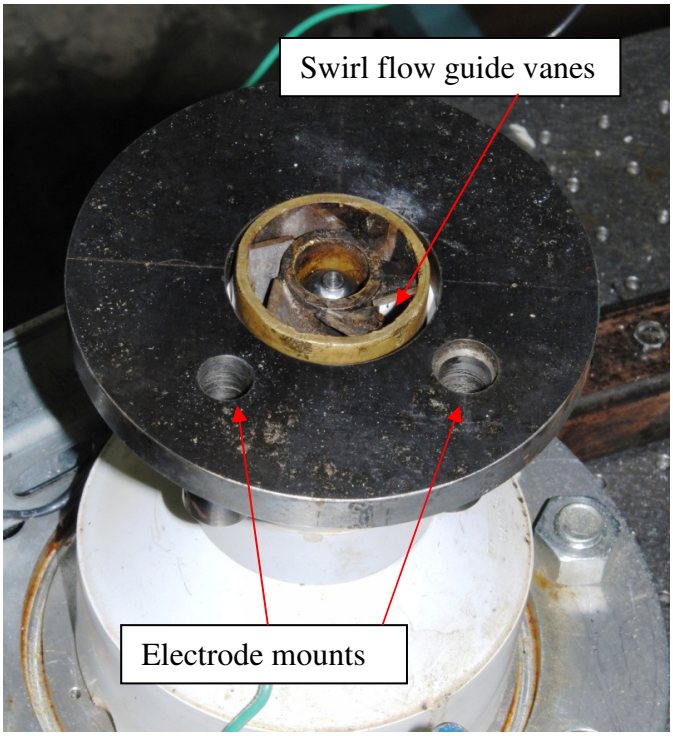

Figure 8. Assembled swirl stabilized combustor.

Procedure

Qualitative combustion tests were initiated by running the LabView VI for 60 seconds to generate baseline data for air flow rates. During this period the nozzle air and swirl flow air rates were set to approximately 4 and 60 standard liters per minute. These flow rates were recorded and commented on in order to help characterize the burning of each fuel. After 60 seconds, the fuel flow pump was turned on along with the electrodes. Upon ignition, or a noticeable exiting of fuel from the nozzle, the two air flows were adjusted in order to either achieve or increase the quality of combustion. Images and video were taken for each fuel both during and after the test.

Results and Conclusions

Setup Modifications

Initial tests with Diesel showed that there was some level of incomplete combustion. Atomized droplets of fuel were viewed hitting the glass chimney. The source of the error was the absence of a flame development zone. Essentially, the level of supporting swirl flow for a stabilized flame was coming in contact with the flame at a very early stage before all of the fuel exiting the

nozzle could combust. In order to solve the problem, a pyrex cylinder was inserted around the nozzle. This effectively lessened the impact of the swirl flow around the entrance region, which allowed the fuel to fully combust before being stabilized. It should be noted that the pyrex cylinders were replaced after two to three tests due to the fact that the flame temperature reached the melting temperature of the pyrex. If left under that state, the pyrex would begin to deform, as seen in Figure 10. The progression of the testing setup as well as results can be seen in Figure 9 through Figure 14.

Testing Observations

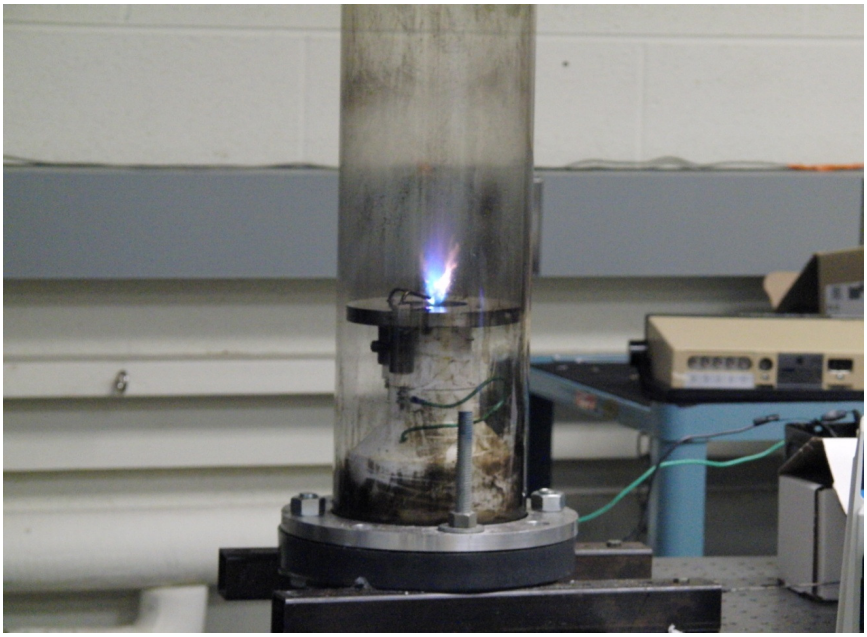

Figure 9. Diesel flame burned in combustor.

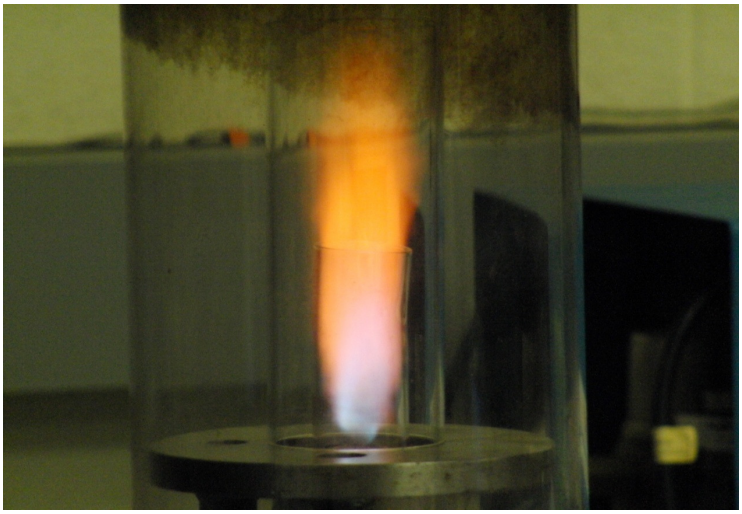

Figure 10. Diesel flame burned in combustor with pyrex chimney.

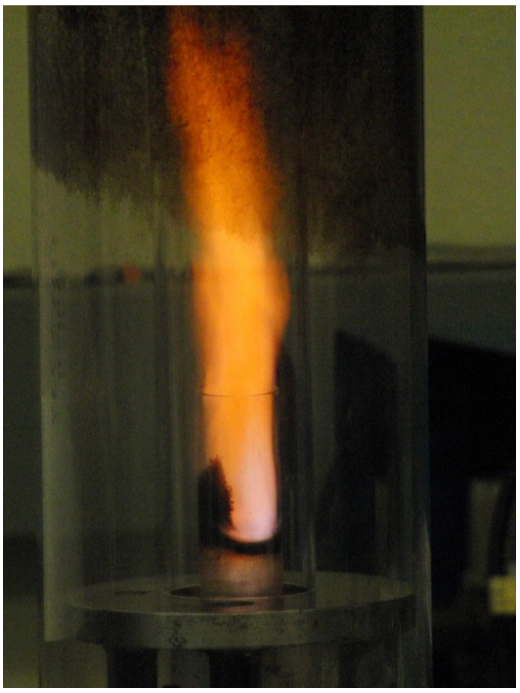

Figure 11. 767P070 flame burned in combustor with pyrex chimney.

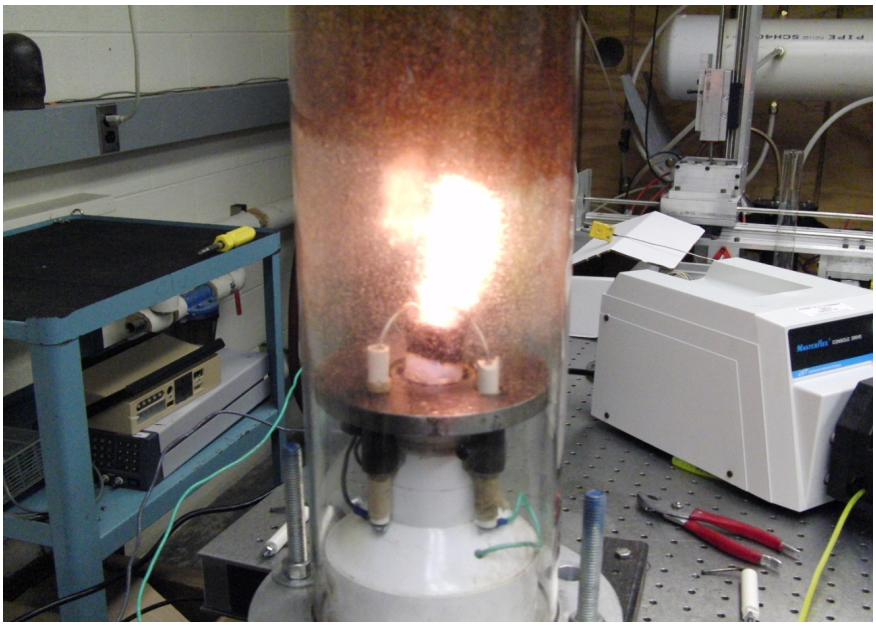

Figure 12. Sample Fuel 767P024 burned in combustor with pyrex chimney.

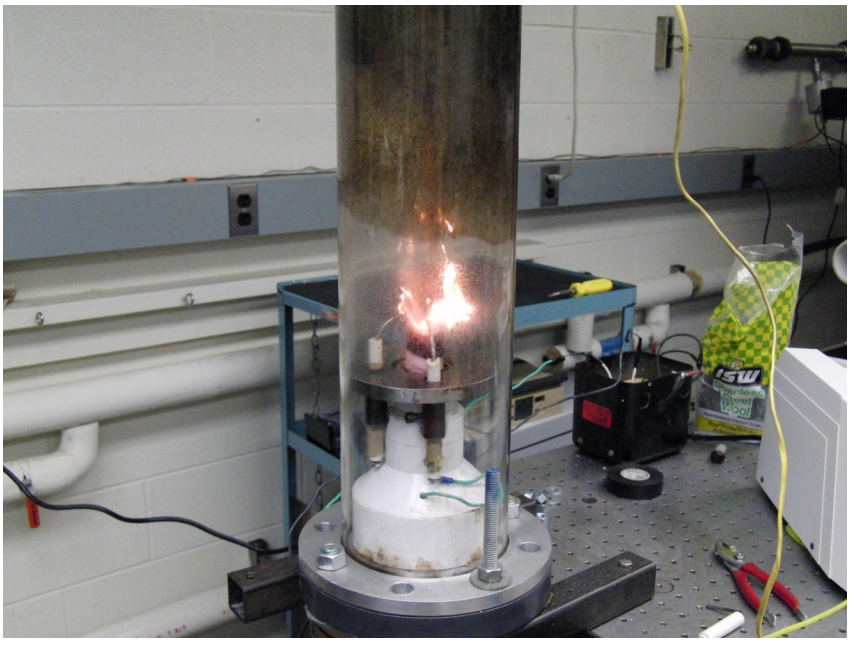

Figure 13. Sample fuel 767P024 burned in combustor with pyrex chimney.

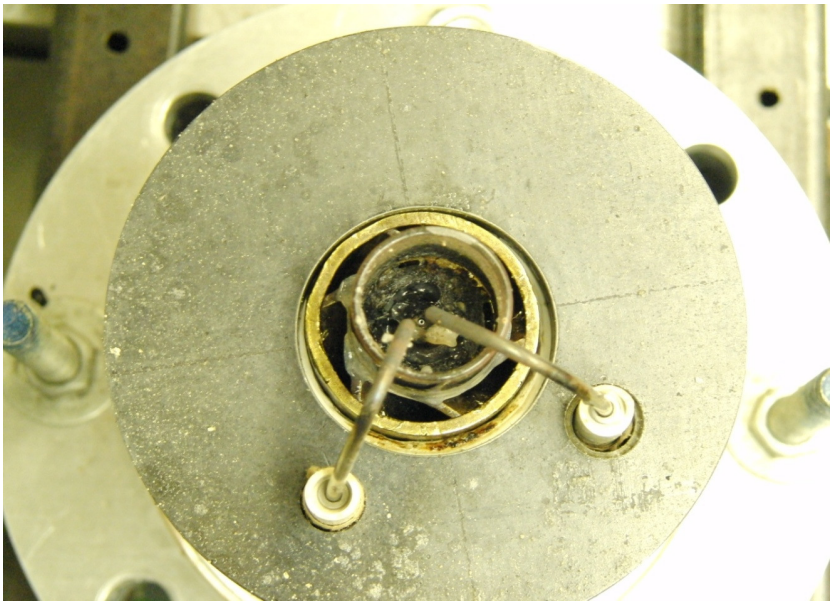

Figure 14. Resulting unburned fuel collection from combustion of sample fuel 767P024.

For this qualitative analysis, diesel was used as a baseline example of steady combustion. As seen in Figures 11 through 14, modifications were made to the system in order to even ignite the FRF tested. With the system modifications, only two fuels, P070 and P024, were able to achieve semi stable combustion. P024 was an emulsified fuel whereas P070 was not. The most successful of these fuels was P070, which has maintained the most stable and controllable flame. The results still show that the ignition of P070 was very poor due to the high level of soot buildup along the pyrex and glass chimneys. It is acknowledged though that pyrex is directly defining the flame stability region and this could be contributing to some of the soot buildup. Fuel 767P024 was able to ignite, but was never able to achieve even a semi-stable level of combustion. As seen in Figures 12 and 13, the resulting flame was unpredictable, volatile and unstable. This is due to poor atomization of the emulsified fuel. Instead of properly atomizing the fuel into small particulates, the fuel jetted out of the atomizer in ligaments, resulting in partial burning and eventual fuel buildup around the nozzle. The unburned fuel from the test stuck to the walls of the chimney or the nozzle and continued to heat up. The heated fuel changed from a high viscous liquid to an amorphous solid to the heat and began to clog the system. From these results, Luna Innovations interpreted the results and proceeded to develop another generation of fuels to be used for the final three tests, the cone calorimeter, the engine performance test and the fire resistance testing.

Recommendations

The primary reason for the poor performance of the FRF in this experiment is due to poor atomization. Though these are desirable results, it is recommended that other nozzles, capable of different exit orifice pressures and flow rates, be tested with the sample FRF to see if atomization improves. Two different nozzles, the SN609-4 and SN609-5, were purchased in an attempt to increase the level of atomization of several Luna sample fuels, but these tests were never conducted due to a time constraint. Each of these nozzles have been purchased from Danfoss and are rated to have higher output flow rates than the original. Testing with the two new nozzles should be compared with the first and used to understand more fully the fuel behavior in this system and potentially validate the original findings.

Though the pyrex chimneys showed promise as a viable solution to the lack of a flame development zone, a more permanent solution needs to be explored. Upon trying to run multiple tests with the pyrex chimney, the temperature of the pyrex quickly reached its melting temperature and began to deform altering flame shape. A more permanent solution should involve designing the system so that the nozzle is recessed even more below the swirl flow guide vanes. The guide vanes are made of brass and have a melting temperature that will not be reached during this testing. Also, it is recommended that the angle of the guide vanes be reduced from 45 degrees to approximately 30 degrees. This will help alleviate flame stability issues due because the base area of the flame will be allowed to wide and further develop before encountering surrounding swirl flow.

Chapter 4 - Cone Calorimeter

Introduction

Used as a supplemental evaluation of the fuels, cone calorimeter tests were performed with the fuels selected to be tested in the engine and the rotary atomizer. For the purposes of this project, the cone calorimeter was used to determine the effective heats of combustion of the fuels tested. The effective heat of combustion of a fuel is defined within the ASTM E1354 standard for heat and visible smoke release rates for materials and products using an oxygen consumption calorimeter[2] as the measured heat release divided by the mass loss for a specified time period. During this testing, the heat release, or energy content, of each fuel will be measured using the cone calorimeter. The effective heat of combustion will be determined as the heat release over the course of the entire fuel burn divided by the mass of the fuel burned.

The determined effective heats of combustion are projected to be less than theoretical heats of combustion, also known as heating values, due to the incomplete combustion. Heating values, which are widely published for several fuels, are determined using a bomb calorimeter, which was not available for this testing. During this testing, the effective heat of combustion will be compared to the net heat of combustion for both Diesel and Jet-A, whose values are widely published. The net heat of combustion is also known as the lower heating value of a fuel, which is a measure of energy release of the fuel upon combustion assuming that the water found in the products is in vapor form.

Nomenclature

Theoretical Calculations

Symbol	Units	Description
$\dot{m}_e$	kg/s	Exhaust duct mass flow
ρ	kg/m^3	Density of fluid
Q	m^3/s	Volumetric flow rate
V_1	m/s	Fluid velocity through orifice hole
V_2	m/s	Upstream fluid velocity
P_1	Pa	Fluid upstream pressure
P_2	Pa	Fluid downstream pressure
A_1	m^2	Cross-sectional area of exhaust duct
A_2	m^2	Cross-sectional area of orifice hole
d_1	m	Diameter of exhaust duct
d_2	m	Diameter of orifice hole
α	Dimensionless	Non-dimensional ratio
C_d	Dimensionless	Coefficient of discharge
β	Dimensionless	Ratio of d_1/ d_2
ρ_o	kg/m^3	Density of air
T_o	K	Ambient Temperature (291 Kelvin)
T_e	K	Exit Temperature
C	Dimensionless	Calibration Constant

Experimental Calculations

Symbol	Units	Description
$\dot{m}_e$	kg/s	Exhaust duct mass flow
$\dot{q}$	kW	Rate of heat release
Δh_c	kJ/kg	Net heat of combustion
r_o	Dimensionless	Stoichiometric oxygen/fuel mass ratio
ϕ	Dimensionless	Oxygen depletion factor
X_{CO}	Dimensionless	CO mole fraction reading after delay time correction
X_{O2}	Dimensionless	O_2 mole fraction reading after delay time correction
X_{CO2}	Dimensionless	CO_2 mole fraction reading after delay time correction
X_{O2}^{a}	Dimensionless	Ambient O_2 mole fraction
X_{O2}^{o}	Dimensionless	Initial O_2 mole fraction
X_{CO2}^{o}	Dimensionless	Initial CO_2 mole fraction
X_{H2O}^{o}	Dimensionless	Initial H_2O mole fraction
C	Dimensionless	Calibration constant
ΔP	Pa	Pressure difference across orifice plate
T_e	K	Absolute temperature of exhaust gas at orifice
$\Delta h_{c,eff}$	kJ/kg	Effective heat of combustion
Δt	s	Sampling time interval
m_i	kg	Initial specimen mass
m_f	kg	Final specimen mass
r	Dimensionless	Repeatability constant

Literature Review

This section provides a background on cone calorimetry as well as an overview of the existing research performed using the cone calorimeter. Developed in early 1980's, the cone calorimeter is a constant pressure process fire testing apparatus that operates on the oxygen consumption principle. This principle, also known as Thornton's [3] rule, asserts that for a large number of liquids and gases, a relatively constant amount of heat is released per unit mass of oxygen consumed during a complete combustion process. Clayton Huggett [4] also found this assertion to be true with organic solids as well. According to Thornton's rule, the measurement of the oxygen consumed in a combustion process is sufficient in order to determine the net heat released. The oxygen consumption principle states that approximately 13.1 MJ of heat is released for each kilogram of O_2 consumed for complete combustion of most materials. This assumption has been proved to maintain accuracy within ±5%. In order increase the accuracy of our measurements, the calorimeter is equipped with a gas analyzer capable of reading O_2, CO_2 and CO in the exhaust gases.

In depth descriptions of the development of the cone calorimeter as well as its current design, equations and guidelines are documented by Babrauskas [5] and Janssens [6]. Standardized technical details of the design of the apparatus as well as analysis procedures and equations have been standardized by the ASTM [2].

Extensive research has been conducted with polymers using the cone calorimeter. Babrauskas and Grayson [7] discuss calorimetry parametric study results for different polymer groups. These results focus on heat release rates at various heater heat flux settings. Rhodes and Quintiere [8] also conducted research on the burning rate and flame heat flux for black Polycast PMMA, a polyacrylic, widely used as a substitute for glass due to its high light transmittance.

Studies have also been conducted on the cone calorimeter which are designed to both compare its accuracy as well as explore its capabilities. Ostman and Svensson [9], have conducted research comparing the rate of heat release results for three different apparatuses, all of which operate under the oxygen consumption principle. The testing methods compared were the OSU-box modified for O_2 consumption, the STFI open arrangement as well as the cone calorimeter.

Also, ignitability measurements were taken by Babrauskas and Parker [9] using the cone calorimeter with a focus on using the irradiance source to make measurements of radiant ignition on materials.

Test Setup

The cone calorimeter consists of several different parts and devices, each of which performs a different and important task. This can be seen in Figure 15, which displays the cone calorimeter used for this experimentation. This system has been divided into seven different categories of focus: the combustion chamber, exhaust system, transport system, gas analyzer, orifice plate, scale and data acquisition.

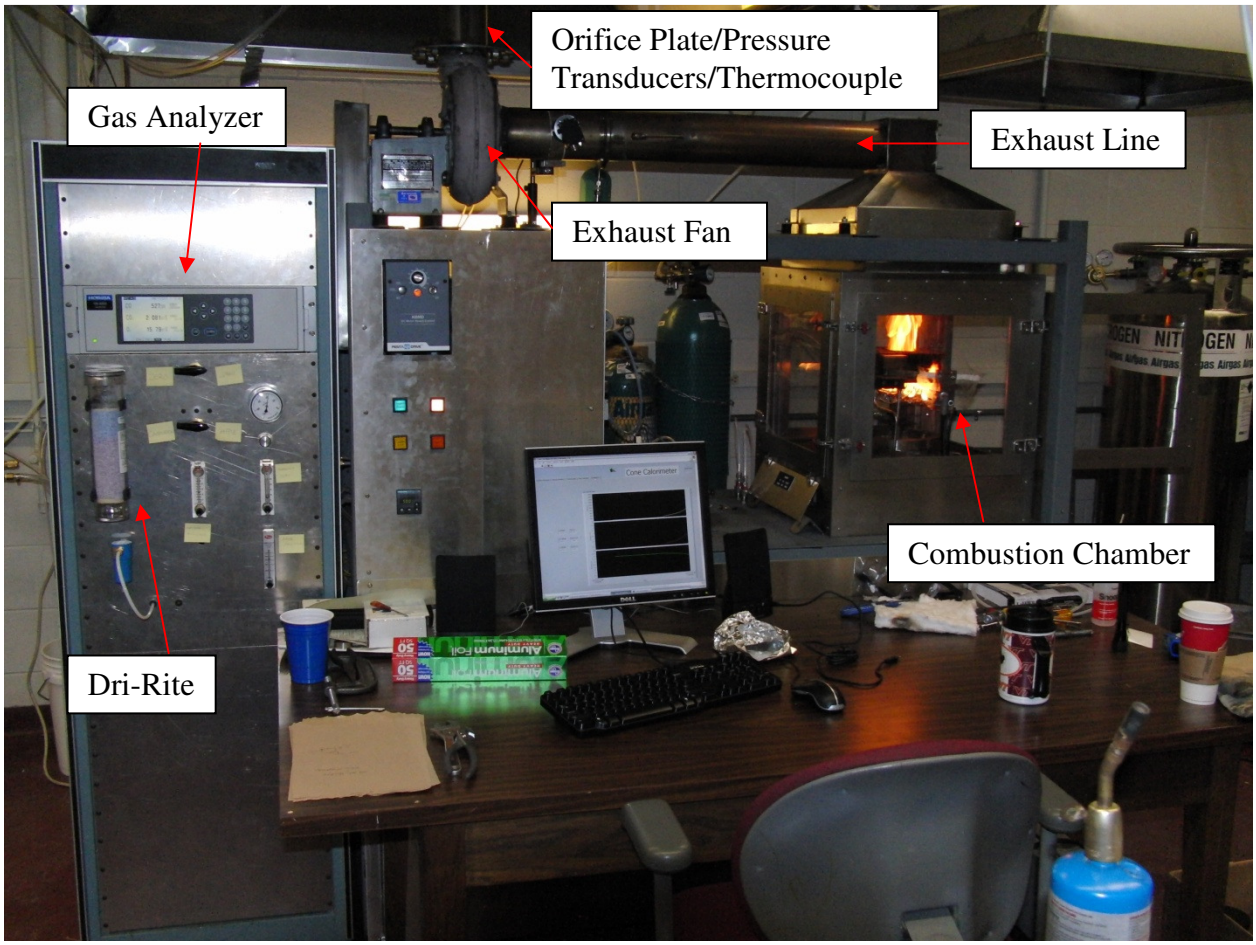

Figure 15. Layout of the cone calorimeter.

Combustion Chamber

The combustion chamber of the calorimeter houses the combustion reaction to be analyzed as well as all of the components required to initiate burning. This can be seen in Figure 16. A conical heater is mounted to rod within the chamber and can be adjusted vertically by means of a pulley system. Three type k thermocouples are integrated within the heater and are connected to a PID temperature controller to ensure constant temperature. The heater is used to uniformly preheat the fuel for a faster ignition. Below the heater is a sample pan holder, which provides a means to mount the fuel sample pan as well as connect it to a scale mounted below the chamber. The fuel sample pan is a 100 mm by 100 mm square steel plate that is used to house the fuel during combustion. There is a layer of low density ceramic wool as well as two layers of heavy duty aluminum foil between the fuel and the sample pan. This measure is used to limit the energy losses to the surroundings during the combustion process. For each test, there must be one inch of separation between the fuel and the conical heater. Ignition is achieved from an electrode which is pneumatically charged to swing over and then away from the sample pan. Lastly, within the combustion chamber is a mount for the methane burner, which is used in calibration of the cone calorimeter.

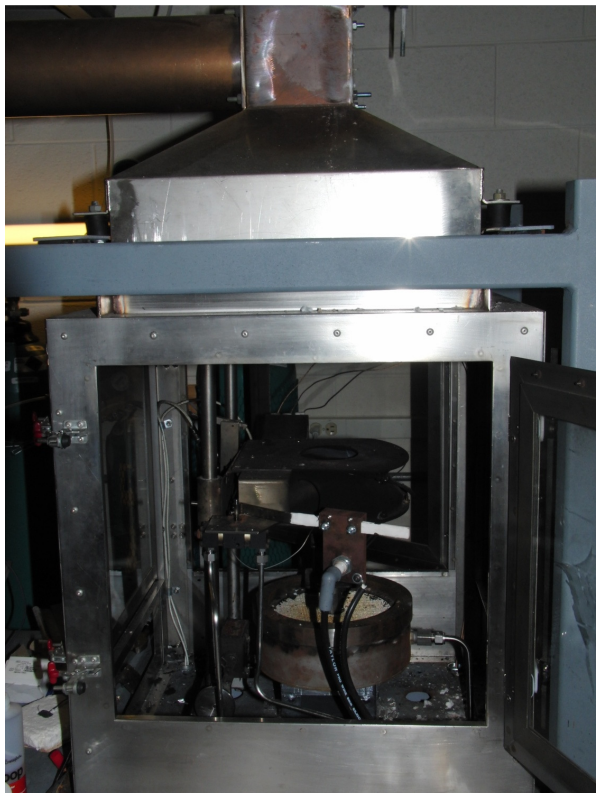

Figure 16. Combustion chamber of the cone calorimeter.

Exhaust System

Products of the combustion process leave the combustion chamber and are forced into the exhaust system. Exhaust gases are driven through exhaust ducts located above of the combustion chamber, by an American Davidson Sturdivant exhaust fan. A sample ring, located approximately half way down the exhaust duct, redirects some exhaust down through a transport system to the gas analyzer, while allowing the rest to travel out the exhaust duct into a ventilation hood.

Transport System

The transport system is responsible for collecting samples of exhaust gas from the sample ring and delivering them to the gas analyzer. During this process, the exhaust gas is prepared for entering the gas analyzer. Exhaust gases are pumped from the sample ring through the transport system by a Thomas 927CA18 diaphragm compressor vacuum pump. Three filters, one course grain, and two fine grain are used to filter out all of the soot from the transported samples. The course filter is a Balston A914A-DX compressed air filter that has been hallowed out and filled with fine grade glass wool. The first fine course filter is (type of filter housing and filter). The last course filter is a Balston A914A-DX compressed air filter. After the soot has been removed from the gas, the exhaust travels through a cylinder of Dri-Rite to remove all water particles. The exhaust gas is then transported through the gas analyzer, a Cole Parmer L-79200-30 vacuum pressure diaphragm pump and out of the system to an exhaust hood.

Gas Analyzer

The gas analyzer used for this testing is a Horiba VA-3000. Seen in Figure 17, this particular model is equipped to measure incoming levels of CO, CO_2 and O_2 to with a repeatability of ± 0.5% for full scale range. For this testing, the incoming gas maintained an approximate 0.5L/min flow rate. The CO level was measured between 0-2000ppm, while the CO_2 level was measured between a 0-5% range, and the O_2 level was measured between a 0-25% range. The measured gas levels were recorded using National Instruments data acquisition hardware and viewed in LabView.

Figure 17. Control panel of the cone calorimeter.

Orifice Plate

An orifice plate is located vertically between the exhaust fan and the exhaust duct. The orifice plate is used to determine the mass flow rate of the exhaust gases. The orifice plate used can be seen in Figure 18 along with the pressure transducers and thermocouple. This thin circular plate with a hole in the center constricts the flow the exhaust gases by reducing the piping diameter. The maximum point of convergence is located slightly downstream of the plate and is called the vena contracta point. By measuring the difference in the gas pressure on before and at this point, the mass flow rate can be determined using Bernoulli's principle. The exhaust temperature is also measured before the gas enters the orifice plate.

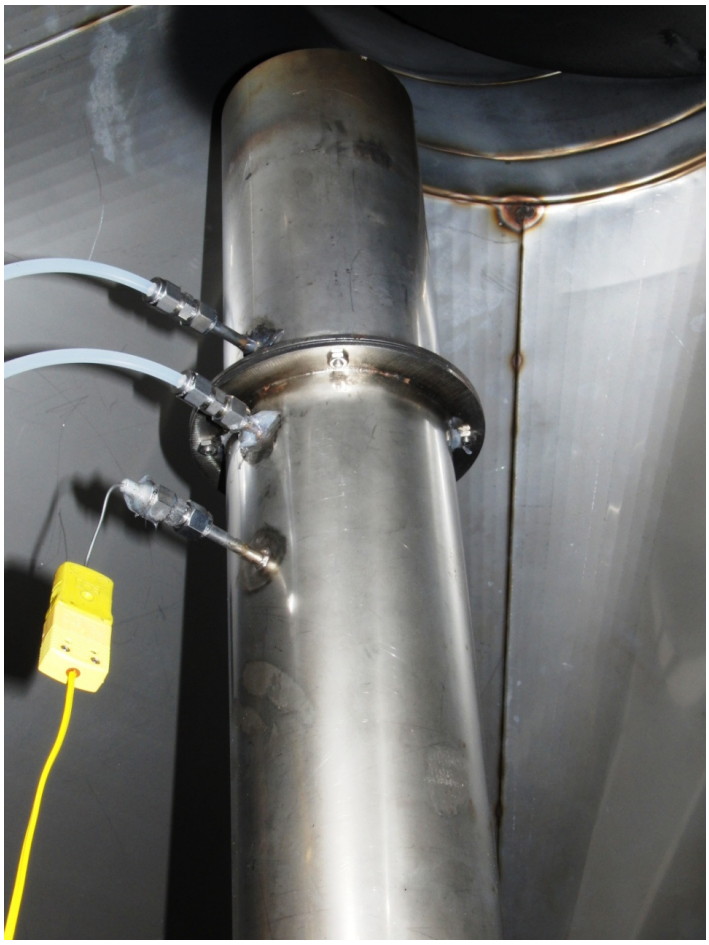

Figure 18. Orifice plate in the exhaust pipe of the cone calorimeter.

Scale

The scale used for this testing was a Sartorius FB6CCE-S, as seen in Figure 19. The scale was used to keep real time fuel mass loss over the course of the burning process. The scale was capable of outputting a signal to the data acquisition system and was monitored via LabView. This data was compared with bulk scale measurements taken before and after the test to determine the total fuel mass burned.

Figure 19. Sartorious load cell used to monitor the fuel mass during each test.

Data Acquisition

For this testing, data was collected using National Instruments data acquisition hardware and LabView. A SCXI-1000 chassis was used to house each of the data acquisition modules. A SCXI 1600 controller module was used to connect the system to the computer via USB. A SCXI 1102 thermocouple and low voltage input module along with a SCXI 1303 high precision terminal connection block. Also, a SCXI 1124 digital-to-analog voltage output module along with a SCXI 1325 terminal connection block.

Procedure

During each day of testing, the calorimeter must undergo a heat release rate calibration to ensure the equipment is functioning properly as well as adjust for minor changes in factors which effect the mass flow determination. This is accomplished by running a 5kW burn of methane for ten minutes. This methane burn is used to determine a calibration constant for the testing equipment at its current state. This calibration constant takes into account the surroundings in the testing environment for that day, such as the air density, humidity and heat lost to surroundings. The calibration constant also takes into account any inaccuracies in the pressure transducers,

thermocouple used in the orifice plate and gas sampling system. A calibration difference of more than 5% between sequential testing days suggests an equipment malfunction.

Prior to the calibration test, it is necessary to calibrate the gas analyzer. The gas analyzer is calibrated to a level of 20.95% volume of oxygen, 0.043% volume of CO_2 and 2 parts per million of CO. The first step to calibrating the gas analyzer is zeroing the O_2, CO and CO_2 readings by supplying the module with pure Nitrogen. Upon zeroing the readings, the CO and CO_2 readings are calibrated by supplying the module with a span gas with known levels of CO and CO_2. Lastly, the O_2 reading is calibrated by supplying the analyzer with surrounding air.

Upon calibrating the gas analyzer, the methane burner is loaded into the combustion chamber. The data acquisition is initiated and allowed to collect data for two minutes. During this time, methane of 99.5% purity is supplied to a mass flow controller in route to the burner. The electrode is swung over top of the burner and kept continuously sparking until ignition. At the end of the two minutes, the mass flow meter is initiated through the data acquisition vi to supply the methane to the burner. The methane is then lit upon exiting the burner, and the electrode is shut off and swung out of the way. The methane burn calibration test is then run for ten minutes while the data acquisition system collects data. At the end of the ten minutes the methane supply is cut off and the data acquisition continues to run until the gas analyzer returns to the normal levels. Using the data recorded, a calibration constant is determined and incorporated into the calculation of the fuel's effective heat of combustion.

Testing of fuels begins by setting the conical heater within the combustion chamber at 590 degrees Celsius, corresponds to a heat flux of 20 kW/m^2. Tests are initiated by starting the data acquisition VI and allowing data to be collected for two minutes. During this time, 25mL of fuel is placed in the sample plate and weighed prior to testing seen in Figure 20. At the end of the two minute baseline data window, the sample pan is placed in the combustion chamber underneath the conical heater. Just as in the calibration burn, a spark igniter is swung over the fuel and remains sparking until the fuel is lit. The sparker is then swung back for the remainder of the test. By placing the fuel in just before ignition, the escape of fuel vapors due to the heat is minimized.

The volumetric flow rate of the exhaust gases into the gas analyzer is monitored to ensure that there is constant flow for the duration of the test. The accuracy of the gas product level data depends on the flow rate into the gas analyzer remaining constant. The test is concluded when the fuel burns completely out. The data acquisition is allowed to record until the gas analyzer has reached normal ambient gas readings with O_2 reading 20.95 volumetric percent. The sample plate is then weighed again on the scale after the test to determine the bulk mass and percentage of fuel burned. The fuel data is then analyzed over the course of the time that the fuel was lit. The resulting heat released during the burn is divided by the mass of the fuel burned to calculate the effective heat of combustion. The calculation of the heat release rate will be discussed in the next section.

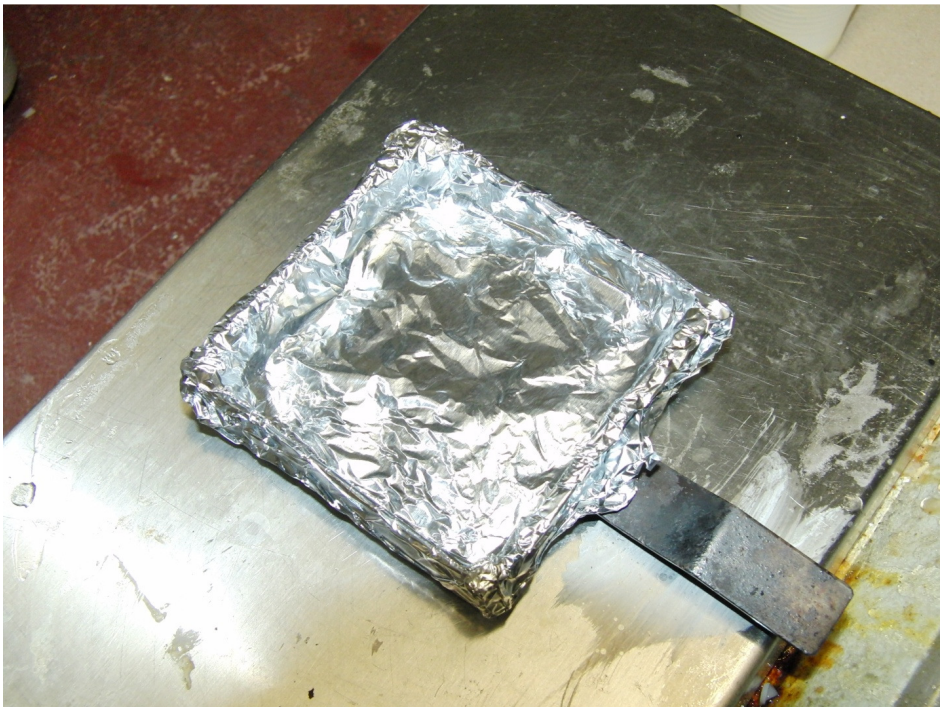

Figure 20. Test sample pan for the cone calorimeter before a test.

Calculations

Theoretical Calculations - Calibration Constant

Theoretical calculations were performed prior to determining an experiment calibration constant. Equations were taken from both Fluid meters[11] as well as Fundamentals of Fluid Mechanics[12]. The results from the theoretical calculations were compared to the experimental values for validation.

The calibration constant is calculated using Bernoulli's equation across an orifice plate. The calibration constant is defined as

$$C = \frac{\dot{m}_e}{\sqrt{\frac{\Delta P}{T_e}}} \tag{2}$$

where $\dot{m}_e$ is the exhaust gas mass flow rate, ΔP is the pressure difference across the orifice plate and T_e is the exhaust gas temperature at the orifice plate.

$$\dot{m}_e = \rho V A \tag{3}$$

$$Q = VA \tag{4}$$

By applying Bernoulli's equation to the incompressible flow across an orifice plate, the solution reduces to

$$P_1 + \frac{1}{2}\rho {V_1}^2 = P_2 + \frac{1}{2}\rho {V_2}^2 \tag{5}$$

where the values for pressure and velocity upstream of the orifice plate are represented as state 1 and the same variables downstream of the orifice plate are represented as state 2.

$$\Delta P = \frac{1}{2}\rho \left(\frac{Q}{A_2}\right)^2 - \frac{1}{2}\rho \left(\frac{Q}{A_1}\right)^2 \tag{6}$$

$$Q = A_2\sqrt{\frac{2(\Delta P)/\rho}{1-(A_2/A_1)^2}} \tag{7}$$

$$Q = A_2\sqrt{\frac{1}{1-(d_2/d_1)^4}}\sqrt{2(\Delta P)/\rho} \tag{8}$$

The volumetric flow rate of the exhaust gases across the orifice plate is defined as

$$Q = C_d A_2\sqrt{\frac{1}{1-(\beta)^4}}\sqrt{2(\Delta P)/\rho} \tag{9}$$

where C_d is the discharge coefficient and β is the ratio of the exhaust pipe diameter to the orifice plate hole diameter.

$$\alpha = \frac{C_d}{\sqrt{1-\beta^4}} \tag{10}$$

As seen in Equation 11, the ideal gas law for constant pressure is used to reorganize Equation 9 in terms ambient air density, ambient air temperature and the exhaust gas temperature.

$$\rho_0 T_0 = \rho T_e \tag{11}$$

Upon substituting the volumetric flow rate of the exhaust gas into Equation 3, the exhaust gas mass flow rate is defined as,

$$\dot{m}_e = \rho Q = A_2\alpha\sqrt{2}\sqrt{\rho_0 T_0}\sqrt{\frac{\Delta P}{T_e}} \tag{12}$$

and the resulting calibration constant is calculated using Equation 13.

$$Calibration\ Constant = C = A_2\alpha\sqrt{2}\sqrt{\rho_0 T_0} \tag{13}$$

The calibration constant was theoretically calculated to be 0.0427.

Experimental Calculations - Calibration Constant

The mass flow rate of the exhaust flow through the duct is calculated using Equation 14. The calibration constant, C, is determined from each calibration run by substituting Equation 14 into the $\dot{m}_e$ in Equation 15.

$$\dot{m}_e = C\sqrt{\frac{\Delta P}{T_e}} \tag{14}$$

Upon calculating the calibration constant for the day, the heat release rate $\dot{q}$ is calculated using,

$$\dot{q} = 1.10\left(\frac{\Delta h_c}{r_o}\right) X_{O_2^a}\left[\frac{\phi - 0.172(1-\phi)X_{CO}/X_{O_2}}{(1-\phi)+1.105\phi}\right]\dot{m}_e \tag{15}$$

where ϕ is the oxygen depletion factor, which is a non-dimensional relationship between measured and initial moles of oxygen, carbon monoxide and carbon dioxide from the exhaust gas.

$$\phi = \frac{X_{O_2^o}(1-X_{CO_2}-X_{CO}) - X_{O_2}(1-X_{CO_2^o})}{X_{O_2^o}(1-X_{CO_2}-X_{CO}-X_{O_2})} \tag{16}$$

$$X_{O_2^a} = \left(1 - X_{H_2O}{}^0\right)X_{O_2^o} \tag{17}$$

The calibration constant used for the final day of testing was 0.0469. The theoretical calculation of the calibration constant varies from the measured value by approximately 9%. As stated by Babrauskas [5], it is difficult to calculate C to better than ± 5% of the measured value.

Effective Heat of Combustion

The effective heat of combustion is calculated using,

$$\Delta h_{c,eff} = \frac{\sum_i \dot{q}_i(t)\Delta t}{m_i - m_f} \quad (18)$$

where $\dot{q}_i$ is the heat release rate determined at each measurement increment, m_i is the initial mass of the fuel and m_f is the final mass of the fuel.

Estimation of Repeatability Constant

The repeatability of each test, otherwise known as the acceptable level of variation between test results, was calculated using an equation found in the Report to ASTM on Cone Calorimeter Inter-laboratory Trials [13]. The repeatability bounds for each fuel test are calculated using

$$\mathrm{r} = 1.23 + 0.050\Delta \mathrm{h}_{\mathrm{c,eff}} \quad (19)$$

where $\Delta \mathrm{h}_{\mathrm{c,eff}}$ is the effective heat of combustion.

Sources of Error

For analysis of these experiments, an assumption was made regarding the energy released per mass of oxygen consumed for each of the FRF. During testing the standard value of 13.1 MJ/kg O_2 consumed, or Thorton's rule, is used. In 1980, Clayton Huggett, a fire research scientist at the National Bureau of Standards, suggested that 13.1 MJ/kg O2 consumed should generate heat release rates to within ±5% for conventional organic fuels. This suggestion has since become accepted as the standard value for oxygen-consumption calorimetry of conventional fuels. For this testing, the chemical composition of the sample fuels was unknown. If the chemical composition is known then a more exact value can be calculated and used, thus increasing the accuracy of the test.

Testing Validation

Validation of the testing setup was required to ensure the accuracy of any of the fuel tests. PMMA, also known as polycast acrylic, has a known heat of combustion and also maintains a relatively constant heat release rate over the course of a 20 kW/m^2 incident flux test. This can be seen in both Figures 22 and 23 which are the measured and published heat release rates for 25 mm thick black PMMA with 20 kW/m^2 incident flux. A test was performed on 25 mm thick black PMMA with 20 kW/m^2 incident flux. As seen in Figure 21, the known heat of combustion for PMMA at these settings is 23.5 MJ/kg. Calorimeter testing experimentally yielded a heat of combustion for PMMA of 24.095 MJ/kg, which is a 2.53% difference from the known value. Figure 21 also shows the repeatability bounds calculated using Equation 19 for the published effective heat of combustion for 25 mm thick black PMMA with 20 kW/m^2 incident flux. Because the measured effective heat of combustion falls within this range of acceptable effective heat of combustion results, it has been concluded that the calorimeter testing setup and procedure are valid and accurate.

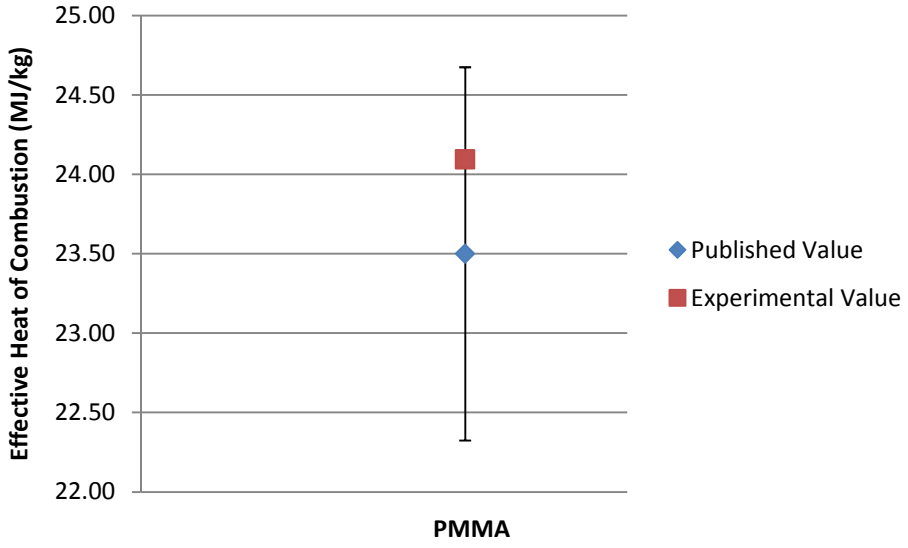

Figure 21. Repeatability bounds of published PMMA effective heat of combustion.

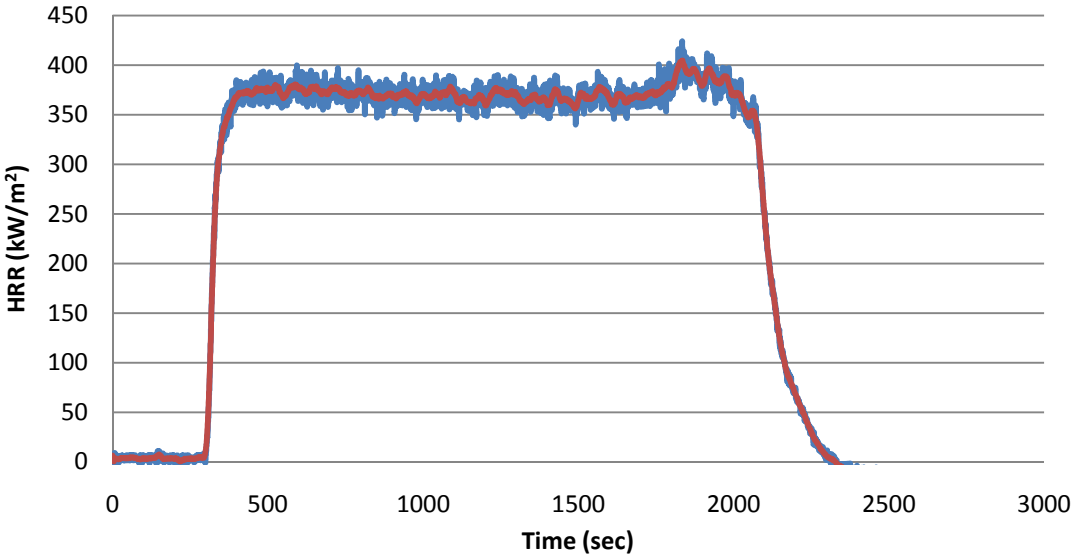

Figure 22. PMMA experimental heat release rate for an incident heat flux of 20kW/m2.

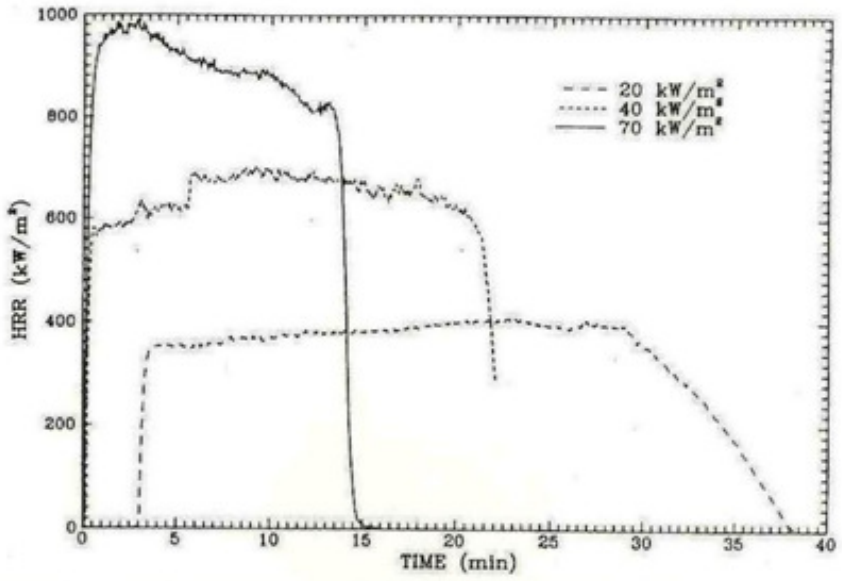

Figure 23. PMMA documented heat release rate [7] (under fair use, 2010).

Results and Conclusion

Effective Heat of Combustion

Testing was conducted for fire resistant fuels P184, P186 and P117, Diesel and Jet-A. Complete results from each test can be found in Appendix B. A comparison of the average results can be

seen in Figure 24. Results from Diesel testing yielded an average effective heat of combustion value of 40.75 MJ/kg. Results from Jet-A testing yielded an average effective heat of combustion value of 43.3MJ/kg. Diesel and Jet-A both have known lower heating values of 42.5 MJ/kg. Both Jet-A and Diesel tests resulted in effective heats of combustion within 5% of their known lower heating values. Though Diesel and Jet-A vary noticeably from one another, it is believed that this could be due to additives placed in the fuels by the fuel companies that would ultimately affect their heating values. The heating value of Diesel can vary depending not only on the source of its petroleum, but also on the refinery at which it was processed.

Results from the testing of the fire resistant fuels show that both P186 and P117 released as much if not more energy than Diesel and Jet A during the testing, having average effective heats of combustion of 43.01 MJ/kg and 41.49 MJ/kg respectively. Results from the sample fuel P184 showed that the average effective heat of combustion was 38.04 MJ/kg, which is a difference of 6.65% from the effective heat of combustion of Diesel. These results have been correlated to the engine results as well as rotary atomization results discussed in the following sections. These correlations will be discussed in the general conclusions section.

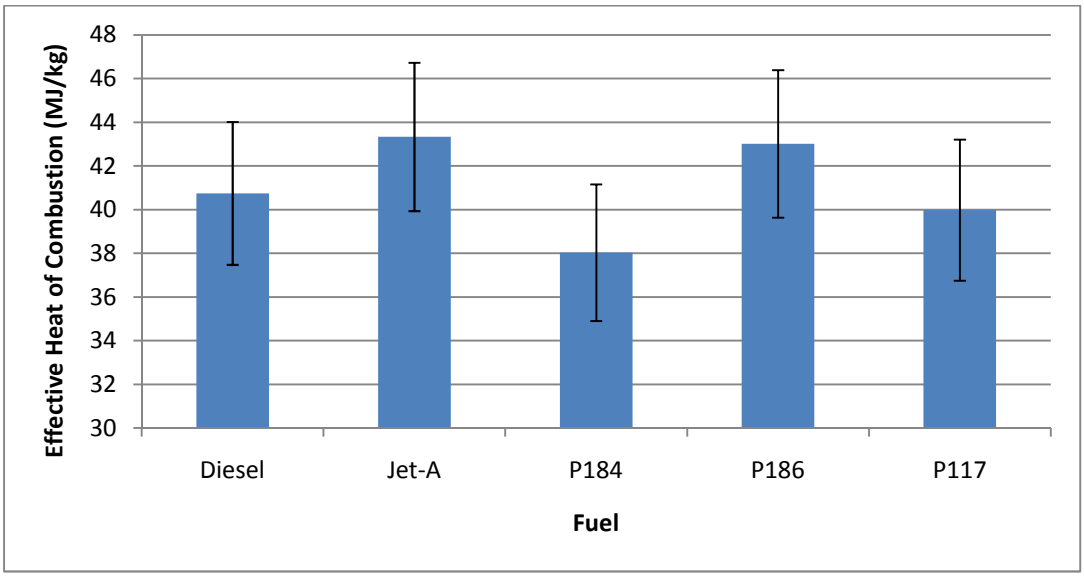

Figure 24. Effective heats of combustion comparison between fuels.

Fuel Pool Fire Observations

Also observed for each fuel were the pool fire characteristics during the calorimeter testing. There was a noticeable difference between the pool fire burn of emulsion FRF and non emulsion fuels. The non emulsion fuels such as Jet-A and P184, which can be seen in Figure 25, burn relatively calmly and occasionally form bubbles on the surface of the remaining liquid fuel. The emulsion FRF, which are represented by P117 in Figure 26, formed a thin film on the surface of the remaining liquid fuel which showed signs of char. This black film ultimately coated the bottom of the foil on the sample pan at the end of each test. This behavior corresponds to the behavior of the emulsion FRF in the swirl flow combustor, where unburned fuel turned into a solid. This behavior is noted, especially in regards to the engine performance and life of operation. Build up of unburned fuel within the fuel injection system could disable the fuel injection pumps, thus disabling the engine.

Figure 25. P184 pool fire during cone calorimeter testing.

Figure 26. P117 pool fire during cone calorimeter testing.

Repeatability

Since the testing setup and procedure has been validated for accuracy through a PMMA test, the fuel results have been analyzed in terms of their repeatability to ensure consistent results. Repeatability, as applied to this experimentation, addresses the variation in the results while each test is performed under the same conditions. The tests are determined to be repeatable if the variation in the data is smaller than the repeatability standard set by the ASTM. As noted in Appendix B, each fuel met the standards of repeatability set by the ASTM for cone calorimetry, with exception of one of the P117 runs. That particular test has been classified as an outlier and is not included in the P117 average effective heat of combustion.

Recommendations

The one key recommendation to be made for this testing is to run several more tests with each fuel in order to strengthen the statistical data. Currently, each of the Luna fuels have been tested a total of three times due to time constraints.

Chapter 5 - Engine Performance Testing

Introduction

The first of the two necessary qualifications for each fire resistant fuel is the ability to fuel military vehicles during normal operating conditions in the field. Currently, a majority of Army combat vehicles are equipped with compression ignition engines, otherwise known as diesel engines. This section will focus on testing the performance of the fire resistant fuels in comparison to Diesel and Jet-A in a Yanmar 2V750 compression ignition engine.

Nomenclature

Symbol	Units	Description
HP	hp	Engine horsepower
torque	ft-lb	Engine drive torque
rpm	rpm	Engine drive shaft rotational velocity

Compression Ignition Engines

A compression ignition engine, otherwise known as a diesel engine, is an internal combustion engine that uses compression within the combustion chamber to initiate the ignition process. During the beginning of the engine cycle, air is introduced to the combustion chamber and is then compressed by the piston with a compression ratio between 15:1 and 22:1 resulting in a pressure of approximately 580 psi. The compression stroke is used to heat up the air from ambient conditions to around 550 degrees Celsius, to be used as an ignition source for the fuel. At the top of the stroke, a small amount of fuel is forced through high pressure fuel injectors into the combustion chamber with the compressed air. Diesel engines are direct injection engines and their fuel injectors allow for a well atomized spray to enter the combustion chamber. The injected fuel spray is vaporized by the heat of the compressed air in the combustion chamber and

subsequently, the vapor is ignited by the same heat. The ignition of the vapor sets off the ignition of the rest of the fuel, thus propelling the piston down to begin the cycle again.

Yanmar 2V750

For the purposes of testing their fuels, Luna Innovations provided a Yanmar 2V750 diesel tractor engine. The Yanmar 2V750 is a two cylinder diesel engine capable of 17 horsepower at 3200 rpm. This engine was to be used for testing the various Luna fuels on a small scale, for viability as fuels in a military combat vehicle. In order to quantify the performance of each fuel in the engine in comparison to diesel, a means to load the engine and achieve its maximum power output with each fuel was needed. For this testing, a Land and Sea Dynomite water brake dynamometer was acquired from another research group at Virginia Tech.

Test Setup

Engine Electrical System and Test Kart

The first step towards making the engine operational was to electrically wire the engine components so that the engine could be run on Diesel fuel. As seen in Figure 29, an electrical diagram was constructed upon modifying a Husqvarna wiring harness to suit the engine. As seen in Figure 27, the engine was provided on a portable testing kart. The electrical operation panel mounted to the engine test kart can be seen in Figure 28. A test stand, composed of 1/8" thick steel angle iron, rests under the engine to provide a dampening effect as well as a separation area between the kart and the engine drive shaft. Upon modification of the engine's electrical system, a control panel was designed and mounted to the side of the engine kart.

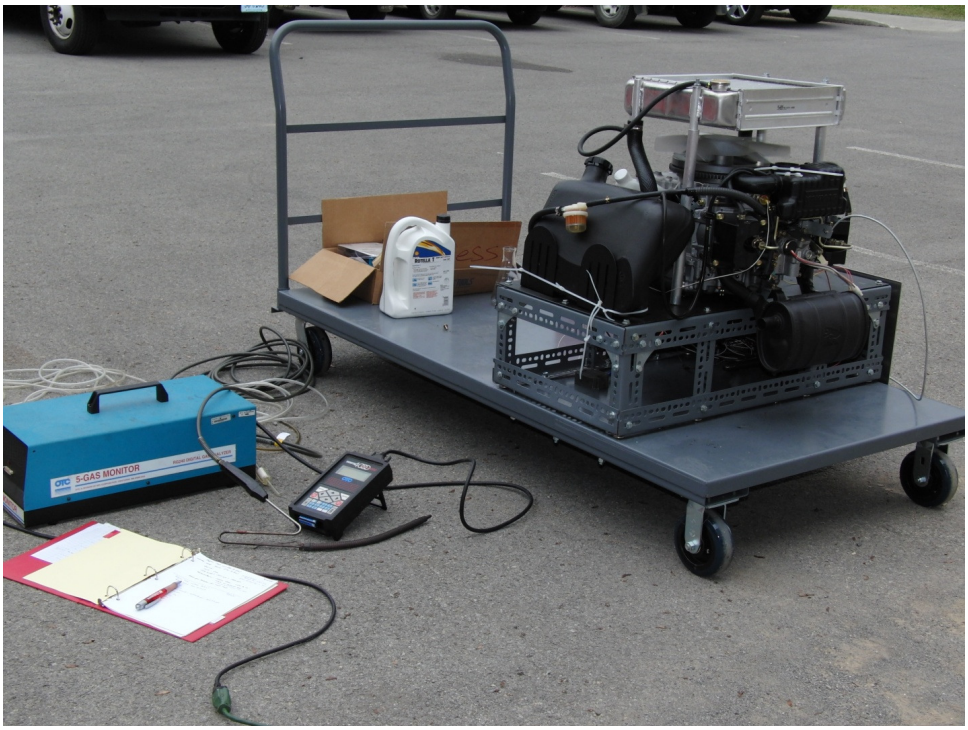

Figure 27. Initial engine testing kart.

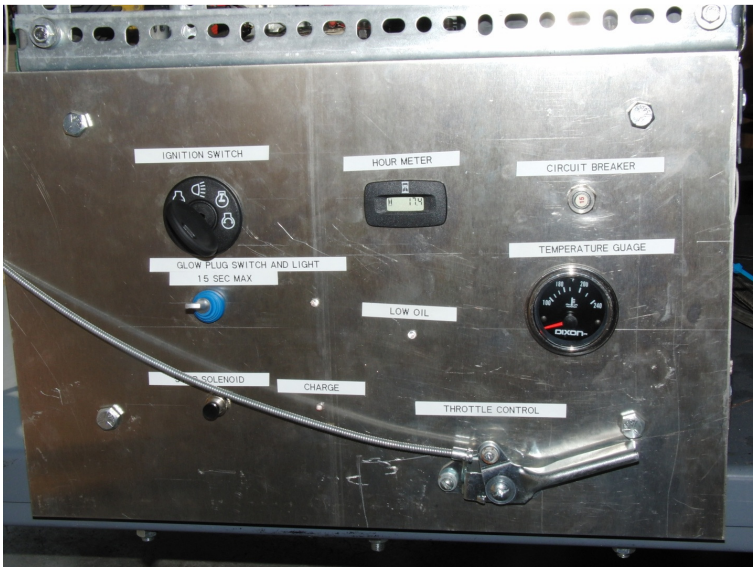

Figure 28. Engine operation control panel.

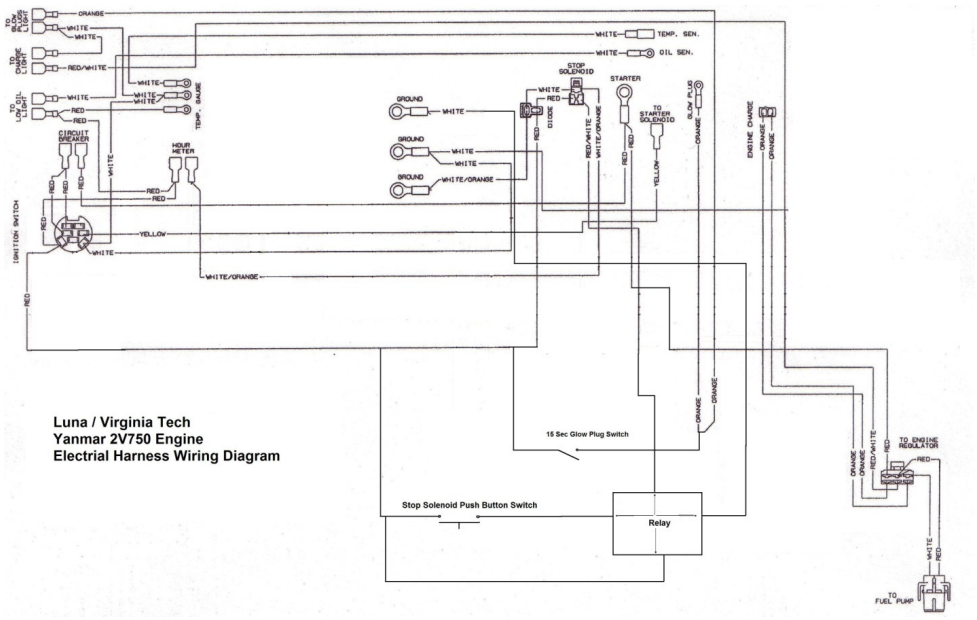

Figure 29. Revised wiring diagram for Yanmar engine.

Low Pressure Fuel Pump

Initially, several fuels were tested in the engine in order to determine whether or not adjustments needed to be made for operating the engine under optimal conditions. After establishing that the engine ran on Jet-A without any adjustments needed, certain Luna fire resistant fuels were run through the engine. Fuels tested include P022, P070A and B, P056. These fuels were not the fuels being tested, but rather they were used to test the engine system setup prior to testing. From these tests, it was determined that the only necessary adjustment to be made was replacement of the low pressure fuel pump. To provide further clarification to this finding, Figure 30 displays a layout of the engine's fuel injection system. The engine's fuel injection has two primary sections: the low pressure pumping system and the high pressure pumping system. The low pressure pumping system is responsible for carrying the fuel from the gas tank to the high pressure system. The high pressure pumping system takes the fuel from the low pressure system, compresses it and delivers it to the engine as an atomized spray. The entire fuel injection system is constantly recalculating since the high pressure fuel system pumps at a much slow flow rate than the low pressure side.

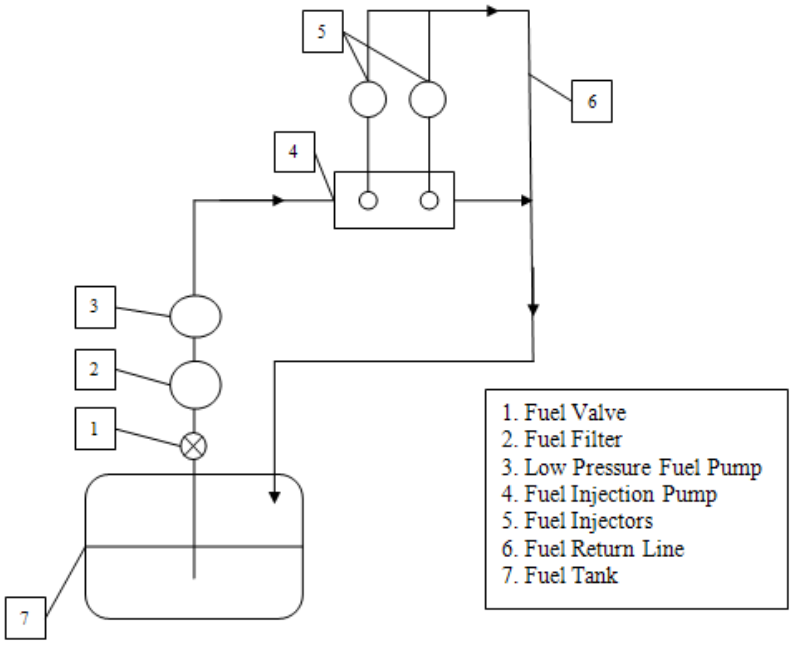

Figure 30. Yanmar 2V750 fuel injection system.

The provided fuel pump was not powerful enough to provide a necessary flow rate of the most viscous fuels to the high pressure fuel injector pump. As seen in Figure 31, a low flow miniature gear pump was purchased to replace the existing fuel pump. This gear pump is capable of pumping less viscous fuels at a flow rate of 0.61 gpm. Upon installing the new gear pump, an engine test was conducted with P084, the most viscous fuel tested to that point. The gear pump was successful in delivering the necessary flow rate of fuel to the engine, resulting in normal engine operation.

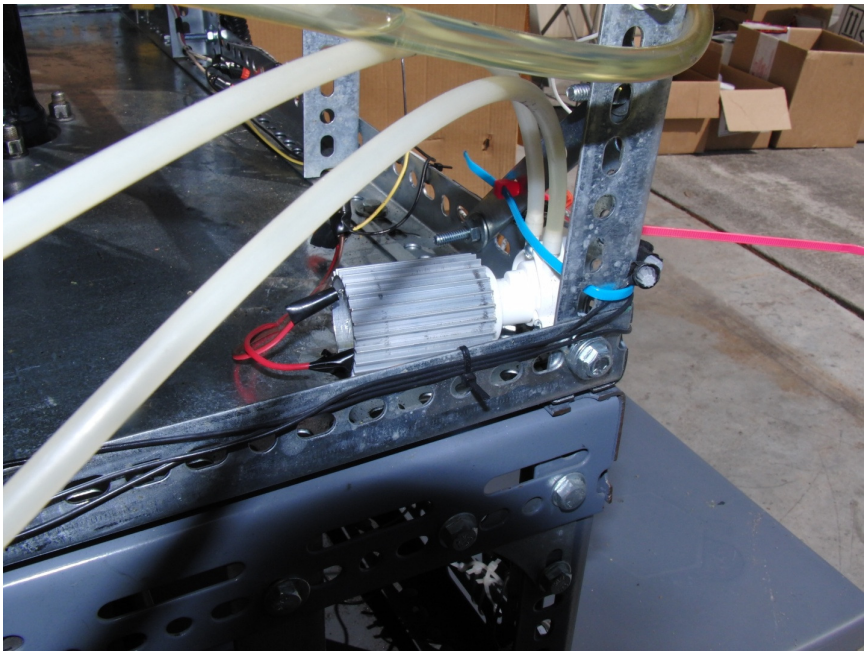

Figure 31. Low pressure fuel gear pump.

Dynamometer

The last step to setting up the engine system to be able to run under load was attaching the dynamometer to the engine. The water brake dynamometer operates by applying a resistive water load to the engine shaft output. The dynamometer is composed of an impeller mounted between two outer plates. The impeller is attached to a main bearing and is free to rotate with the input shaft from the engine. As seen in Figure 32 water is input from an external source into the top of the dynamometer and is circulated through the housing cavity by the impeller, which is connected to the engine input shaft. The input water provides resistance to the impeller, which in turn provides resistance to the engine. Water exits through the two exit hoses with predetermine orifices. The load applied to the engine is increased by adjusting the water flow regulator seen in Figure 34. As the load applied to the engine is increased through greater water flow, the housing begins to torque in the rotational direction of the input shaft. As seen in Figure 33, the dynamometer body is held in place by a torque sensor, which is pinned to the kart frame. As the torque sensor begins to flex, a strain gauge mounted on the center of the sensor detects the load being applied. Using the known moment arm of the torque sensor, the torque applied by the engine could be calculated and used to determine the power output of the engine as well. Engine power output was calculated in horsepower from Equation 20.

$$HP = \frac{torque * rpm}{5252} \quad (20)$$

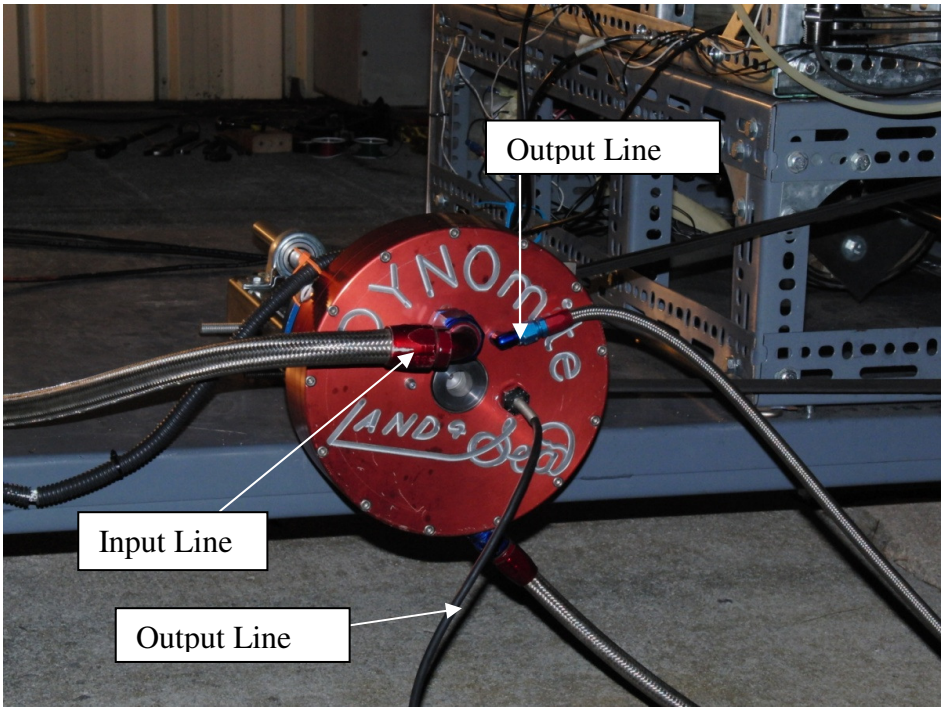

Figure 32. Land and Sea DYNOmite water brake dynamometer. The dynamometer is attached to the final engine testing assembly.

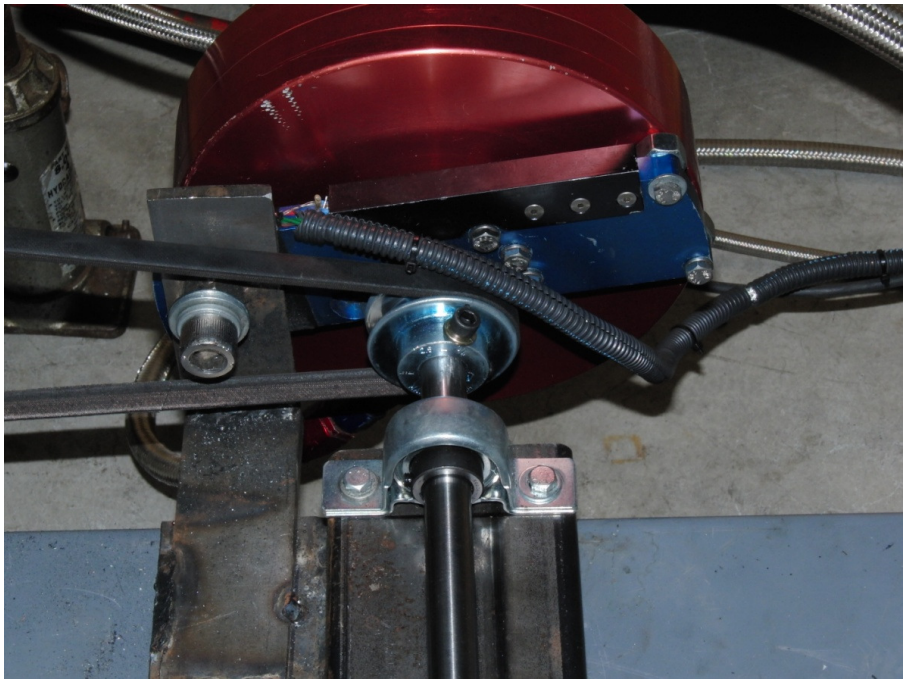

Figure 33. Dynamometer and torque arm assembly.

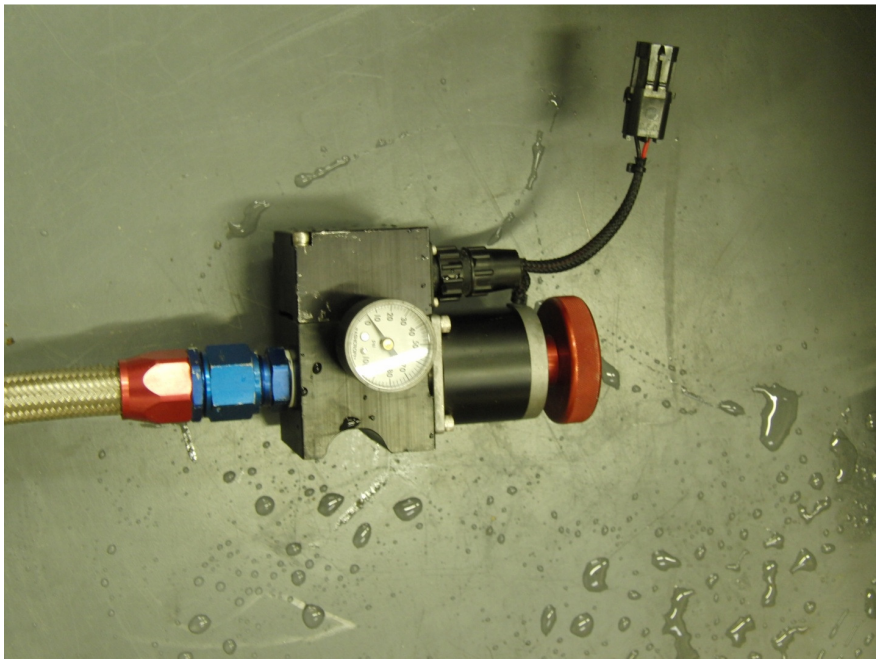

Figure 34. Dynamometer water flow regulator.

The dynamometer used for testing of the Yanmar engine was calibrated prior to testing. The dynamometer assembly was not equipped for computerized automation. Instead, each test was

run manually using these components: a water brake absorber, input and exit hoses, manual load adjustment control and a torque sensor. The torque sensor, as seen in Figure 35, consists of an aluminum body, a strain gauge and the sensor wires. The torque sensor required rewiring of the strain gauge as well as calibration. Upon rewiring, the torque sensor was calibrated and the strain gauge assembly covered with a high temperature silicone sealant.

As seen in Figure 36, the torque sensor was calibrated by hanging weights from the pin hole on the left and reading the change in voltage output by the strain gauge. Since the torque arm is a simple cantilever, the torque for each weight was calculated by multiplying the magnitude by the moment arm, which was located at the top bolt of the three bolt grouping near the center of the arm. In order to amplify the strain gauge signal to an appropriate level, a quarter bridge strain gauge amplifier was used throughout the calibration and testing. Voltage readings were taken from the strain gauge at each load setting and used to generate a torque curve. A linear regression was applied to the generated curve and a calibrated conversion constant was determined.

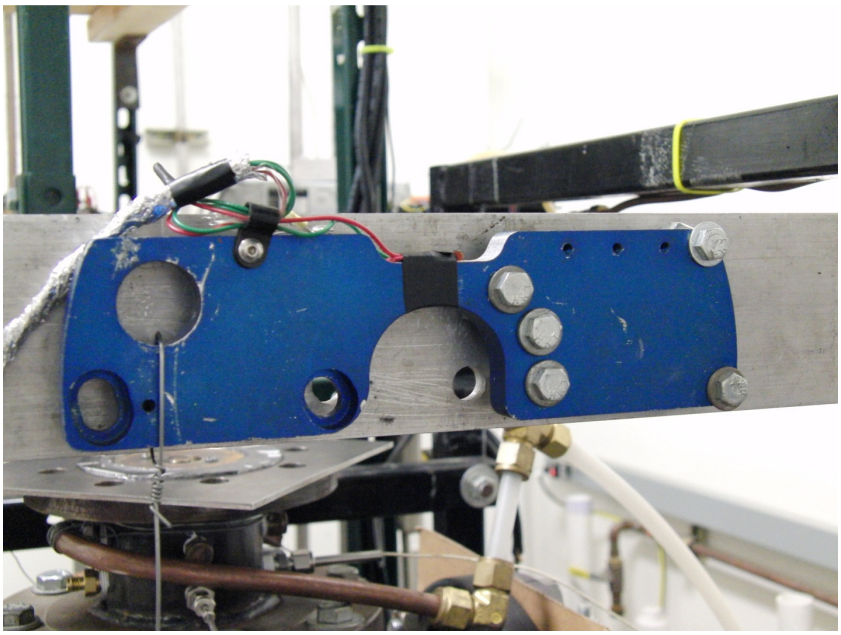

Figure 35. Torque sensor mounted to calibration testing frame.

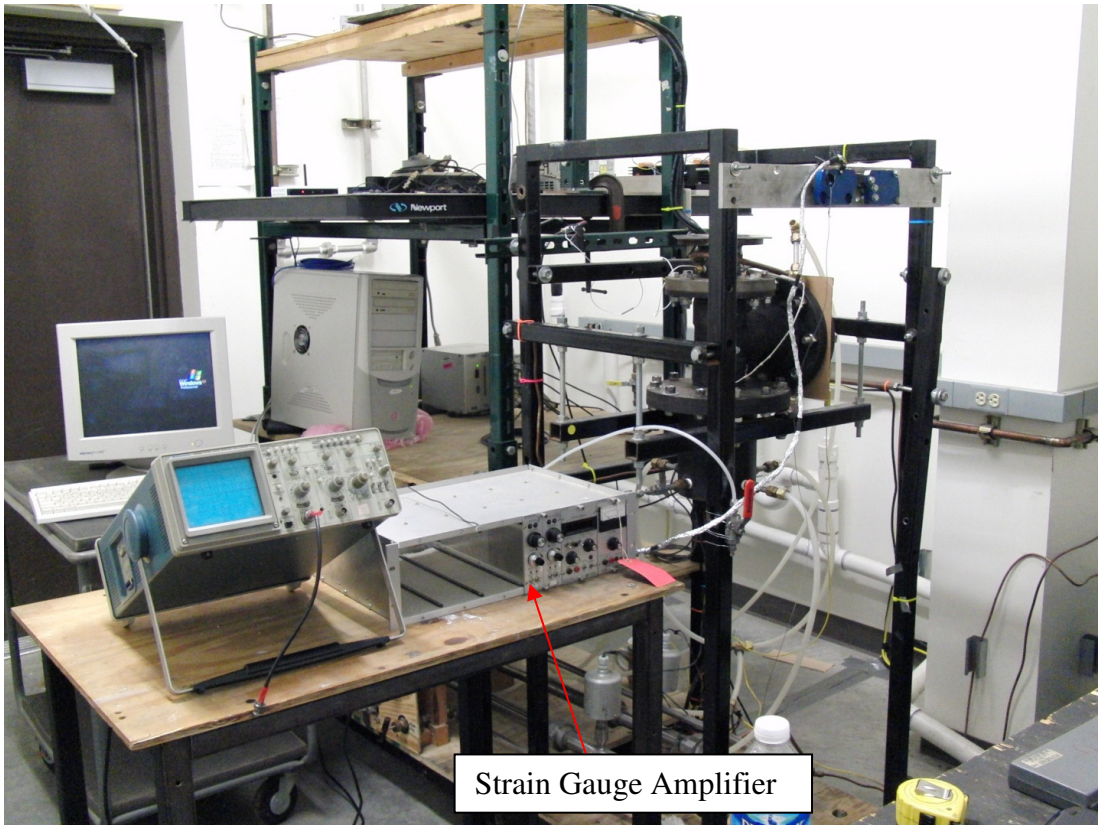

Figure 36. Torque sensor calibration setup.

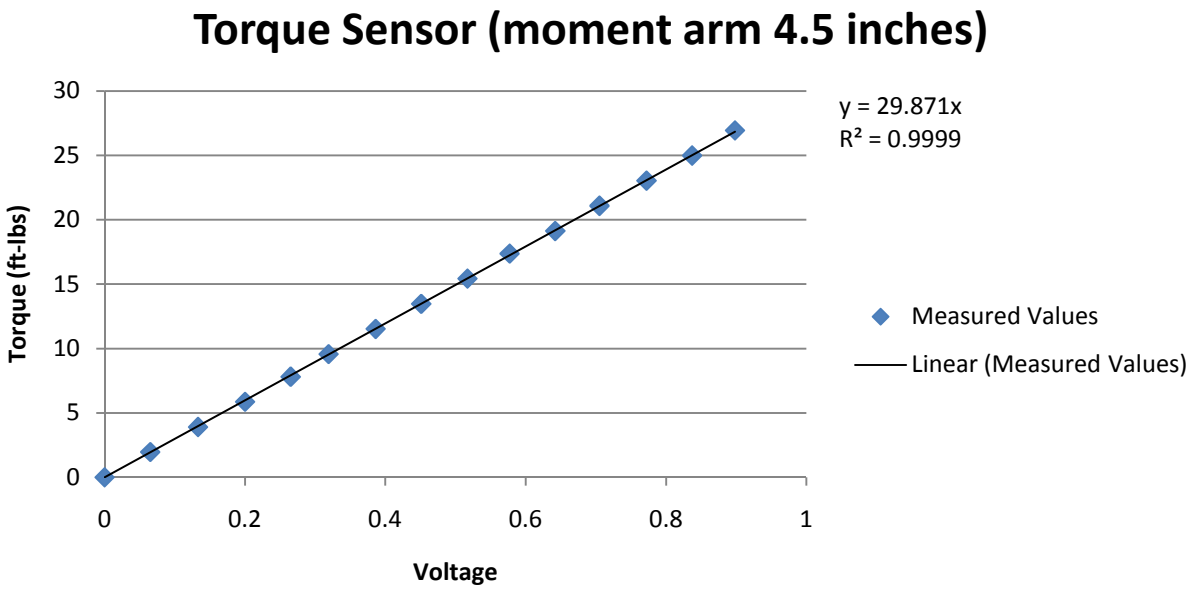

Figure 37. Torque curve generated using DYNOmite dynamometer torque sensor and known weights.

Since the dynamometer requires a horizontal shaft input and the engine is a vertical drive shaft output, a rear differential from a BMW motorcycle was acquired from Cycle Salvage in Dublin, Virginia and used to connect the two devices. As seen in Figure 38, the engine was raised up from its original angle iron mounting box to a second tier composed of the same material. This allowed for the differential to mount underneath the engine via shaft couplings and special mounts designed by the Combustion lab, and machined by the Virginia Tech machine shop. Computer aided designs of these components can be found in Appendix D. The differential was attached to a drive shaft, which rested in a bearing at the end of the angle iron frame centered with the differential hole.

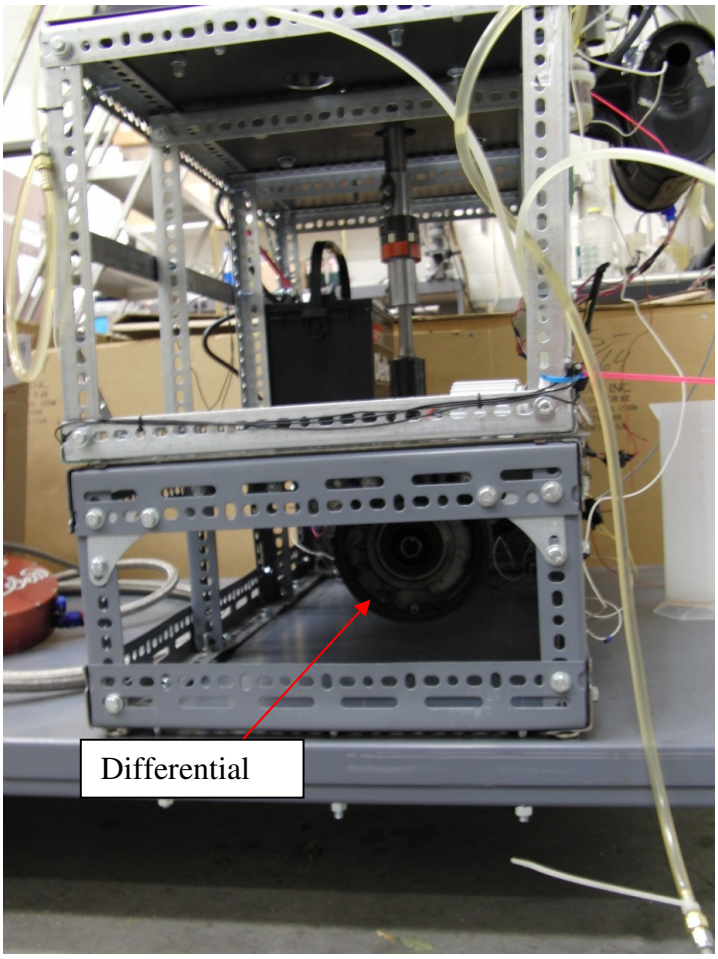

Figure 38. Updated engine kart assembly with installed differential.

The differential was found to have a gear down ratio in its established setup of 4:1, so that for each revolution the engine drive shaft made, the differential output shaft made a quarter of a rotation. As seen in Figure 39, the load curve for the water brake dynamometer, which is available at the Land and Sea website, indicates that the dynamometer requires an input engine shaft speed between 1,200 and 1,500 rpm in order for the absorber to engage, or begin to apply a resistive load. In order to achieve necessary shaft speed to allow the absorber to engage the engine, an external transmission was constructed using a v-belt pulley system. The transmission frame was constructed of two pieces of square stock, welded length-wise next to each other. The frame connected to the kart with four bolts, which rested in two groves cut out of the kart base. Two solid mount ball bearings were secured at the front and back of the frame. A 3/4" drive shaft, which was threaded into the water brake absorber, was fixed between both locking bearings. A pulley was pinned between the end bearing and the absorber and allowed to rotate freely with the drive shaft. A second larger pulley was fixed to the drive shaft on the differential side. Upon mounting the v-belt to the pulleys, a hydraulic jack was used to push the gearbox frame away from the engine until the belt became taught. Locking nuts were screwed into each of the four bolts to secure the assembly for testing. A 7 inch zinc die cast pulley was on the differential side and a high quality 2.5 inch steel pulley was installed on the dynamometer side. The steel pulley was used on the dynamometer side to withstand the high level of torque applied and prevent deformation. This achieved a 2.8:1 gear up ratio, which still resulted in the correct shaft speed needed to operate the dynamometer. The final testing assembly can be seen in Figure 40.

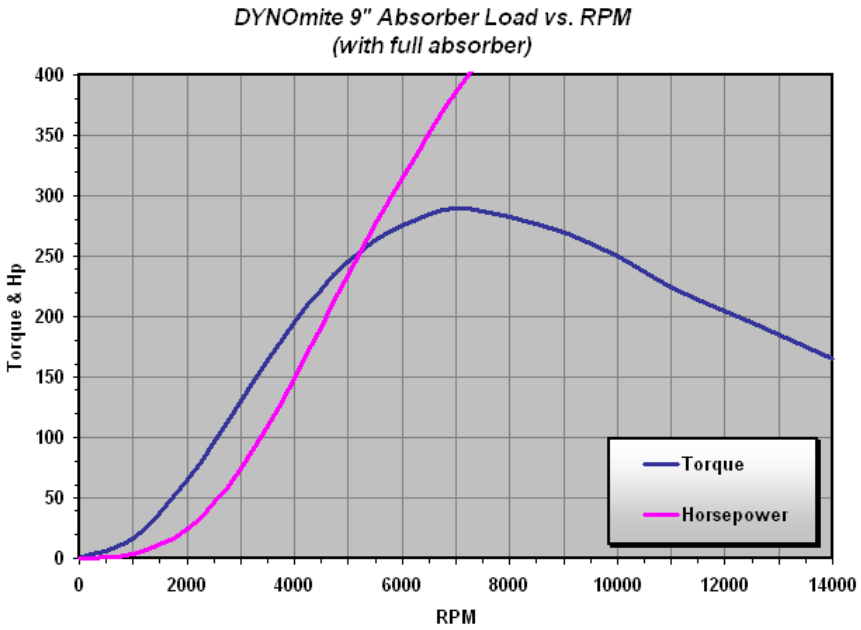

Figure 39. DYNOmite dynamometer load curve. The dynamometer does not begin to apply a resistive load to the engine until the input shaft speed reaches around 1000 rpm. Source: http://www.land-and-sea.com/snowmobile-dyno/DYNOmite%20Snow%20075-150-1K%20Quick-Specs.pdf (under fair use, 2010).

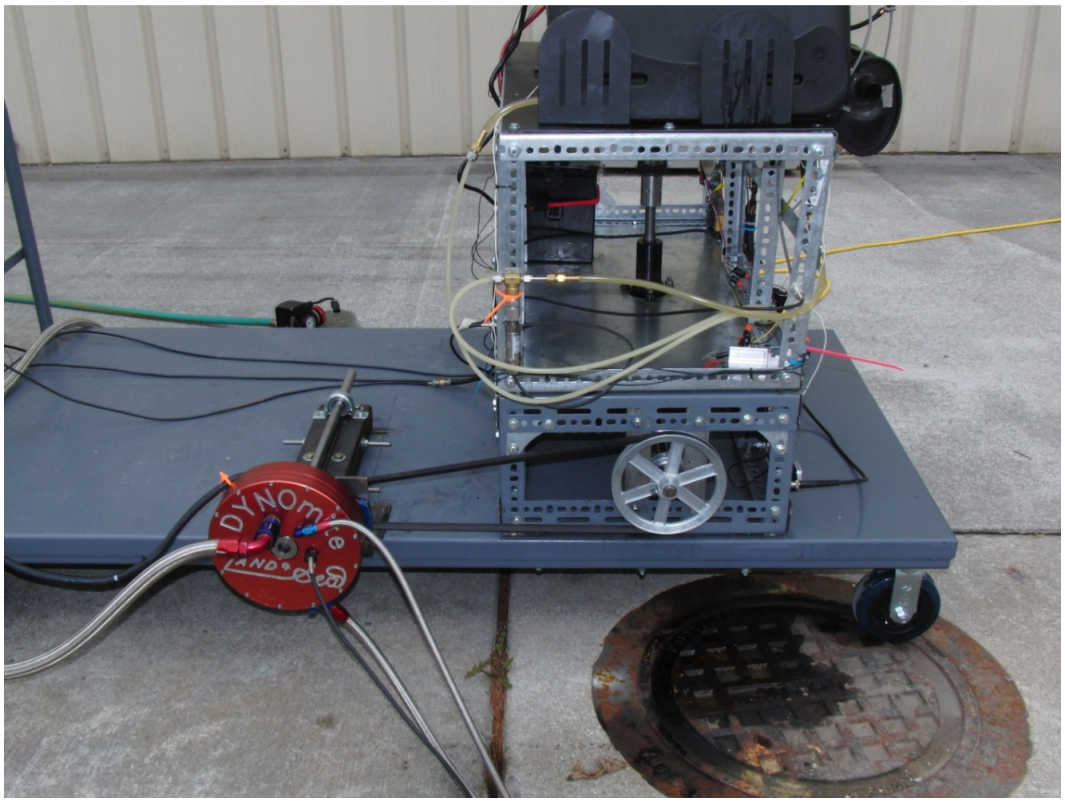

Figure 40. Final engine testing assembly.

Data Acquisition

A National Instruments SCXI data acquisition system was used to capture and record all of the data from each input sensor. For this experimentation, a SCXI-1000 chassis was used to house the data acquisition module. A SCXI 1141 lowpass elliptical filter module was used for data input along with a SCXI 1305 BNC terminal connection block. The complete data acquisition system along with instrumentation can be seen in Figure 42.

Testing sensors included the dynamometer torque sensor, a bicycle tachometer as well as two pressure transducers located at the low and high pressure fuel lines on the engine. Pressure transducers were used to monitor the engine's fuel injection system performed while under load, and potentially diagnose any problems that arose with the engine's performance. The bicycle tachometer was used to determine the engine shaft speed during operation. As seen in Figure 41, a magnet was glued to the drive shaft on the differential side of the gear box and a simple latch sensor recorded a pulse each time the magnet passed across it.

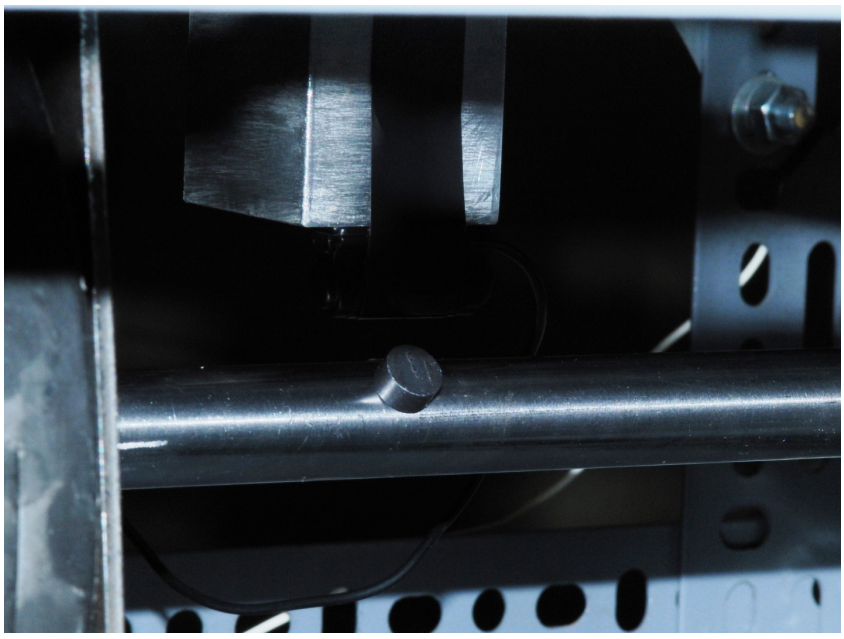

Figure 41. Bicycle tachometer used for tracking engine drive shaft rpm.

Figure 42. Data acquisition system for engine testing.

Procedure

Engine specifications for the Yanmar 2V750 show that the engine is capable of a maximum power of 17 horsepower (hp) at 3200 rpm. Initially, the engine was tested to determine its maximum power output with diesel at the maximum power rpm stated by the manufacturer. From this testing, it was determined that the engine achieved maximum power at 3100 rpm. This rpm level was deemed an appropriate set point and was attempted for each test to ensure a consistent comparison of engine performance for each fuel.

Before comparative testing began, the engine was allowed to warm up on diesel for 10 minutes. A graduated cylinder replaced the fuel tank for these tests. Using the graduated cylinder allowed for easier monitoring of fuel consumption as well as elimination of a potential contamination problem. For each set of tests, 250 ml of fuel was measured in to the graduated cylinder. Depending on the rate of fuel consumption, five to six tests were performed during each fuel run.

Diesel was the first fuel to be tested in order to validate previous results and ensure consistent engine performance. Diesel tests runs were also conducted between each of the other fuel test

runs to ensure that the each fuel was guaranteed of the same initial conditions. If any abnormalities arose in between runs, the problems would be resolved before testing any new fuel. Each fuel was tested in the same manner in the order of Jet A, P184, P186, P117, P129, P130. Between each run, Isopropanol was run through the fuel lines to clean them of other fuel residue. Isopropanol was then mixed with Diesel and cranked in the engine for 15 to 30 seconds to clean the fuel injection pump, high pressure fuel lines as well as the fuel injector and combustion chamber.

During each test, the fuel was allowed to warm up in the engine for 5 minutes. The data acquisition program was then set to record data while the engine was put under load by the dynamometer. In putting load on the engine, the engine throttle was slowly increased while the water input to the dynamometer was also increased. Careful attention was paid so that the engine did not over rev during testing. As the engine began to bog down at 3100 rpm, the throttle was completely opened to allow the engine to reach its maximum power output. Upon reaching maximum power, the engine lost rpm and the throttle and water input were both turned down. Between each test, the engine rested at idle while the water input maintained zero flow.

Engine Power Curves

Since the dynamometer tests did not have the capability of being computerized, adjustments of the load to the engine as well as the engine speed were made by hand. This restricted the type of testing that able to be performed. For this testing, each test was run to determine the peak engine power. As stated in the engine manual, the Yanmar 2V750 is rated for 17 hp at 3200 rpm. From testing with Diesel, it was determined that the peak engine power occurred around 3100 rpm. An example of a typical engine power curve can be seen in Figure 43 for Diesel test 1. A complete plot of power curves for each fuel is located in Appendix D.

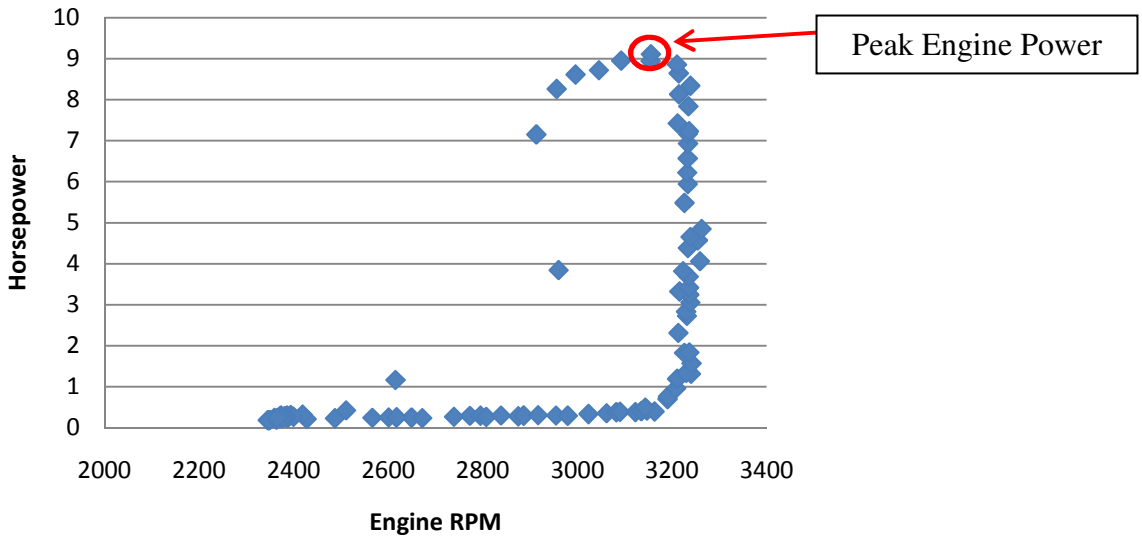

Figure 43. Diesel test 1 power curve

Consistency Measures

In order to ensure the consistency of the engine performance results for each fuel, it was necessary to ensure that each fuel had the same engine conditions. These conditions primarily included properly functioning high and low pressure systems. In order to ensure that the engine was functioning properly before each test, a Diesel test was conducted between each fuel test and compared to an initial Diesel baseline. As seen in Table 1. Diesel engine results between each fuel test., engine maintained proper functioning after each test except for the emulsion fuels P117, P129 and P130. These fuels consistently clogged the fuel injection pump, resulting in loss of pressure and engine power. Measures were taken to clean the engine and restore it to a functioning state prior to new tests.

Table 1. Diesel engine results between each fuel test.

Fuel	HP	RPM	Std Dev
Diesel Baseline	9	3079	0.2
Diesel after JetA	8.5	3138	0.4
Diesel after P184	8.9	3262	0.2
Diesel after	8.4	3160	0.7

P186			
Diesel after P117	5.1	3087	0.00
Diesel after P129	7.1	3090	0.4
Diesel after P130	5.4	2882	0.7

Testing Results

Losses From the Transmission

The engine maximum power output, while operating on diesel, maintained a steady level of approximately 9 horsepower over the course of several tests. These results do not match the peak 17 hp stated in the user manual. This 47% drop in power output can be attributed to several sources. Most of the engine power losses are parasitic power losses, which are losses caused by attaching devices to the engine which use energy generated from the engine. Some of the parasitic losses are used to drive components of the engine which also contribute to the engine's ability to generate energy. Other parasitic devices, such as transmissions, solely take energy from the engine thus robbing the engine of power output.

Most of the parasitic losses in this setup can be attributed to the external drive train attached to the engine, more specifically, the differential. The motorcycle differential is typically used to gear down the engine output provide more torque to the drive wheel. The inner gears of the differential create friction when accomplishing this which promote heat displacement which is lost to the surroundings. Oil displacement within the differential is also a cause of parasitic losses. In terms of the rest of the transmission, much of the remaining parasitic losses are due to energy from heat dissipated in the v-belt pulley system. This system relies on friction between the pulleys and the v-belt in order to function. This friction results in heating of the pulleys and belt which yield heat losses to the surroundings. After running any test, it took several minutes for the belt and pulleys to cool down to the surrounding air temperature. Since the engine was able to maintain a steady maximum 9 hp, it was deemed that each of the fuel tests reflect an accurate comparison with diesel.

Comparison of Results

In conclusion, this proved to be a good preliminary test for operating the fuels in a compression ignition engine under load. As seen in Figure 44, the thicker fuels P117 and P130 provided the most promising results of all of the fire resistant fuels. While running P117, the engine produced an average maximum power of 9.89 hp with a peak value of 10.58 hp. When operating with P130, the engine produced an average maximum power of 8.6 hp with a peak value of 8.92 hp. It should be noted that while testing P130, the engine experienced pressure loss in the high pressure lines. This suggests that the results for P130 do not reflect the full potential of the fuel in the engine. These results do show that the fuel is a viable option as a replacement fuel for diesel in the engine and that it has the possibility for further improvement in engine performance.

Engine operation while running Jet-A averaged a maximum power of 4.6 hp with a peak of 5 hp, which is approximately half the power output from diesel. A possible explanation of these results could be due to the difference in the density, cetane number and distillation curve of the fuels. The cetane number of a fuel is a representation of the fuel's ignition time delay. This delay is the time between the beginning of ignition and the actual combustion of the fuel. Fuels with higher cetane numbers will have shorter ignition time delays than fuels with lower cetane numbers. An investigation into the cetane numbers of both the diesel and Jet-A used for testing is needed to validate this possible explanation. Modification to the timing of the engine could allow for the engine to reach its full potential when operating on Jet-A.

Neither P184 nor P186 were able to generate as much power in the engine as Diesel. P184 testing resulted in an average maximum power of 6.84 hp with a peak value of 7.12 hp. P186 testing resulted in an average maximum power of 5.72 hp with a peak value of 6.32 hp. These results do not rule these fuels out as potential fuels for this engine. JP-8 is currently being used as the primary fuel in the Army's compression ignition engines. The results for Jet-A show that under ideal Diesel operating conditions, the engine peak power was roughly half that of Diesel. Adjustments made to the engine such as the fuel injection timing, spray duration or high pressure line pressure could improve the peak power performance of Jet-A in the engine. Since P184 and P186 produced results between Diesel and Jet-A, there is potential for adjustments to the engine

to increase the performance both fuels. Lastly, P129 did not perform well in the engine. While operating on P129, the engine experienced several misfires resulting in an inability to achieve steady state operation.

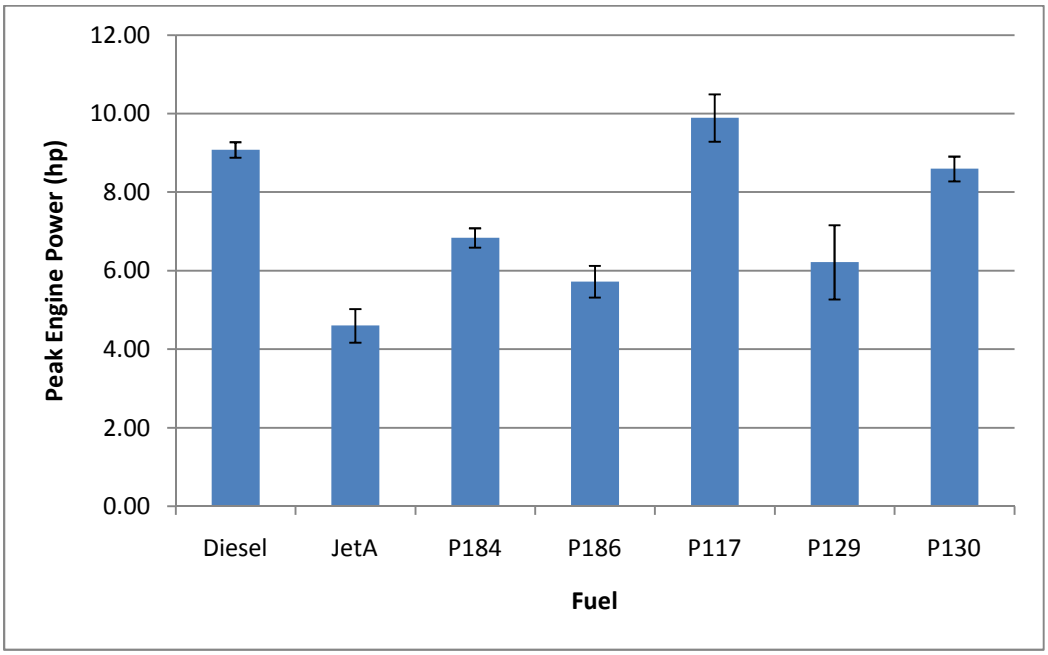

Figure 44. Peak engine power results.

During this testing, several observations were made regarding the effects of the fuel on the engine. Each of the emulsified fuels, P117, P129 and P130, caused a clogging of the fuel injection system located at the fuel injection pump head. These clogs were noticed after operating the engine on each fuel, cleaning the fuel injection system with isopropanol and diesel, and then trying to run the engine again with diesel. During these diesel runs, the maximum power of the engine decreased between two to four horsepower, or roughly 22 to 44 percent of its baseline power level. Also, it was noted that after testing P184 and P186, occasional crystallization occurred in the fuel injector pump head. These occurrences are not visible in the results seen in Table 1. The crystallization led to sticking of one or both of the fuel injector pump heads, inhibiting or halting engine function by restricting fuel flow to the high pressure lines.

Recommendations

Ideally, for this testing, a horizontal shaft engine should be used. This will allow for a direct input to the water brake dynamometer, thus eliminating a need for, and potential losses from a differential as well as a step up gearbox. Also, a full dynamometer kit should be purchased, which includes computer software as well as electronic control of the load input. This will allow for a wider range of dynamometer tests to be run, such as steady state testing or sweep testing. Also, this will allow for more consistent tests to be performed since human error will be minimized.

If more tests are to be run with this design certain aspects should be changed to optimize the engine output and fuel performance consistency. First, in order to maintain the life of the gearbox as well as reduce some of the losses, the pulley sizes should be changed to a 10 inch steel pulley on the differential side and a 4 inch steel pulley on the dynamometer side. In order to reduce any potential losses due to slipping of the belts, a chain link sprocket system should be implemented.

In order to maintain fuel performance consistency, a more effective means of cleaning the engine between fuels must be established. It should be noted that each of the thicker fuels caused the engine fuel pump pistons to slightly seize up, thus restricting flow of fuel into the engine. In order to properly clean requires removing the entire fuel injection system and cleaning individual pieces with Isopropanol and Diesel. Two possible recommendations are to either design a better fuel injection system to handle such fuels. This could be as simple as installing two new springs around the pistons with higher stiffness values which would make them more reactive to the fuels. The second solution could be a solvent that could be pumped through the engine occasionally to breakdown buildup or incorporated into the fuel so that it is constantly running through the engine, preventing buildup from occurring.

Lastly, longevity testing must be completed in order to analyze how these fuels perform in an engine under regular wear and tear and if more adjustments must be made or ultimately if the fuels are completely viable.

Chapter 6 - Rotary Atomizing Mist Characterization System

Introduction

In order to classify the sample fuels as potential fire resistant fuels, a test was developed to simulate their exposure and reaction to a combative situation. There are numerous combat situations in which the fuel of an American military vehicle can become a potential threat to the safety of the vehicle and its inhabitants. In order to test the generic fuel characteristics applicable to some of these potential situations, a rotary atomization mist characterization system has been developed. This experiment allows us to analyze the spray as well as ignition characteristics of each of the Luna sample fuels in comparison to those of Diesel and Jet A under repeatable conditions.

Testing of each fuel's fire resistance potential has been divided into two categories; characterization testing of atomized sprays as well as fuel ignition testing. Characterization of the fuel sprays will focus on qualitative analysis as well as determination of the spray angle from exit location, droplet diameter as well as droplet velocity. Common methods for determining droplet size distributions include static laser diffraction, Phase Doppler Particle Analyzers and PMS optical array probes. For this analysis, droplet diameter will be evaluated at a set distance of approximately 0.035m from the disk exit orifice. The droplet instantaneous velocity will be determined over the course of the droplet lifetime.

Ignition testing for each fuel will be used to both qualitatively judge the ignitability of each fuel as well as potential flame propagation rates. Each test will involve a set volume of fuel and will be continuously recorded for the entire life of that fuel. Results will be correlated between atomization characteristics as well as ignitability in order to evaluate each sample fuel's fire resistance potential.

Nomenclature

Droplet Blur Technique

Symbol	Units	Description
DC	inches	Disk circumference about edge of tape
D	inches	Diameter about edge of tape
LV	inch/sec	Linear velocity at edge of tape
Delay	sec	Image time delay or time taken to capture
B	inches	Blur length on fuel stream
DD	inches	Droplet diameter
V	m/s	Droplet velocity

Drag Model

m	kg	Droplet mass
V	m/s	Droplet velocity as a function of time
F	N	Force acting on droplet
D	N	Drag force acting on droplet
C_d	Dimensionless	Coefficient of drag
A	m^2	Area of droplet
ρ_{air}	kg/m^3	Density of air
C	1/m	Equation constant
t	sec	Time
S(t)	m	Position as a function of time
S_o	m	Initial position
V(t)	m/s	Instantaneous velocity as a function of time
V_o	m/s	Initial instantaneous velocity

Literature Review

Rotary atomizers, in their general sense, are liquid fed rotating elements that utilize centrifugal force to spread out and eventually break up liquid streams into droplets. The concept of centrifugal, or rotary, atomization has been discussed and studied by several researchers including Lefebvre [14], Karim and Kumar [15] and Hewitt [16]. Lefabvre [14] discusses that there exist several different types of rotary atomizers. Common types that are used today are vanned disks, which have guide channels open on the top that are either radial or curved, flat disks, cups, or slotted disks with confined channels that run through the disk.

The most common application for rotary atomizers have been found in the agriculture industry in crop spraying and aerial distribution of pesticides. Lefebvre [14] discusses that other applications include spray drying of particles as well as fuel injectors for heat engines. The most common example of this is the one developed by the Turbomeca company in France for use in a gas turbine engine.

The rotary atomizer test was chosen for this experimental study because it is relatively easy to control the particle size and velocity by adjusting the speed of the disk. The setup of the test stand for this experiment was modeled after the design developed by the Naval Research Laboratory (NRL) [17]. The NRL has performed droplet characterization testing in an effort to measure the mist flammability characteristics of Jet fuel. Along with this setup, the NRL used a Malvern Spraytech light scattering device to measure the Sauter Mean Diameter of the fuel droplets. The NRL also utilized their setup to perform testing to study the flammability characteristics of the fuel aerosols generated.

Test Setup

The foundation for the design of this apparatus was modeled after a design developed at the Naval Research Laboratory. As seen in Figure 45, the design is relatively simple. A router motor is located in the middle of a sheet metal base and a quarter inch steel platform. The motor is attached to a specially designed disk, seen in Figure 46. Fuel is poured from above into the cavity of the disk, where the centrifugal force from the disk forces the fuel through four quarter inch thru holes and out of the disk. This slinging of the fuel through a small orifice causes

atomization at high speeds. The design also called for a sheet metal shield that fit just inside the sheet metal base to contain the fuel being tested, which can be seen in Figure 47.

To ensure the uniformity of the film thickness during atomization, and with that a more uniform droplet size, three criteria were met before testing. The first is that the disk rotation was tested and determined to be vibration less. The second is that the thru holes were determined to be smooth. The last criteria is that the centrifugal force is known to be greater than the gravitational force.

Figure 45. Original NRL atomizer design [17] (under fair use, 2010).

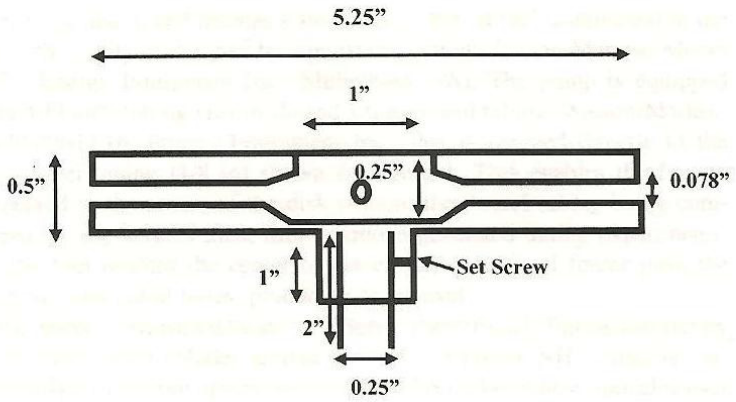

Figure 46. Disk specifications and design [17] (under fair use, 2010).

Figure 47. Original Atomizer design with shield [17] (under fair use, 2010).

Atomization Testing

A Casio EX-F1 high speed camera was provided for image capture of atomized sprays. Initial image capturing efforts were focused on determining the appropriate camera and disk speed settings to properly capture the fuel spray. Disk speeds were tested between 12,000 rpm and 8,000 rpm. A Shimpo 205L tachometer was used to measure the disk speed. The camera's on

board flash, which was rated with a maximum shutter speed of 1/1000 seconds, was used to freeze the disk in the image. In Figure 48, an attempt was made to freeze the disk spinning at 10,000 rpm. This was unsuccessful for several reasons including disk speed, the shutter speed setting as well as the f-stop setting.

The camera settings were optimized by minimizing the shutter speed, which removed the blur from the object, lowering the f-stop setting, which helps to increase the lens speed of the camera by delivering more light intensity to the focal plane, and setting the ISO to between 200 and 400. The ISO setting on the camera is an indication of how sensitive the image is to light. By setting the ISO to a lower number of 200 or 400 as opposed to 800 or 1600, the image is less sensitive to light and in result much clearer. It was also determined that in order to capture a still image of the disk at these camera settings, the disk speed must not exceed 8,500 rpm. As seen in Figure 49, a successful image was taken at 8,000 rpm under optimal camera settings.

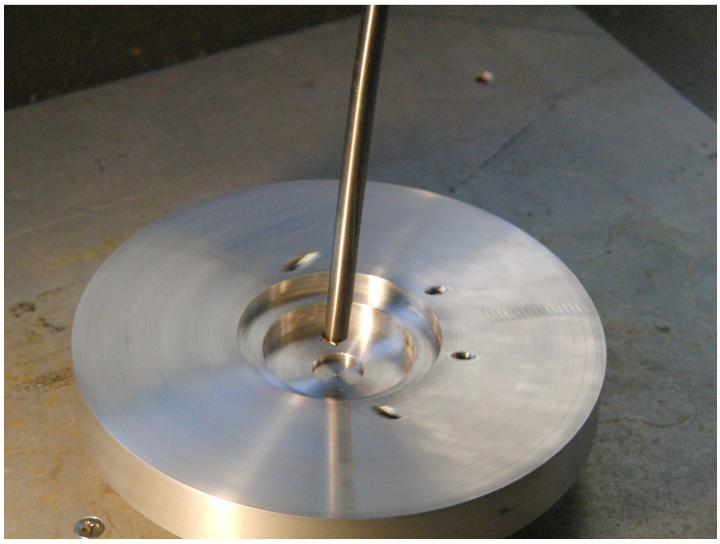

Figure 48. Initial image capturing effort at a disk angular velocity of 10,000 rpm.

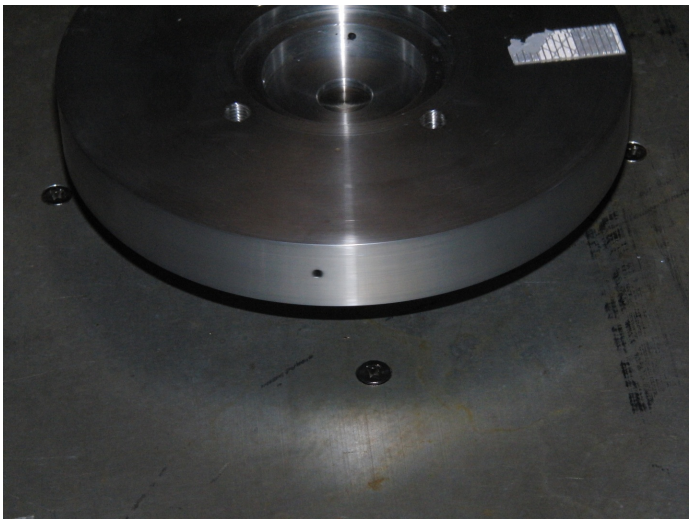

Figure 49. Image of disk spinning at 8000 rpm.

As seen in Figure 50, an external camera mount was constructed using 1/8" angle iron bars welded together at the joints. The mount allowed for the camera to be positioned overtop of the area of interest without being influenced by the vibrations on the main body.

Figure 50. Angle iron camera mounting frame.

Also, a Hamamatsu L4633 converging type Xenon flash lamp, seen in Figure 51, was purchased to replace the onboard camera flash. Compared to the onboard camera flash, the external Xenon

flash lamp allowed for higher quality images for two primary reasons. First, the flash lamp eliminated the glare produced by the onboard camera flash which reflected off of the disk's metal surface. Without this glare present, fuel streams became more easily recognizable due to increased contrast in the image. Secondly, the flash bulb produced a higher intensity, shorter duration flash than the onboard flash. This allowed for increased image clarity through elimination of blur. The pulse duration of the flash bulb is one micro second, whereas the maximum camera shutter speed with the onboard flash is one millisecond with a maximum flash pulse duration of 50 micro seconds. This equates to the 0.051 degrees of disk rotation during the xenon flash pulse and 2.55 degrees of disk rotation for the onboard flash pulse at an angular velocity of 8500 rpm. Along with the flash bulb, a C3684 power circuit as well as a E4370-01 trigger circuit were purchased.

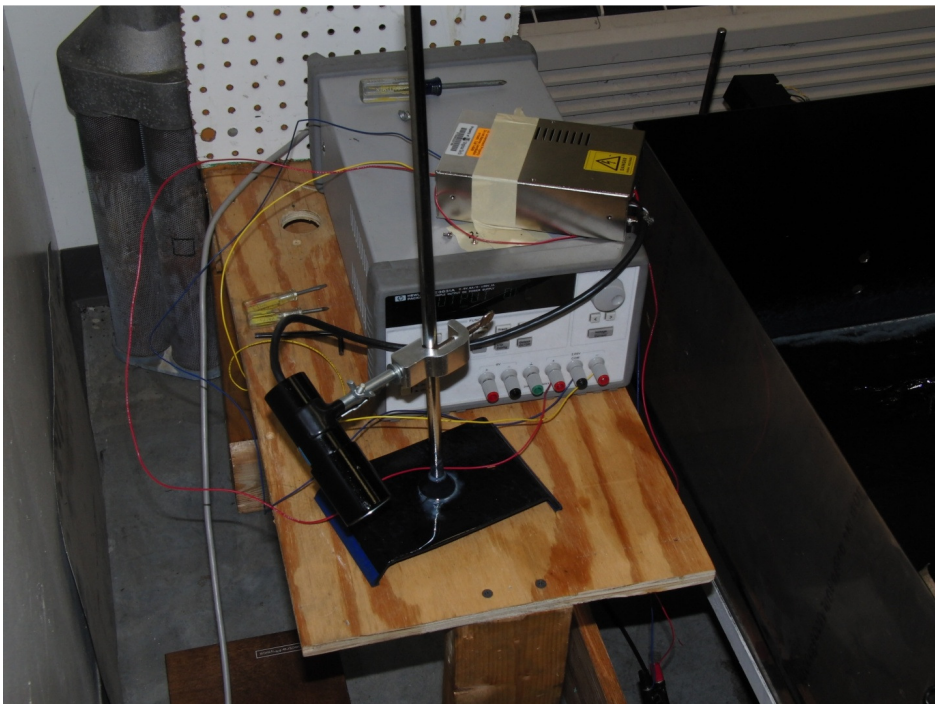

Figure 51. Hamamatsu L4633 converging Xenon flash bulb with power supply and trigger circuit.

Lastly, adjustments were made to the testing setup in order to capture images of each fuel exiting the disk in the same location each time. This allowed for consistent and easier image analysis of each fuel. In doing this, a triggering system was designed that comprised of three primary sections.

Timing and Synchronization Method

This section will outline the timing and synchronization method and testing setup used for image capturing of fuel streams. Further details of triggering inputs and outputs, as well as a circuit diagram are included in Appendix I.

Laser

A laser system was constructed to initiate the triggering system. As seen in Figure 53 and Figure 57, a laser was shown through a hole in the shield wall onto the disk surface. A piece of reflective tape was attached to the disk surface as well. Upon contact with the laser, the reflective tape relayed the beam across the apparatus through another hole in the shield wall to a photodiode seen in Figure 52. During operation, the photodiode output a voltage signal which corresponded to level of light input to its sensor. Input beams from the laser increased the level of light recognized by the sensor, thus increasing the output voltage signal a set amount. Rapid laser beam inputs to the photodiode from the rotation of the disk generated a rectangle wave voltage output which is then sent to the triggering circuit. Since the output voltage signal is not large enough to be recognized by the circuit on its own, the signal is conditioned by a Vishay 2300 voltage conditioner.

Figure 52. Photo diode for recognizing laser impulses. Upon recognizing the laser signal, the diode sends a signal to the circuit.

Figure 53. Laser for timing circuit.

Triggering Circuit

The circuit developed for the triggering system was designed and constructed by Dr. Christopher Martin from the Virginia Tech Dynamic Systems Combustion laboratory. The circuit, and its outer casing, can be seen in Figure 54 and Figure 55. A detailed description along with a wiring

diagram can be found in Appendix H. When armed, the circuit reads the input voltage from the photodiode. When the photodiode signal peaks at approximately 12 volts, the trigger circuit engages and sends out a voltage signal to the external flash triggering it to pulse a single flash. Since the signal is dependent on the laser passing across the tape, the flash triggers and freezes the same spot on the disk each time within a couple degrees due to changes in disk speed. Images were taken with a ruler near the disk so that during image post processing, the pixel count can be converted to real distances. Along with the xenon arc lamp, tests were also performed with a Sunpak 433 D external flash with an aperture of f/16. The resulting images show measurable lengths of blur associated with each fuel droplet. These droplet blur have been utilized to determine droplet diameter as well as the instantaneous velocity of the leading edge of the droplet stream curve. The overall test setup can be seen in Figure 56.

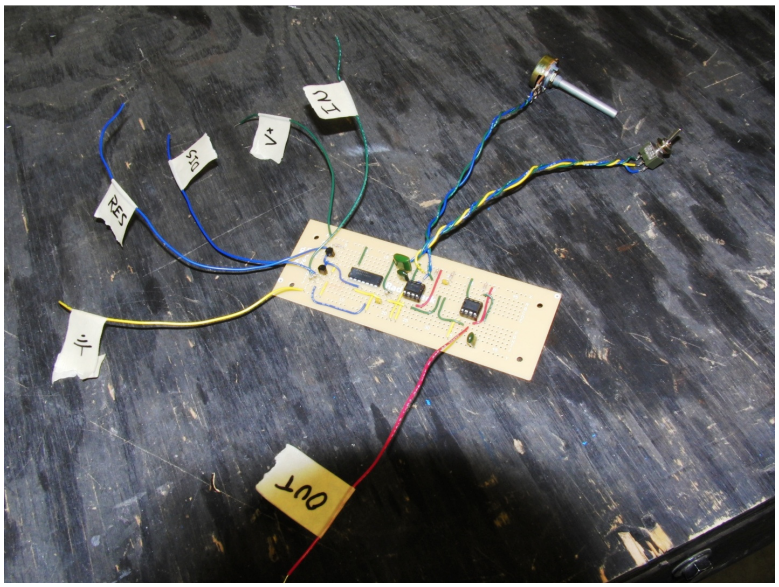

Figure 54. Internal components of trigger circuit.

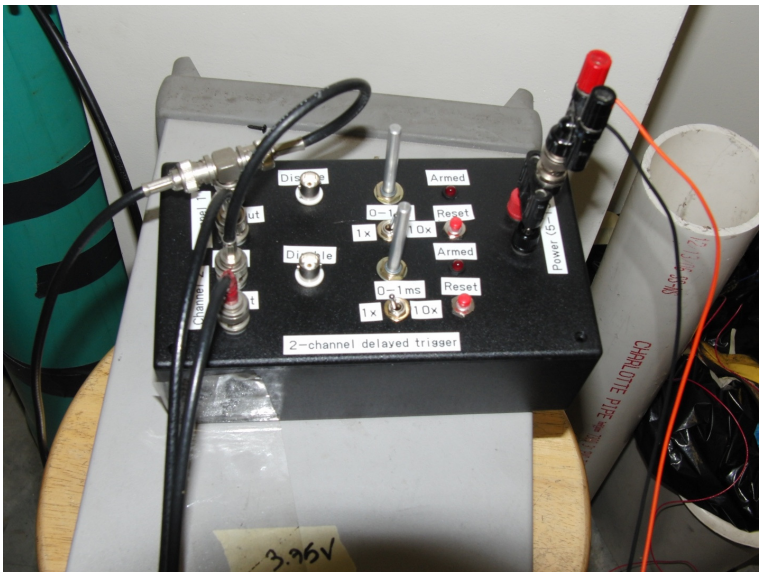

Figure 55. Trigger circuit for image capturing system.

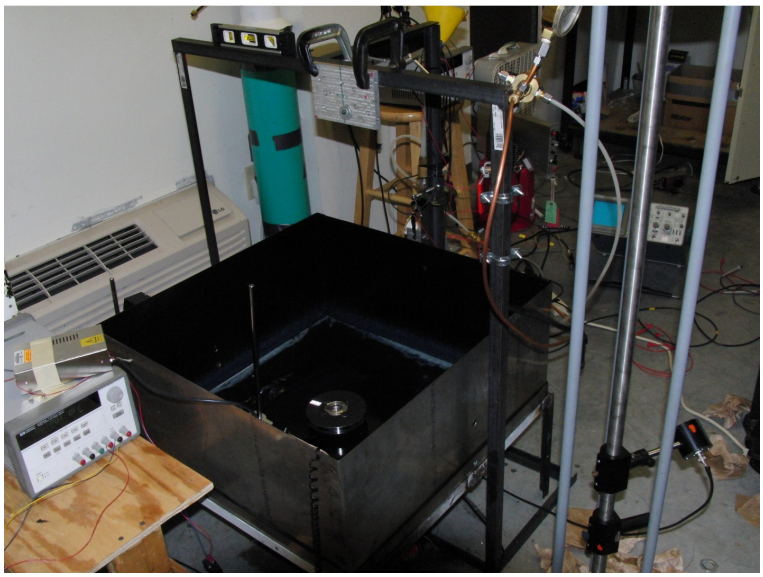

Figure 56. Atomizer setup for image capture of each fuel.

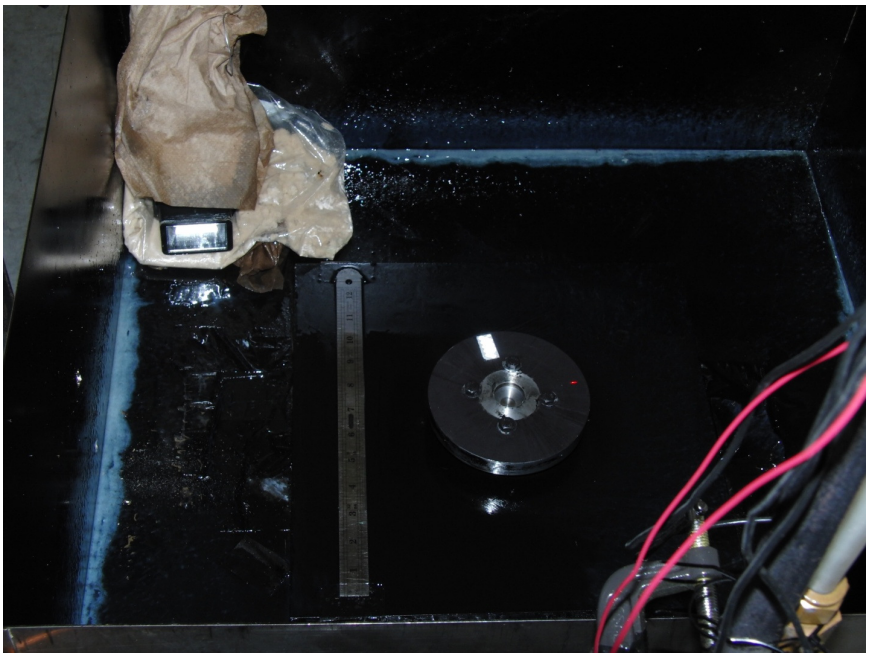

Figure 57. Atomizer design with low speed flash.

Potentiometer

The potentiometer seen in Figure 58 was used to control the router motor. This potentiometer relayed a very steady voltage signal into the router motor allowing for a precise and relatively constant disk speed. In order to capture the image with the disk in a relatively constant position, the speed must be relatively constant. The disk speed was monitored and noted before each test was run.

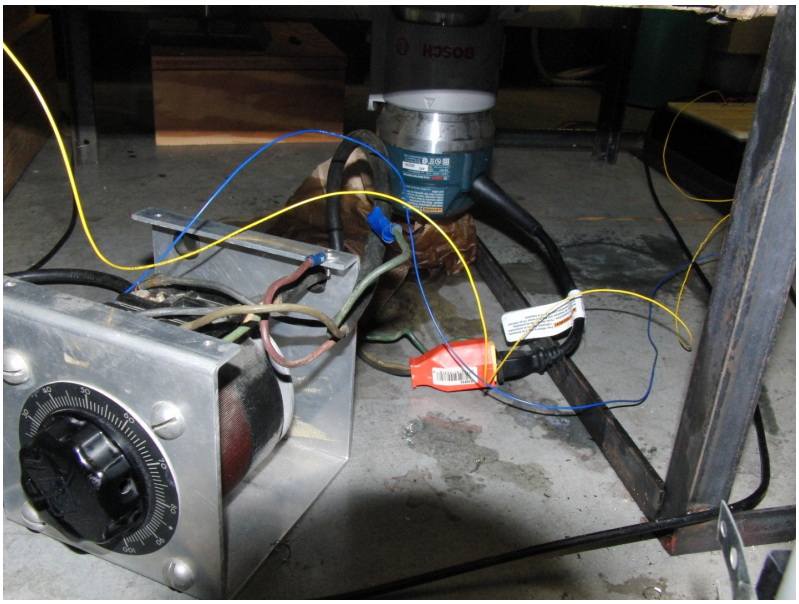

Figure 58. Router motor and potentiometer.

Ignition Testing Setup

The second half of the flame resistance testing was fuel ignition testing. Two primary modifications were made to the system when constructing the testing setup. The first modification was a fuel delivery system. Due to the safety risks involved in creating a high speed rotary ignition, it became necessary to develop a time delayed fuel delivery system. Initially, the delivery unit was a gravity feed system composed of a funnel and a tube located above a two-way ball valve. On the lower end of the ball valve is a copper tube which leads the fuel down into the center of the disk. Upon testing the system with more viscous fire resistant fuels, it became evident that a pumping system would be needed in order to supply enough fuel to the disk. As seen in Figure 60, the final fuel delivery system contains the same low flow gear pump used on the low pressure side of the engine. As the current system is setup, fuel is poured into the funnel and then is pumped by the miniature gear pump through a recirculation system. When the test is ready to run, the valve is opened allowing the fuel to pump down into the disk.

The second modification to the system was the incorporation of an ignition source. This was achieved by securing a propane torch through a hole drilled in the base of the metal frame. As seen in Figure 59, the center of the flame was kept at four and a half inches from the edge of the

disk for each test. This distance was experimentally determined as the necessary distance the flame needed to be from the edge of the disk for Jet-A to ignite with a disk speed 8,500 rpm.

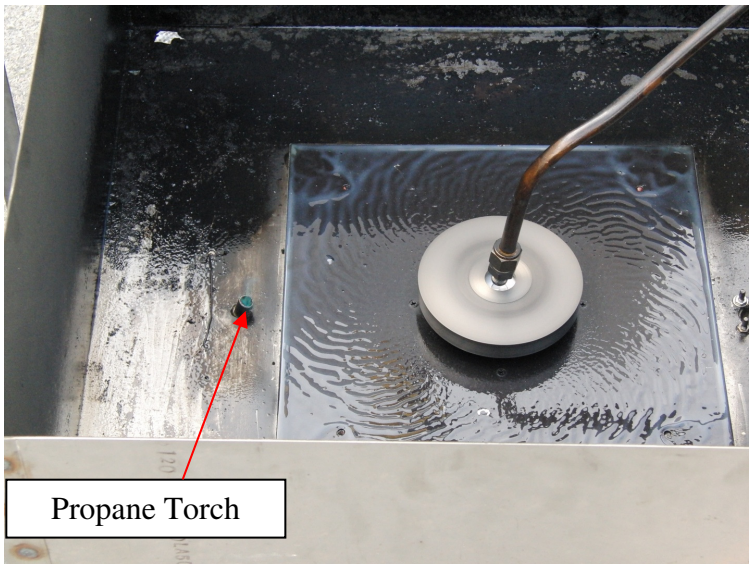

Figure 59. Propane torch used for ignition testing.

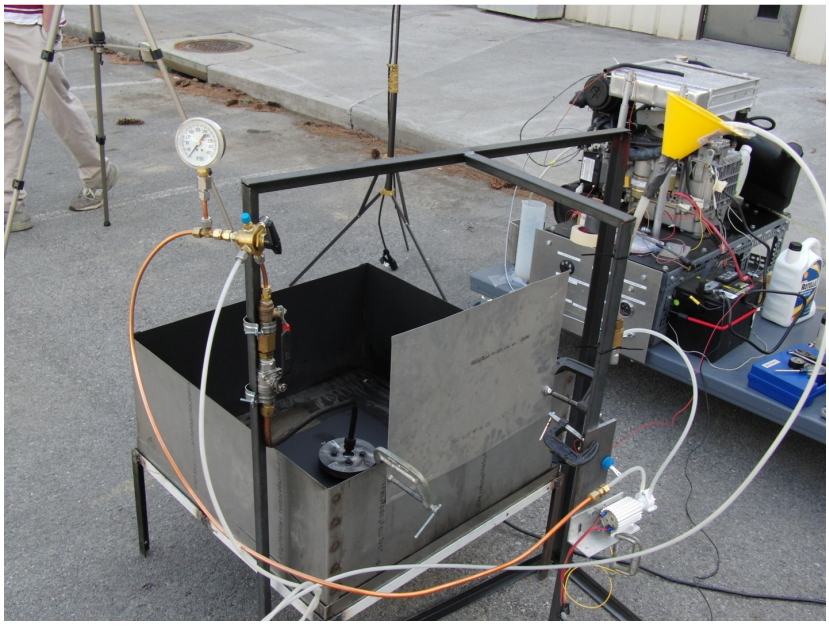

Figure 60. Atomizer setup for ignition testing.

Procedure

In running image capturing atomization tests, the first step was to turn on the potentiometer and setting the router motor at the desired speed of 8500 rpm. The laser was then turned on and the circuit and flash were powered. The camera was then focused on the same plane as the exit holes on the outside of the disk. Lastly, an approximate amount of fuel was placed into a pouring cup.

These tests were run by two people; one person was in control of the fuel, pouring a small short pulse of fuel into the cavity of the disk while the other person was in control of the camera and the flash. The automated pouring setup was not used because the input piping would be in the way of the laser across the disk top. An open shutter image capture technique was used for this testing. The camera was set to leave the shutter open for one second and capture the image during that time. The operator of the camera counted down from three to zero. As the operator reached one, the camera record button was pressed and as zero was reached the fuel was poured and the circuit button was pressed setting the flash off. Sets of five tests were run for each fuel for both the Hamamatsu xenon arc lamp as well as the Sunpack flash. Images were reviewed to ensure that each was of quality and results for each flash for Diesel test 1 can be seen in Figures 61 and 62.

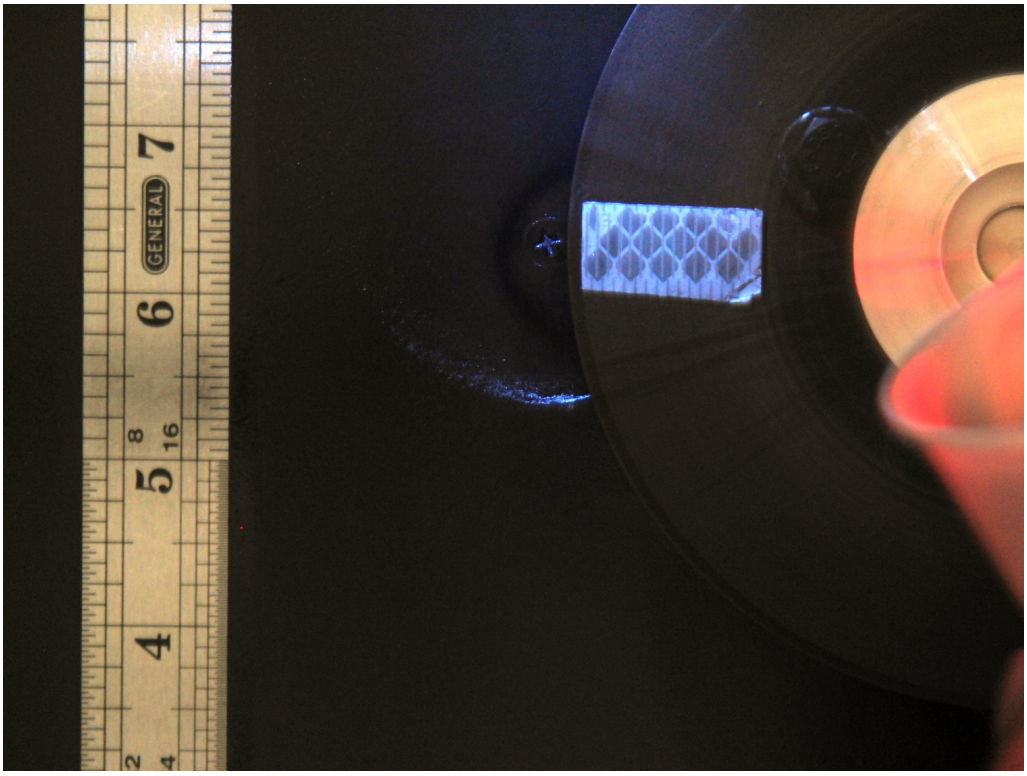

Figure 61. Diesel Test 1 using the Xenon arc lamp external flash.

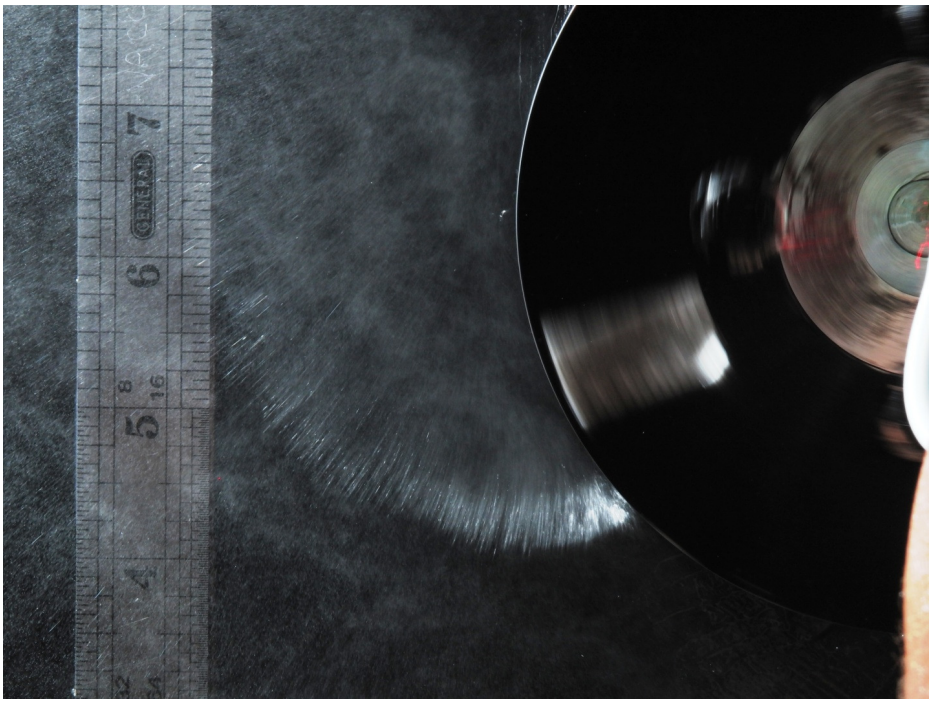

Figure 62. Diesel Test 1 using the Sunpack 433D external flash.

For the ignition testing, the potentiometer was set to the desired disk speed and verified with the hand held tachometer. Fuel was inserted into the fuel line and the gear pump was initiated to cycle the fuel through the delivery system. Two cameras were used for this testing. Both were located near the apparatus. One was used to take high speed video at 1200 fps during the run, while another took standard definition video so the test could be observed at real speed. Tests were initiated by beginning the both camera video captures and then routing the fuel to the disk. The video was recorded and analyzed later. Ignition tests were run at 8500, 11000, and 13500 rpm. Results can be found in Appendix H.

Fuel Stream Angle Calculations

The fuel stream angle for each fuel has been calculated using the images taken with the Xenon arc lamp. Within MATLAB, each image was uploaded to the workspace and calculations were made using the imtool function. For the purpose of this comparative test, the fuel stream angle is the angle between the radial vector at the current state of the disk exit orifice and what is deemed the observable end of the fuel stream in the image. Within imtool, lines are drawn from the disk exit to the end of the stream as well as along the radial slope at the disk exit point. As seen in Figure 63, a line is then drawn vertically to connect the two. A final line is drawn from the disk exit point to intersect the vertical line. Using the known distances of the lines drawn as well as the law of cosines, the desired angle is determined.

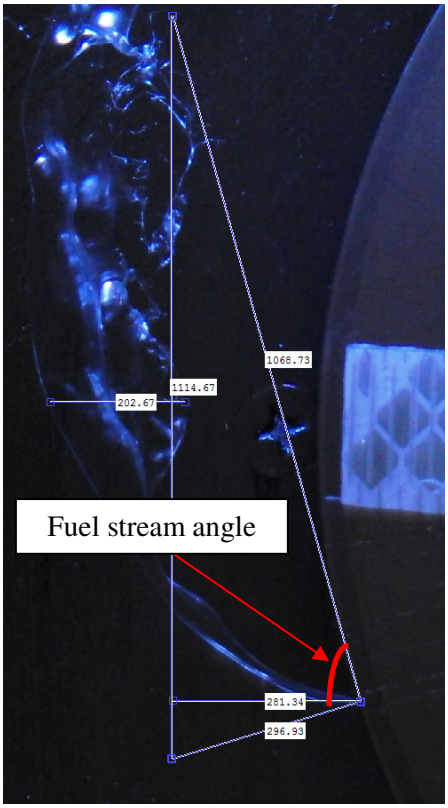

Figure 63. P130 image processing to determine spray angle.

Droplet Diameter and Velocity Calculations

Each of the techniques used to determine droplet diameters as well as velocity analyze the images taken with the SunPack external flash. These images allow for such analysis techniques due to the blurring of each fuel droplet along the fuel stream, which occurs due to the slow pulse duration of the flash. Lastly, only the fuels that were able to properly atomize, which in this case exhibited Newtonian characteristics and were assumed to be Newtonian fluids, were analyzed with these techniques. These fuels, which atomized into droplets, formed approximately linear blurs along the droplet spray path. The non-Newtonian emulsion fuels tested formed ligaments upon exiting the disk, which could not be analyzed with these techniques due to their complex spray paths.

Blur Technique

For the analysis of each test, MATLAB's image processing toolbox was used to determine droplet diameter, spray angle as well as image blur lengths. Calculations for the droplet velocity were split into two parts. The first area of focus was to determine the time delay experienced in the image. The time delay, or the time between initial image capture and final image capture, can be seen in the blur or elongation of noticeable elements in the image. The time delay of the image was determined using the piece of reflective tape on the disk surface. The location and size of the tape was known. The disk circumference was calculated using equation 21,

$$DC = \pi * D \tag{21}$$

where D is the diameter generated about the edge of the tape closest to the disk edge. The linear velocity at the edge of the tape is calculated from equation 22.

$$LV = RPM * DC \tag{22}$$

Lastly, the time delay is calculated using equation 23,

$$Delay = B/LV \tag{23}$$

where B is the blur length determined on the outermost edge of the tape. After determining the time delay in the image, it is applied to the droplets in the fuel stream to determine their linear velocity. Four droplets were selected from each test at a distance of 800 pixels or 1 2/3" from the disk exit point along the fuel stream. Between the four droplets selected, an average droplet blur was determined using each individual droplet blur calculated from equation 24,

$$DB = L - DD \tag{24}$$

where L is the total droplet length and DD is the droplet diameter. The droplet is assumed to be spherical and the diameter is determined to be the width at the end of the leading edge of the

stream. The average velocity of the droplet is then calculated using equation 25. Example calculations, results and code can be found in Appendix H.

$$V = DB/Delay \tag{25}$$

Angle Technique

A second velocity calculation method was originally explored to provide validation of the results determine using the blur technique. This method has proved to be more consistent than the blur technique at calculating the average velocity of the droplet due to the fact that there is less human error involved. This technique is also believed to be more accurate than the blur technique, but this assumption would have to be verified by another known droplet characterization test, such as a PIV. Known as the angle technique, this method has become the primary means to calculate the droplet diameter, position along the leading edge, instantaneous and average velocities. A MATLAB code was used to perform each of the necessary calculations. An example of the code used for Diesel fuel can be found in Appendix H.

The angle technique operates under the primary assumption that the droplets travel in a linear fashion upon exiting the disk. For this testing, four streams spread along the leading edge have been analyzed for each image. The droplet diameter for each stream is calculated in the same fashion as the blur technique. Within MATLAB, two location points are provided to the code for each stream. The location points are used to define the angle of the stream and the bottom point is always at the end of the leading edge of the stream. A line is then drawn from the droplet along the stream angle until it intersects the edge of the disk at the location where the fuel first exited the disk orifice. A curve is then generated between the intersection point created at the edge of the disk for the fuel stream and current location of the disk exit orifice.

Using the rotational velocity of the disks, the time taken for the disk to travel between exiting that particular fuel stream and the final location in the image is determined. This time is also the same time taken for the fuel stream to travel from the disk exit orifice and its current location in the image. Using both the time calculated for the fuel stream to travel as well as the distance it traveled, the average velocity of the fuel stream is determined. Using the distance traveled by

each stream in the image, a plot of the leading edge of the stream trajectory from the disk exit point is created.

Drag Model

Upon generating the position curve using the angle technique, a simple drag model was derived using a drag force calculation to provide a curve fit solution to the data points. This model determines the theoretical droplet position along the leading edge of the fuel trajectory, as well as the instantaneous velocity curve. As seen in equation 26, Newton's Second Law of Motion was used to relate force to the mass and velocity of the fuel droplets.

$$F = \frac{d}{dt}(m * v) \tag{26}$$

The drag force acting against the fuel droplets is represented using equation 27,

$$D = \frac{1}{2} * C_d * V^2 A * \rho_{air} \tag{27}$$

where the drag coefficient, C_d, is 0.424 for droplets in turbulent flow. Equation 28, shows the drag force equation substituted in as the force in Newton's Second Law and rearranged to be solved in terms of velocity.

$$\frac{dv}{dt} = \frac{\frac{1}{2} * C_d * A * V^2 * \rho_{air}}{m} \tag{28}$$

Equation 29 shows the integration of equation 28 to solve for instantaneous velocity with C representing each of the constants in the equations.

$$V = \frac{ds}{dt} = \frac{1}{C * t + V_o{}^{-1}} \tag{29}$$

$$C = \frac{C_d * A * \rho_{air}}{2 * m} \tag{30}$$

Equation 31 shows the integration of equation 29 to solve for position of the leading trajectory over time.

$$S(t) = \frac{\ln|C*t+V_o{}^{-1}|}{C} + S_o - \frac{\ln|V_o{}^{-1}|}{C} \tag{31}$$

For the analysis of the images, the initial position, S_o, is set to 0. Thus the equation for the position of the leading edge of the droplet stream over time reduces to

$$S(t) = \frac{\ln|C*t*V_o+1|}{C} \tag{32}$$

where V_0 is the initial velocity of the droplet as it exits the disk, and C remains the same as equation 30.

Curve Fit

In order to generate the fuel stream leading edge position curve for each fuel test, the MATLAB curve fitting toolbox was utilized. The fit function along with a custom fittype allowed for equation 32 to generate a best fit solution in the form of

$$\frac{1}{a} * \ln(a * b * x + 1) \tag{33}$$

where a represents the constant C, b represents the initial velocity V_o, and x represents time t.

As seen in equation 29, the derivative of this position curve fit provides a curve of the instantaneous velocity of fuel streams as a function of time. The instantaneous velocity curve was generated using the values for C and V_o taken from the position curve fit over a set range of time. The time used was $1.2 * 10^{-3}$ seconds, which was the average time evaluated for all fuel tests.

Tangential and Radial Velocities

As a supplemental analysis of the fuel stream velocity profile, this approach also focuses on creating velocity vectors in both the radial and tangential directions for each fuel stream. The tangential slope for each fuel stream is calculated by taking the derivative of the curve of the disk at the exit point of the fuel stream. The radial slope is then determined as the inverse of tangential slope. As seen in Figure 64, the tangential and radial velocity vectors are draw from the total velocity vector along their respective slopes until intersecting using MATLAB code. The angle, in degrees, between the total velocity vector and the radial velocity vector was calculated using Equation 34.

$$\theta = \tan\left(\frac{length\ of\ tangent\ vector}{length\ of\ radial\ vector}\right) * 180/\pi \tag{34}$$

The tangential and radial velocities are then calculated using Equations 35 and 36.

$$V_{tangent} = V * \sin(\theta) \tag{35}$$

$$V_{radial} = V * \cos(\theta) \tag{36}$$

Examples of the images used to provide input to the MATLAB code as well as the resulting images, plots and data can be found in Appendix H.

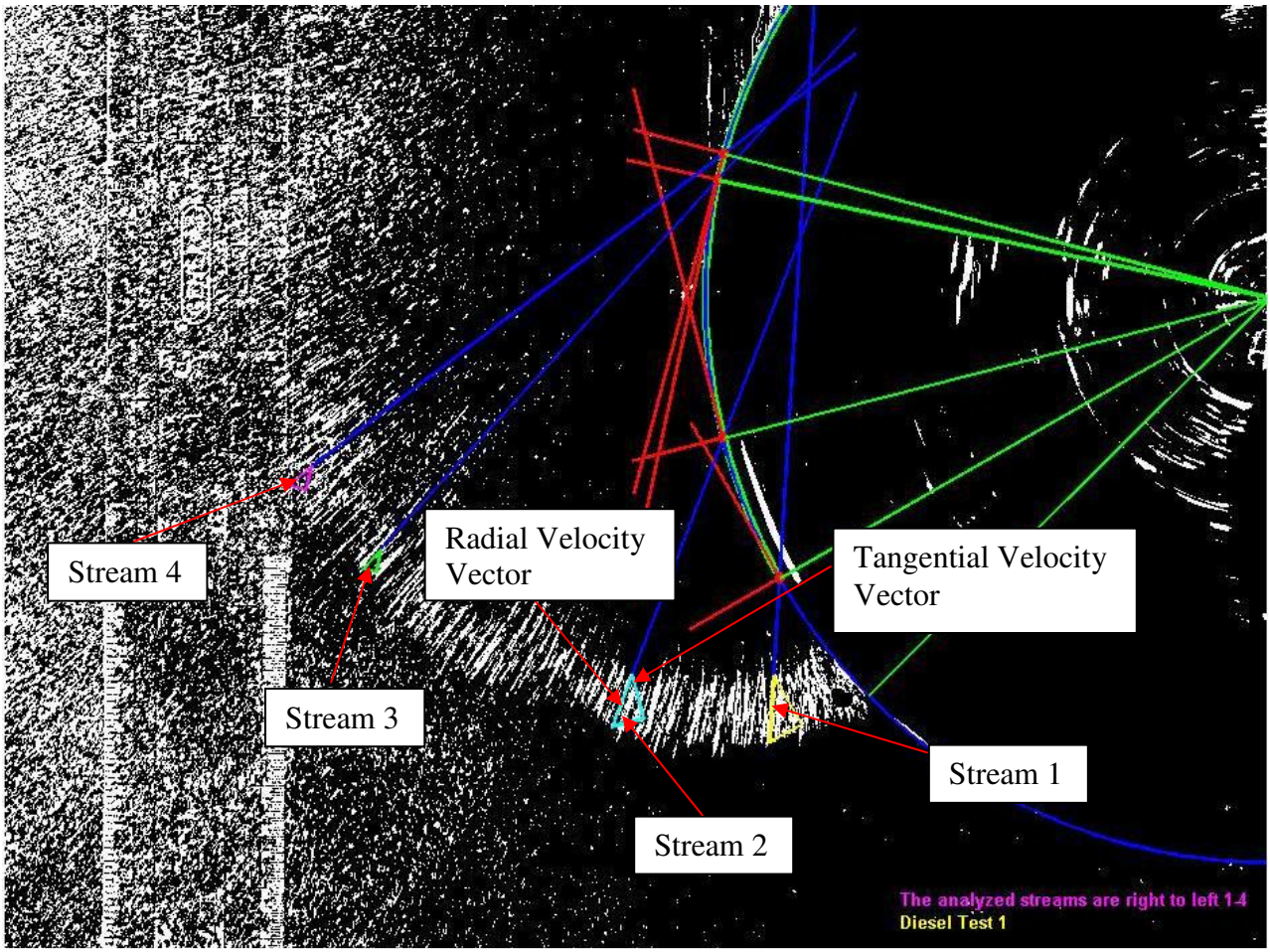

Figure 64. Resulting image from Velocity_calc_by_angle_diesel1 MATLAB code for diesel test 1 image.

Results and Conclusion

For the atomization tests, it is easy to qualitatively determine which fuels were able to atomize and which were not. These observations were confirmed with analysis of the fuel stream angle from the exiting point, drop diameters as well as droplet velocities. From the five tests run for each fuel, the top three quality tests were used for analysis.

Fuel Stream Angle

The fuel stream angle analysis focuses on the direction that the main fuel stream travels. This analysis was conducted for two distinct divisions: fuels that atomized and fuels that did not atomize. For the fuels that atomized, which include diesel, Jet-A, P184 and P186, results

averaged between 30 and 40 degrees. With the exception of Jet-A, each of the atomized fuels averaged within a few degrees of one another. Due to the sensitivity of the analysis, the results for Jet-A do not prove any significant difference between the atomization of the fuel and the other atomized fuels.

For the fuels that did not atomize, higher angles between the spray and the fuel exit point equate to higher levels of elasticity. This can be noticed with each of the thicker fuels, P117, P129 and P130. None of these fuels were able to atomize, and they instead produced either an elongated stream of fuel or a few ligaments. Results from P117, P129 and P130 averaged between 44 and 68 degrees. Each of these fuels are non-Newtonian, implying that they do not maintain a constant level of viscosity, thus their spray patterns also varied from test to test. Both P117 and P129, which were maintained the lowest angles from the exit location, formed ligaments within the time of the image capture. Sample fuel P130 maintained the highest spray angle from the exit location due to the fact that its fuel streams elongated along the edge of the disk during the time of the image capture.

Droplet Diameter and Velocity

The analysis of the droplet diameter and droplet velocity focuses both on the trajectory of the leading edge of the fuel stream as well as the level to which the fuel was able to atomize. For this analysis, the droplet diameter was measured at approximately 0.035m from the disk exit orifice. The droplets at the set distance from the disk exit were assumed to still be holding a spherical shape. Upon applying the spherical droplet shape to the droplet stream in each blurred image, the diameters were measured as the droplet width. An example image used to determine droplet diameter can be found in Figure 65.

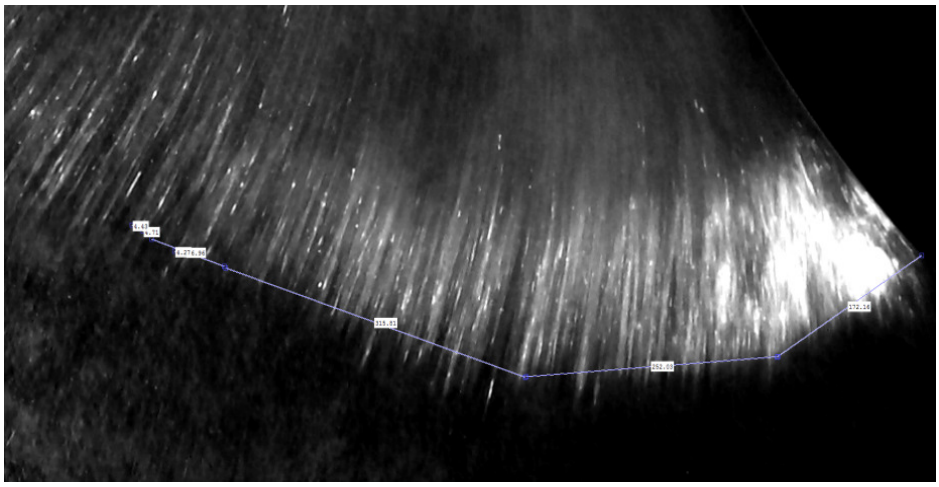

Figure 65. Image used to determine droplet diameter for Diesel test 1

This measurement has proved to be sensitive due to human error as well as the pixel to length ratio of the image. The percent error in measuring the diameter one pixel more or less than the previous measurement is 20%. This deviation, in comparison to other published droplet distribution curves is very acceptable. Within even a single point in a droplet mist, there exists a significant range of droplet sizes. Evidence of this can be seen in Figure 66, where for the lowest air flow curve there exists a difference of 140% between the mean diameter and the outmost boundary. In order to reduce some of the sensitivity, the droplet diameter results reflect an average of three droplet diameters measured around the 0.035m distance traveled for each test.

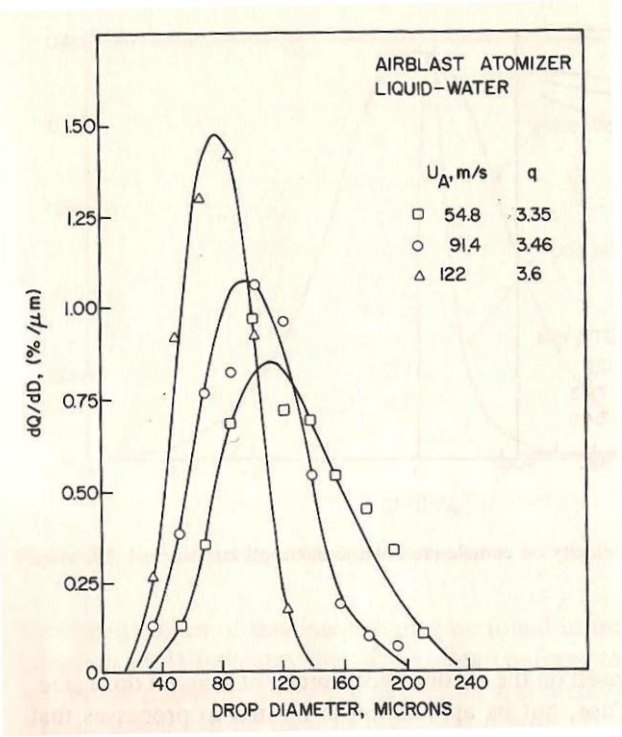

Figure 66. Example droplet frequency curves from Lefebvre [14] (under fair use, 2010).

A comparison of the droplet diameter results can be seen in Figure 67. These results show the average droplet diameters and standard deviations for three fuel tests conducted. The maximum deviation percentage between multiple runs of a single fuel can be found in the Diesel results at 17.4%. This result falls well within the distribution seen in Figure 66 and shows that the analysis method, although sensitive to human error, provides plausible results. The maximum droplet diameter difference of 33% is between Diesel and P184. Due to the level of variability in this analysis, it has been concluded that this result shows no significant difference in the particle break up of Diesel, Jet-A, P184 and P186.

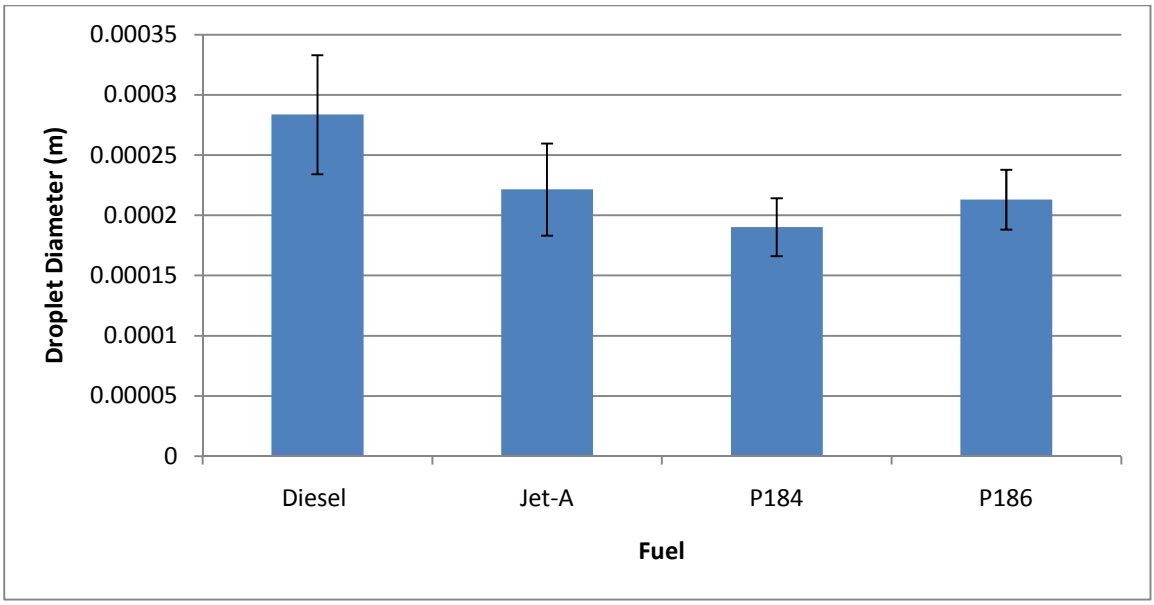

Figure 67. Droplet diameter comparison between fuels.

As seen in Figure 68, the fuel stream leading edge position over time proves to be fairly consistent between all of the fuels. Upon reaching 1.2 E-10 seconds from exiting the disk, each fuel droplet has traveled approximately 0.0625-0.067 meters, which yields a maximum variation of 7.2%. This value is deemed acceptable. These curves show that on average, when any of the fuel streams exit the disk, they will maintain a fairly consistent trajectory path as each of the other fuels.

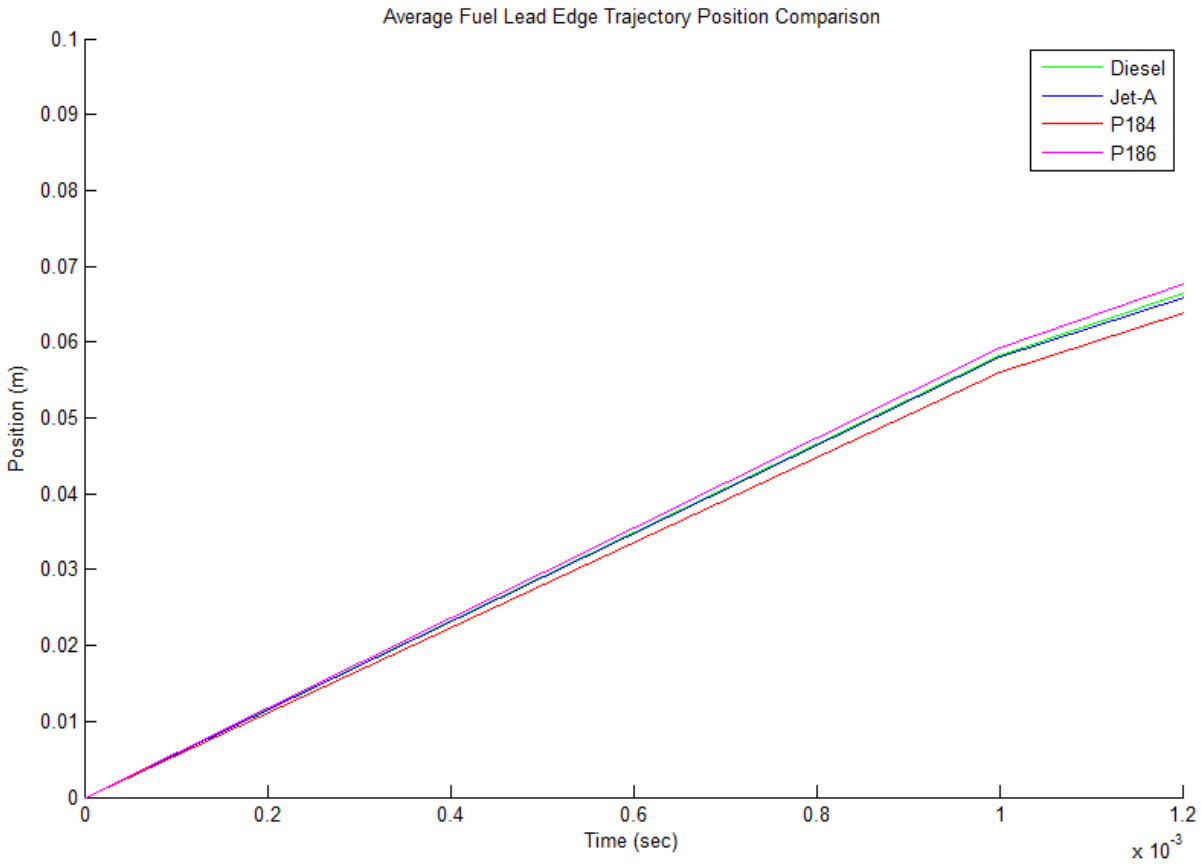

Figure 68. Curve fit for the position of the fuel leading edge trajectory.

The average instantaneous velocity curves for each fuel can be seen in Figure 69. These curves show little variation between the droplet velocity of each fuel over the course of time. A comparison between the initial velocities of each fuel can be seen in Appendix H. The percent deviation between each initial velocity proves to be a good measure of variability between fuels. The average initial velocity is 72 m/s with a percent deviation of 2.22%. These numbers are believed to be acceptable.

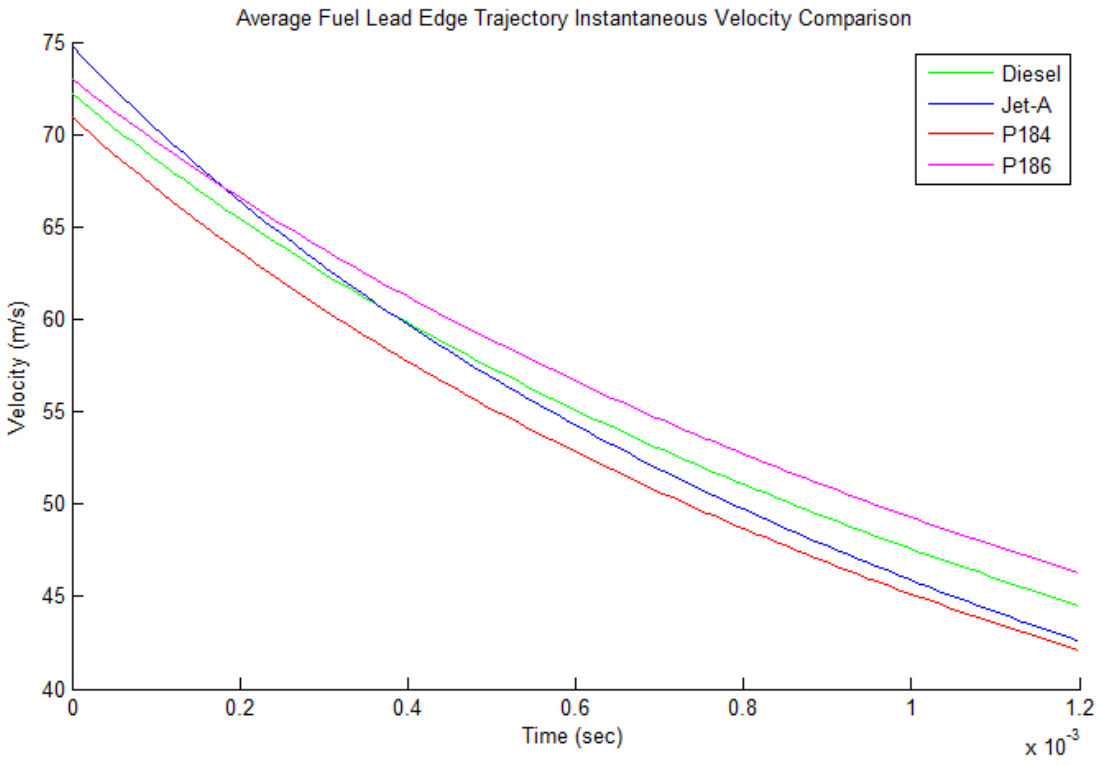

Figure 69. Instantaneous velocity of the fuel leading edge trajectory.

The results of the droplet diameter and instantaneous velocity analysis prove to be plausible. Though there are no similar comparative studies available to claim a specific degree of certainty upon these measurements, it is known that each of these fuels has a very similar density value to Diesel, and it has been seen qualitatively and quantitatively that the shear forces acting on the droplets in this experiment are not large enough to make a significant impact. Since each fuel's droplet diameter falls within the same magnitude, it is very plausible that the droplet stream trajectory and instantaneous velocity will result in similar trends and magnitudes. From these tests, it is concluded that Diesel, Jet-A, P184 and P186 demonstrate essentially the same atomization behavioral characteristics.

Fuel Propagation

During the ignition testing, each fuel was initially tested at 8500 rpm to correlate the results to the camera images. During that testing each fuel ignited except for P117, P129 and P130. In an effort to test the limits of these fuels, each of the three were tested again at 11,000 and 13,500

rpm. The resulting tests showed that no ignition occurred at either speed for any of the three fire resistant fuels. Visible ligaments exited the disk during testing of these fuels, and even though there were short burst of small flames across the torch, propagation did not take place. For the fuels that did burn, their propagation rates were analyzed in order to determine if the Luna fuels were more fire resistant than Diesel or Jet A. Propagation rates for the purpose of these tests are defined as the rate at which the lit fuels travel from the torch around the circumference of the disk. This definition can be seen in Figure 70, which shows a progression from left to right of Jet-A fuel initially igniting and then proceeding to propagate completely around the disk. This completed propagation can be seen in Figure 71.

Figure 70. Jet-A flame propagation progression.

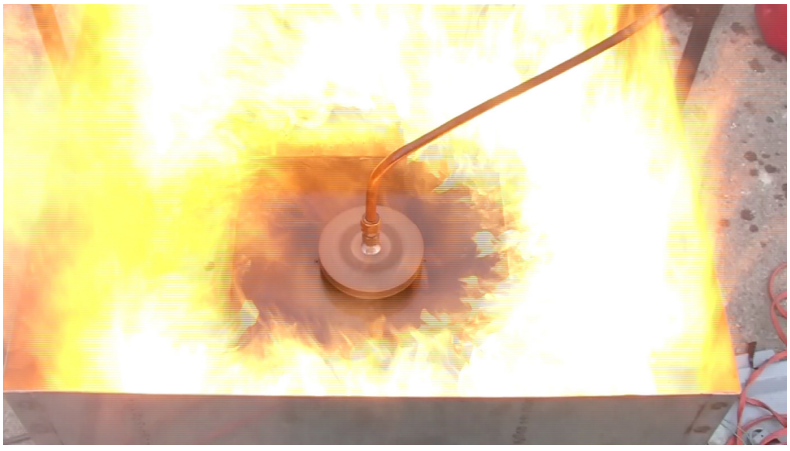

Figure 71. Jet-A rotary atomizer ignition test.

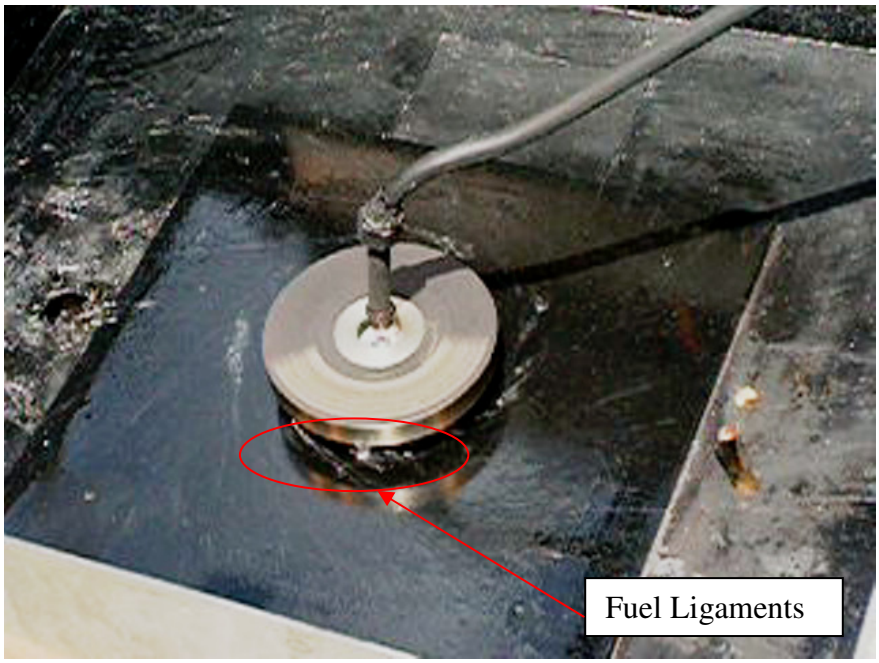

Figure 72. P117 rotary atomizer ignition test.

In terms of propagation rates, the Luna fuels were at the trailing edge of the curve. Jet A propagated the quickest at 110 inches per second with Diesel and P186 at 66 inches per second and P184 at roughly 47 inches per second. The results for both P186 and P184 show improvements in regards to Jet A, but do not warrant these fuels as being viable options as fire resistant fuels. For this testing, none of the emulsion FRF were able to propagate. This can be seen in Figure 72, where visible ligaments are formed, which correspond to visual results from the atomization characterization analysis. These ligaments spark when in contact with the propane flame but do not propagate.

Error Analysis

Error analysis was performed for droplet diameter calculations as well as droplet velocity. For error analysis of the droplet diameter, the standard deviation and percent difference were calculated as a measure of repeatability. The repeatability bounds for this analysis show the presence of noticeable error in the solutions. The magnitude of the results is deemed plausible. Several studies have been reviewed in which other researchers have utilized light scattering

technology to precisely determine droplet diameter at a range of rpm. As seen in Figure 73, at 8500rpm, the mean droplet diameter is approximately 1 E-4 m, which is within the same magnitude as the results obtained in this study.

As seen in Figure 74, 95% confidence intervals have been generated for lead edge trajectory position curves. These confidence intervals are not very wide, which reveals several things about the data points chosen in each fuel test. The first thing that should be noted about this test is there is human error involved in determine the coordinates for a droplet stream. Even though there is inherent error in the calculation from the involvement of the droplet diameter, the droplet diameter inaccuracies do not significantly affect the velocity measurements. This plot though reveals that the sensitivity of those points is not unreasonable. It should also be noted that the simple drag model provides a very accurate fit to these trends of data points.

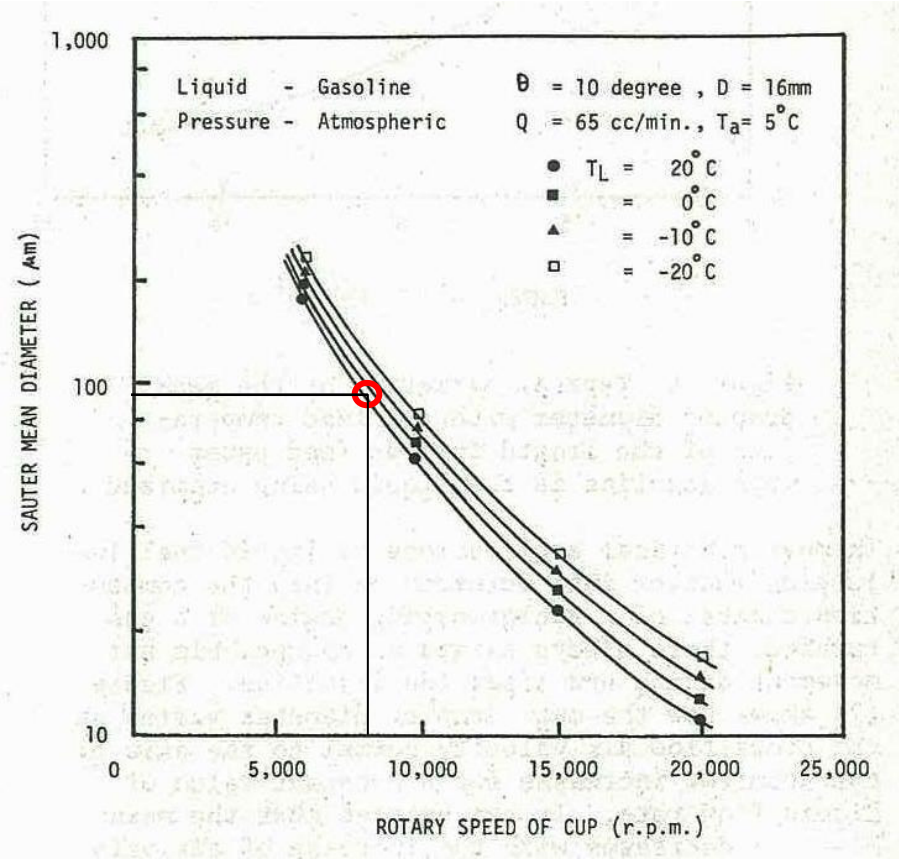

Figure 73. Typical variation in the mean droplet diameter with respect to the rotary speed of the cup from Karim and Kumar [15] (under fair use, 2010).

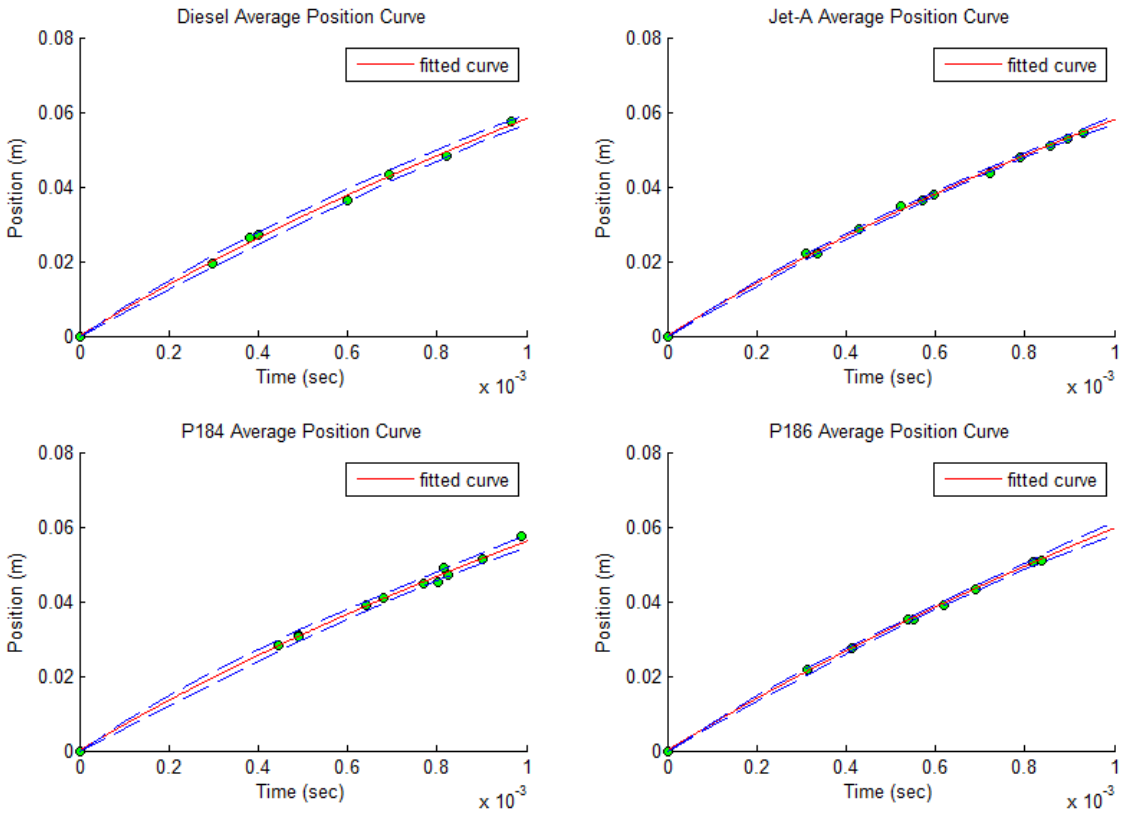

Figure 74. Curve fits for the position of the fuel's leading edge trajectory along with 95% confidence intervals and the original data points.

Recommendations

There are a few recommendations to be made for further testing of type or even with this testing setup. In terms of determining droplet size and velocity to characterize a fuel spray, static laser diffraction, Phase Doppler Particle Analyzers and PMS optical array probes would provide more accurate results. The use of any of these techniques would also allow for a more typical spray pattern to be analyzed through a nozzle setting. This would allow for easier replication of combat situations.

For the current rotary atomizer setup, the necessary key to better results and more options for analysis is a better camera for image taking and high speed video. Though the camera used can reach 1200 fps and has very nice features, it was never designed for this type of testing. Higher

speed and quality cameras will enhance the clarity of images and video allowing for greater detail. Use of a camera capable of taking an estimated 5 to 20 thousand frames per second could allow for more comprehensive observation of fuel behavior. Video recordings of the fuel spray would increase accuracy of droplet diameter and velocity calculations as well as allow for these calculations to be made over the course of time rather than at a specific instance.

Testing for spray characterization as well as fuel ignition should be conducted for each fuel at the steady state temperature reached in an engine. During field operations in the desert, the steady state temperature of the fuel in an operating diesel engine could potentially affect the performance of the fire resistant fuels in a negative way. These results need to be explored to determine the effect of preheating on spray characteristics as well as fuel ignition.

It would also be worthwhile to run these same types of tests with a fuel injector for an engine. Examining the spray characteristics of the engine fuel injector would allow a comparison to be made as to what it would take to light some of these fuels.

Lastly, it is recommended to setup a few specific high possibility scenarios during combat situations in which these fuels could be potentially harmful to the vehicle and its inhabitants. For these scenarios it is recommended to model the pressure as well as velocity of droplets exiting the tank. This will help to design tests with the atomizer to replicate those situations and experimentally validate those models.

Chapter 7 - Summary

In summary, the objectives for this comparative study were to experimentally evaluate the sample fire resistant fuels on two primary criteria: the ability for the fuel to replace Jet-A as a fuel in a compression ignition engine and the ability of the fuel to resist ignition when experiencing atmospheric temperature and pressure.

Preliminary bench-scale tests were performed to help narrow down the field of potential FRF candidates, as well as understand basic behavioral characteristics of certain types of FRF. These tests included the linear flame propagation testing as well as the swirl-flow combustion testing.

In order to address the first criteria, dynamometer testing was designed and performed to place a Yanmar 2V750 compression ignition engine under load. For each fuel, engine peak power outputs were determined at the maximum engine rpm level.

To address the second criteria of fire resistance, a rotary atomization testing apparatus was constructed in accordance with Naval Research Laboratory standards. Modifications were made to the system and testing of the fuels was completed in two stages; spray atomization characterization to determine fuel spray angle, droplet diameter and velocity, as well as fuel ignition characterization.

Lastly, cone calorimetry testing was performed to determine effective heats of combustion of selected fuels. This experiment provided supplemental information towards understanding results from the other tests.

Chapter 8 - Conclusions

Experimental results obtained from this comparative study provide quantitative evidence to support or deny the classification of Luna Innovation's sample fuels as potential fire resistant fuel candidates. The experimental setup and data reduction of the rotary atomizer has potentially provided a new means of determining droplet velocity as a function of time.

It is concluded that P129, P184 and P186 do not meet the requirements to be classified as fire resistant fuels. Within the engine test, P129 failed to achieve steady combustion within the engine. During the same testing, P184 and P186 were able to achieve steady combustion, but neither was able to achieve the same engine power as Diesel. Within the rotary atomization testing, P184 and P186 both atomized as well as Diesel and both ignited under the test conditions.

It is concluded from this research that both P117 as well as P130 meet the engine and fire resistance requirements to classify them as fire resistant fuel candidates. Both fuels met and exceeded the engine power output standard set by Diesel in the dynamometer test. Both fuels also failed to properly atomize, and thus also failed to ignite in the rotary atomization characterization testing.

In terms of the cone calorimeter testing, it is concluded that the energy content of each fuel was sufficient to operate the engine. It is also concluded that the energy content of each fuel did not play a significant role in the fuel's fire resistance ability. The fuels that did not ignite maintained the same levels of effective heat of combustion as both Diesel and Jet-A.

The results and conclusions from this testing provide a foundation for further research on the complex field of fire resistant fuels. Further testing of P117, P130 or any future generations will be needed in order to determine if they will prove successful in the field.

Chapter 9 - Future Research

This section will propose suggestions for future research of the fire resistant fuel candidates. In terms of the engine testing, it is recommended that more comprehensive dynamometer testing be conducted. This testing should focus on exploring the engine performance along the entire power curve and not just at the peak value. Also, it is recommended that engine endurance testing be performed with the fuels. It has been observed that the FRF candidates have the potential to negatively affect the engine's fuel injection system over time. It is proposed that long duration tests be run with the engine and that during the testing, dynamometer tests be used to monitor the engine power output. These endurance tests can be separated with a period of inactivity so that fuel has time to sit in the engine. This will help to monitor fuel capability in potential field scenarios before actually running a vehicle. Lastly, it is recommended that engine tests be conducted in various climates. These tests will explore the relationship between fuel startup temperature and the engine's ability to run. Upon completion of these tests, it is recommended that field testing be conducted.

In terms of the fire resistance testing, it is first recommended that a fundamental study be conducted in order to determine such fuel characteristics as auto ignition temperature and the activation energy required to ignite a set mass of fuel at standard atmospheric conditions. It is lastly recommended that combat situational ballistics testing be performed to explore fuel response to common field ignition sources.

References

1. ASTM Standard D5306 -92, 2002, *Standard Test Method for Linear Flame Propagation Rate of Lubricating Oils and Hydraulic Fluids*, ASTM International, West Conshohocken, PA, 2003, DOI**:** 10.1520/D5306-92R07 , www.astm.org.

2. ASTM Standard E 1354-04a, 2004, *Standard Test Method for Heat and Visible Smoke Release Rates for Materials and Products Using an Oxygen Consumption Calorimeter*, ASTM International, West Conshohocken, PA, 2003, DOI: 10.1520/E1354-04A , www.astm.org.

3. Thornton, W. (1991). "The relation of Oxygen to the Heat of Combustion of Organic Compounds." Philosophical Magazine and J. of Science, 33.

4. Huggett, C. (1980). "Estimation of the Rate of Heat Release by Means of Oxygen Consumption." J. of Fire and Flammability, 12, pp. 61-65.

5. Babrauskas, V. (1984). "Development of the Cone Calorimter--A Bench-scale Heat Release Rate Apparatus Based on Oxygen Consumption." Fire and Materials 8(2): 81-95.

6. Janssens, M. L. (1991). "Measuring Rate of Heat Release by Oxygen Consumption." Fire Technology 27(3): 234-249.

7. Babrauskas, V., Grayson, S.J. ed. (1992). "Heat Release in Fires." London, Elsevier Applied Science.

8. Rhodes, B. T., Quintiere, J. G. (1996). "Burning Rate and Flame Heat Flux for PMMA in a Cone Calorimeter." Fire Safety Journal 26: 221-240.

9. Ostman, B. A.-L., Svensson, I. G. (1985). *Comparison of Three Test Methods for Measuring Rate of Heat Release.* Fire and Materials 9(4): 176-183.

10. Babrauskas, V., Parker, W. J. (1987). “Ignitability Measurements with the Cone Calorimeter.” Fire and Materials 11: 31-43.

11. ASME. "Fluid Meters-Their Theory and Application," Report of the ASME Committee on Fluid Meters. H. Bean, editor, Sixth Edition. 1971.

12. Munson, B. R., Young, D. F., Okiishi, T. H. (2006). *Fundamentals of Fluid Mechanics*. New York: John Wiley & Sons.

13. ASTM RR: E05-1008, Report to ASTM on Cone Calorimeter Inter-Laboratory Trials, 1990.

14. Lefebvre, A. R. (1989). *Atomization and Sprays*. New York: Taylor and Francis.

15. Karim, G. A., Kumar, R. (1977). *The Atomization of Liquids at Low Ambient Temperature Conditions*.6th Australasian Hydraulics and Fluid Mechanics Conf., Dec. 5-9.

16. Hewitt, A. J. (1993). “Droplet Size Spectra Produced By Air-Assisted Atomizers.” Journal of Aerosol Science 24 (2): 155-162.

17. Willauer, H. D., Hoover, J. B., Williams, F. W., Mushrush, George W. (2005). "The Construction of an Improved Automated Atomizer for Evaluation Jet Fuel Flammability." Petroleum Science and Technology 23 (9 and 10): 1075-1082.

18. Semmlow, J. L. (2004). *Biosignal and Biomedical Image Processing MATLAB-Based Applications*. New York, Marcel Dekker.

19. Willauer, H. D., Hoover, J. B., Williams, F. W., Mushrush, G. W. (2004). *Chemical Methods For Decreasing Jet Fuel Flammability [PDF slides]*. Retrieved from Federal Aviation Administration Fire Safety website:

http://www.fire.tc.faa.gov/2004Conference/files/fuel/H.%20Willauer_Chemicals_for_decreasing_fuel_flammability.pdf

20. Schmitigal, J. A., Le Pera, M. E. (2009, October 2009). *Army Testing Fire Resistant Fuels for Combat Vehicles*. Retrieved 29 December, 2009, from http://www.nationaldefensemagazine.org/archive/2009/October/Pages/ArmyTestingFireResistantFuelsforCombatVehicles.aspx.

21. DiNenno, P. J., Drysdale, D., Beyler, C. L.,Walton, W. D., Custer, R. L. P., Hall, J. R. Jr., Watts, J. M. Jr., Ed. (2002). *SFPE Handbook of Fire Protection Engineering*. Quincy, National Fire Protection Association.

22. Marty, S. D., Schmitigal, J. (2009). *Fire Resistant Fuel*.

23. Lattimer, B. Y., Beitel, J. J. (1998). "Evaluation of Heat Release Rate Equations Used in Standard Test Methods." Fire and Materials 22: 167-173.

24. Turns, S. R. (2000). *An Introduction to Combustion Concepts and Applications*. 2nd ed. New York. McGraw-Hill.

25. Babrauskas, V., Twilley, W. H., Parker, W. J. (1993). “The Effects of Specimen Edge Conditions on Heat Release Rate.” Fire and Materials. 17:51-63.

26. Yanmar. Service Manual for Yanmar 2V750 Engine. pg. 4-3 – 13-15.

Appendix A: Swirl Flow Combustor Data Acquisition

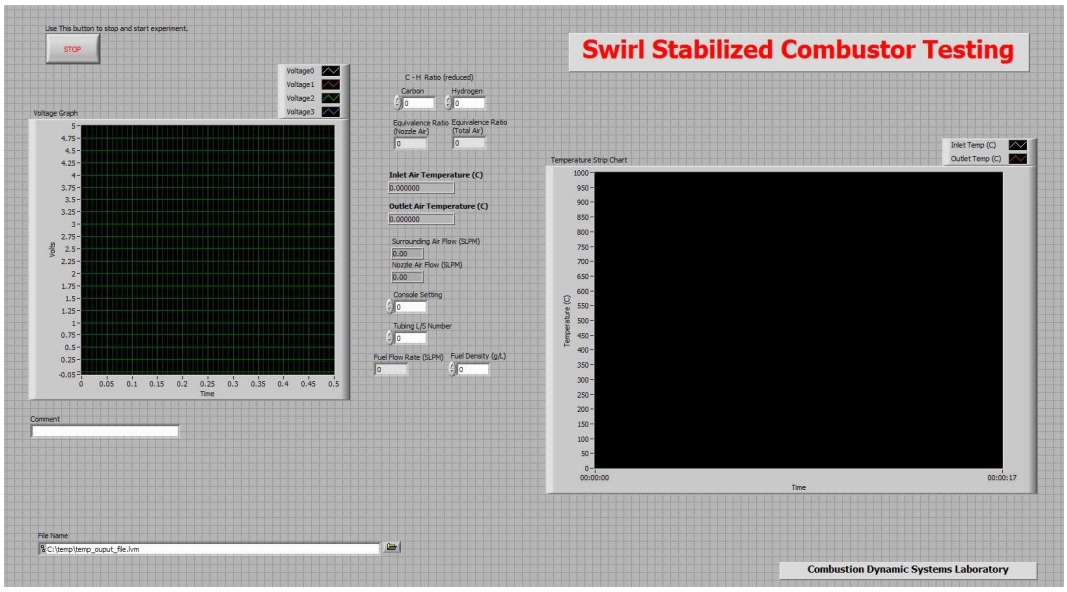

Figure 75. Front diagram for swirl flow combustor LabView VI.

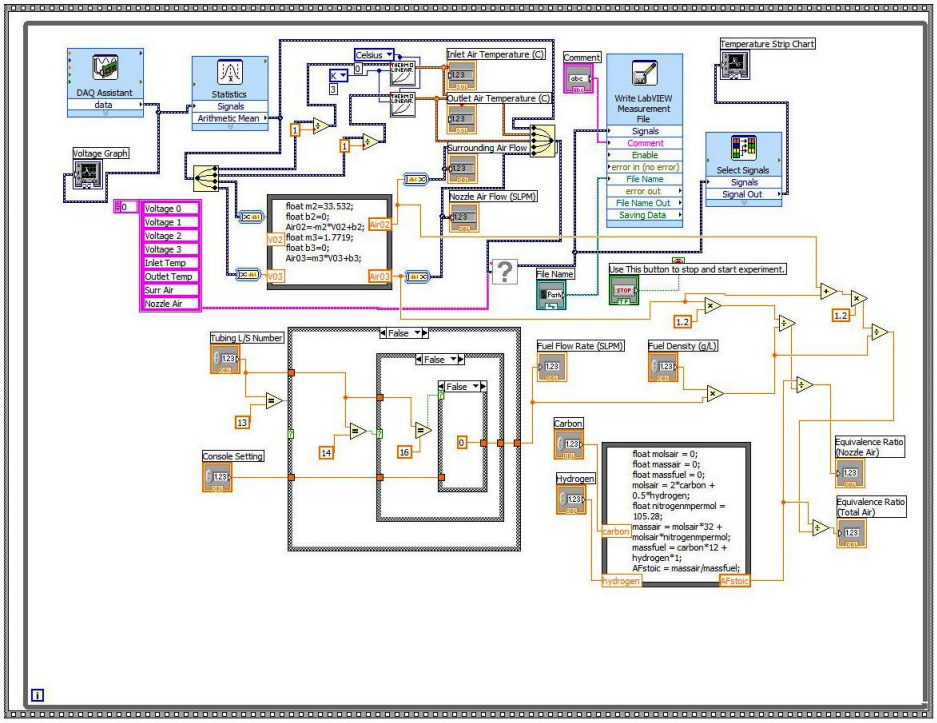

Figure 76. Block diagram for swirl flow combustor LabView VI.

Appendix B: Cone Calorimeter Test Results

Table 2. Diesel Calorimeter Heat of Combustion Results

Diesel	Bulk Heat of Combustion (KJ/kg)	Difference of Bulk from LHV	Date	Run #
1	41085.25	3.33%	23-May	1
2	40833.78	3.92%	23-May	2
3	40322.09	5.12%	23-May	3
average	**40747.04**			
st dev	388.90			
% Deviation between runs	**0.95%**			
ave lower heating value (lhv)	42500			

Table 3. Jet A Calorimeter Heat of Combustion Results

Jet-A	Bulk Heat of Combustion (KJ/kg)	Difference of Bulk from LHV	Date	Run #
1	44240.43	3.37%	23-May	1
2	43467.10	1.56%	23-May	2
3	42299.02	1.17%	23-May	3
average	**43335.52**			
st dev	977.37			
% Deviation between runs	**2.26%**			
ave lower heating value (lhv)	42800			

Table 4. P184 Calorimeter Heat of Combustion Results

P184	Bulk Heat of Combustion (KJ/kg)	Date	Run #
1	37209.40	23-May	1
2	39615.39	23-May	2
3	37282.78	23-May	3
average	**38035.86**		
st dev	1368.41		
% Deviation between runs	**3.60%**		

Table 5. P186 Test Comparison Chart

P186	Bulk Heat of Combustion (KJ/kg)	Date	Run #
1	44345.45	23-May	1
2	42306.49	23-May	2
3	42392.81	23-May	3
average	**43014.92**		
st dev	1153.09		
% Deviation between runs	**2.68%**		

Table 6. P117 Test Comparison Chart

P117	Bulk Heat of Combustion (KJ/kg)	Date	Run #		Date	Run #
outlier	36984.19	23-May	1			
	41726.75	23-May	2	41726.75	23-May	2
	41250.26	23-	3	41250.26	23-May	3

May

average	**39987.07**			**average**	**41488.51**
st dev	2611.46			st dev	336.93
% Deviation between runs	**6.53%**			**% Deviation between runs**	**0.81%**

Results without outlier

Table 7. Overall Calorimeter Effective Heat of Combustion Results

Fuel	Run #	Bulk Heat of Combustion (KJ/kg)	Repeatability Range	Averaged Repeatability Range
Diesel	1	41085.25	3.284	3.267
Diesel	2	40833.78	3.272	
Diesel	3	40322.09	3.246	
Jet A	1	44240.43	3.442	3.397
Jet A	2	43467.10	3.403	
Jet A	3	42299.02	3.345	
p184	1	37209.41	3.090	3.132
p184	2	39615.39	3.211	
p184	3	37282.78	3.094	
p186	1	44345.45	3.447	3.381
p186	2	42306.49	3.345	
p186	3	42392.81	3.350	
p117	1	36984.19	3.079	3.229
p117	2	41726.75	3.316	
p117	3	41250.26	3.293	

ASTM Standard for Repeatability:

$r = 1.23 + 0.05 * \Delta h_{c,eff}$

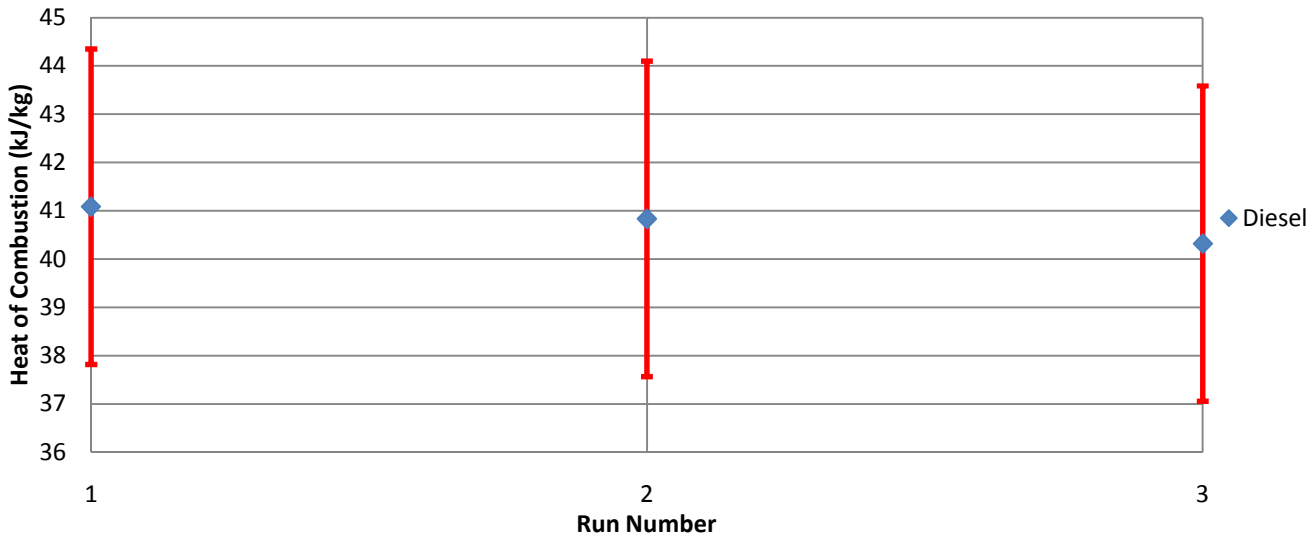

Figure 77. Heat of combustion results for Diesel. Error bars reflect the standard for repeatability set by the ASTM.

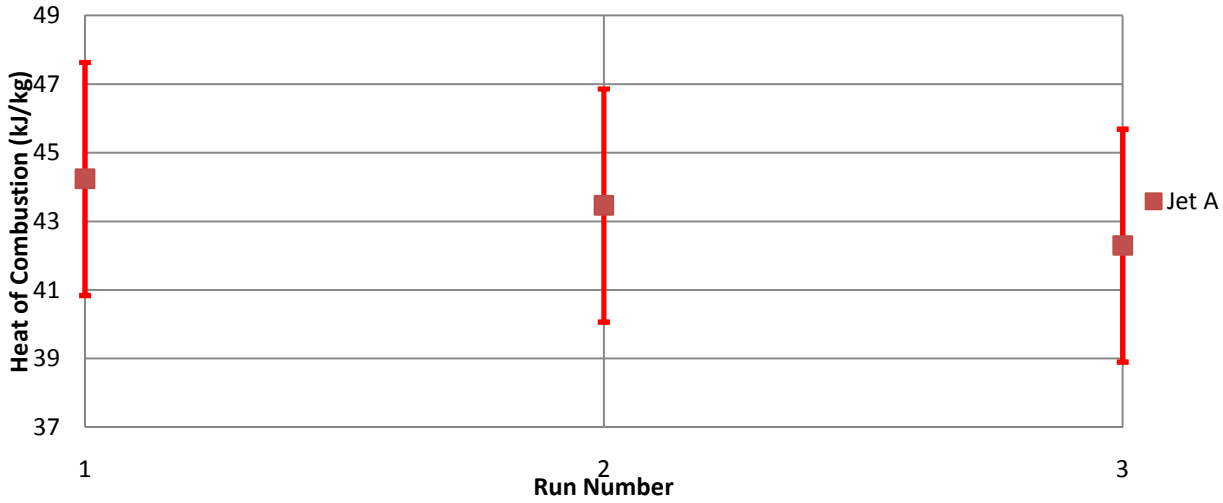

Figure 78. Heat of combustion results for Jet A. Error bars reflect the standard for repeatability set by the ASTM.

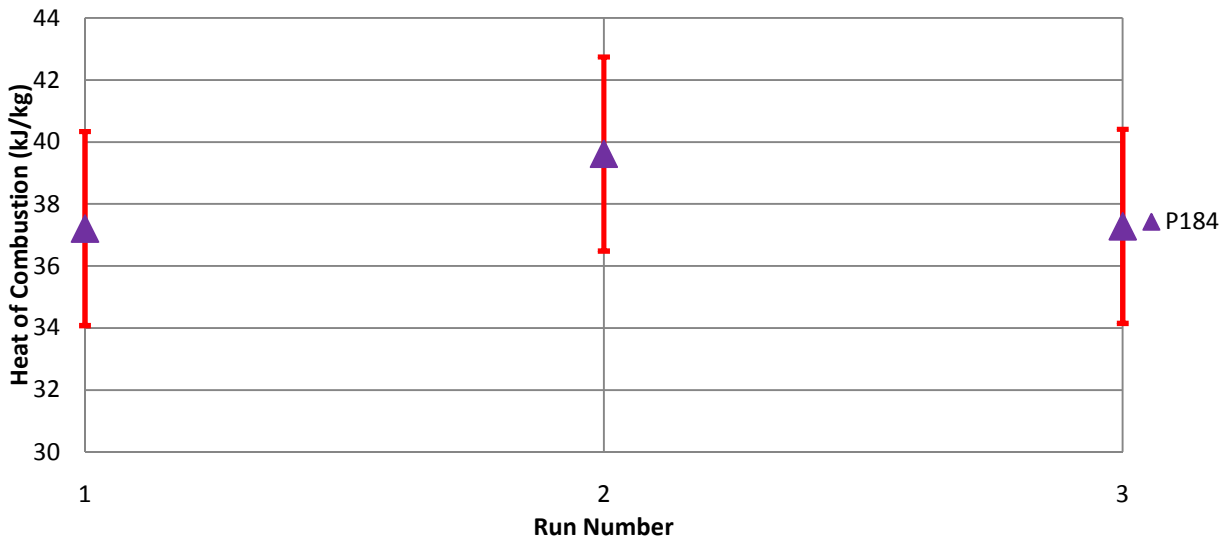

Figure 79. Heat of combustion results for P184. Error bars reflect the standard for repeatability set by the ASTM.

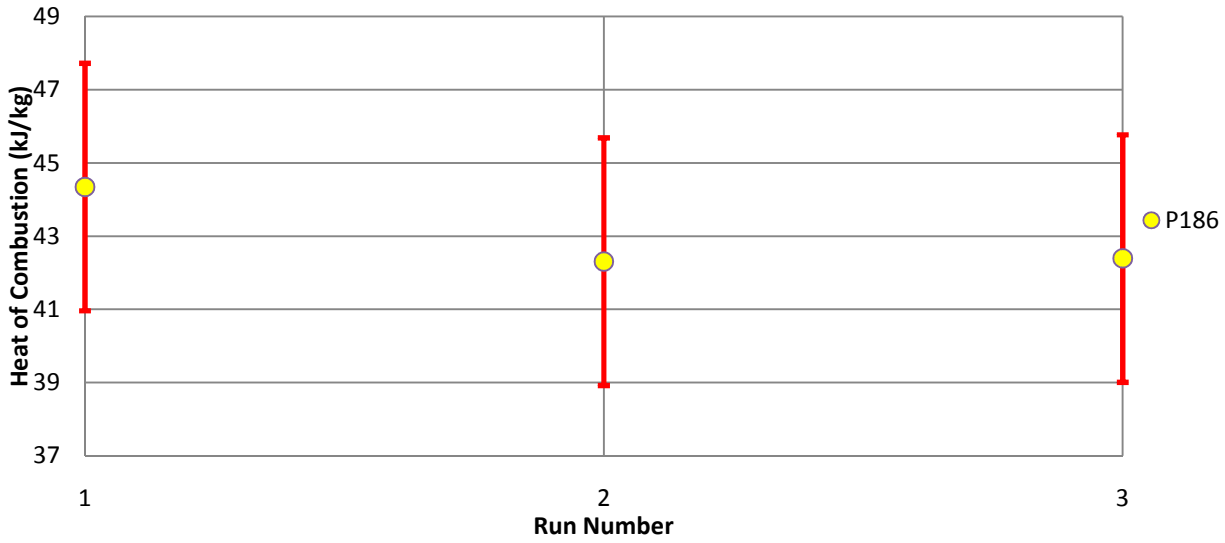

Figure 80. Heat of combustion results for P186. Error bars reflect the standard for repeatability set by the ASTM.

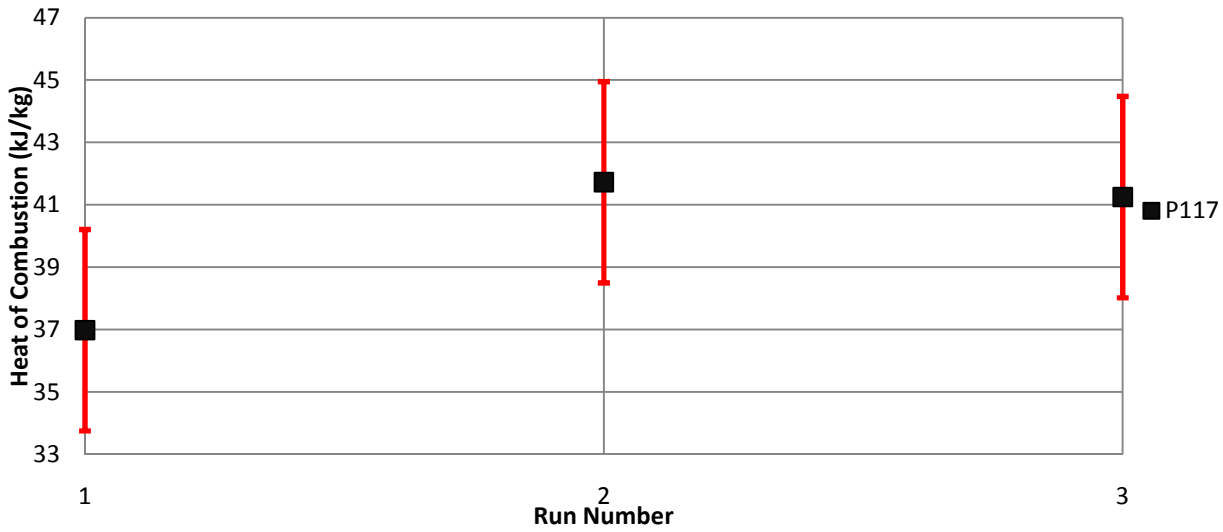

Figure 81. Heat of combustion results for P117. Error bars reflect the standard for repeatability set by the ASTM

Appendix C: Calorimeter Data Acquisition

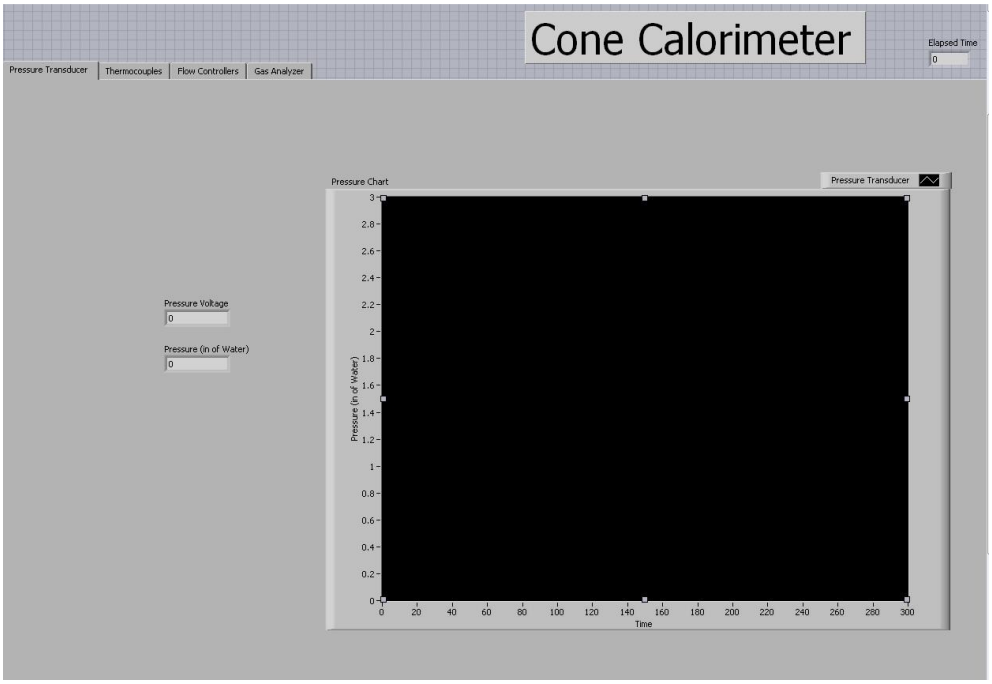

Figure 82. Front diagram for cone calorimeter LabView vi.

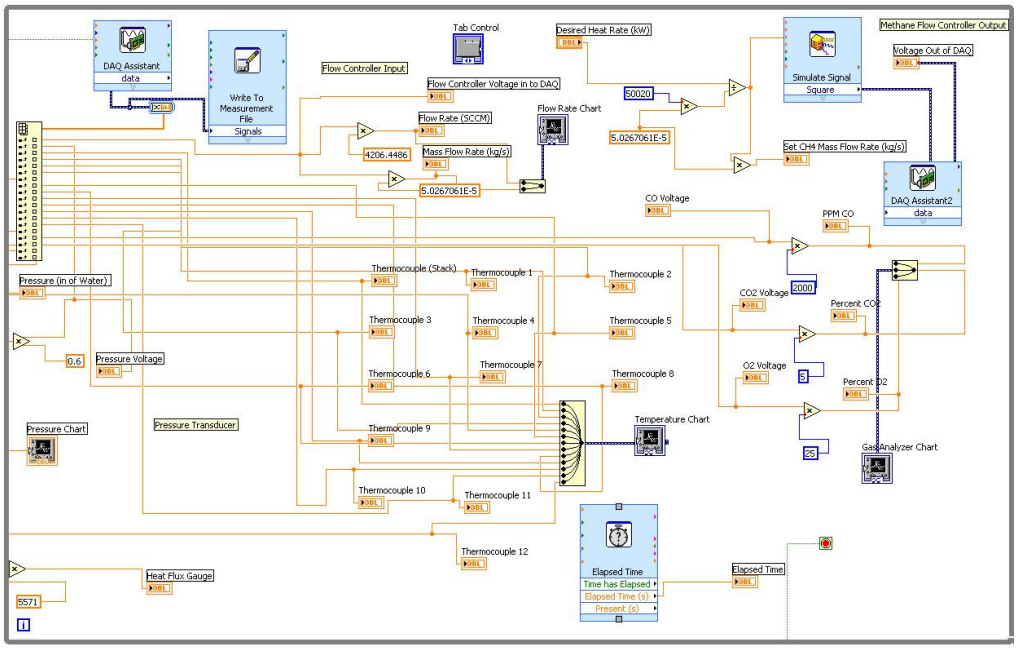

Figure 83. Block diagram for cone calorimeter LabView vi.

Appendix D: Engine Test Results

Table 8. Engine Test Comparison Chart

	Peak Values		Average Values		Deviation in Data			
Fuel	HP	RPM	HP	RPM	Std Dev	% Dev	Comments	Testing Order
Diesel	9.11	3155.80	9.08	3079.27	0.20	2.19%	baseline	1
JetA	5.00	3101.76	4.60	3082.19	0.43	9.31%		2
Diesel after JetA	8.78	3161.96	8.51	3138.23	0.37	4.34%		3
P184	7.12	3141.22	6.84	3117.32	0.25	3.60%	alcohol clean before test 7 in pulley	4
Diesel after P184	9.22	3220.75	7.03	0.37	0.18	1.97%	alcohol clean before test 7 in pulley	5
P186	6.32	3102.14	5.72	3038.66	0.40	7.05%	alcohol clean before test 7 in pulley	6
Diesel after P186	8.74	3145.01	8.43	3160.65	0.70	8.31%	alcohol clean before test 7 in pulley	7
P117	10.58	3045.71	9.89	3057.59	0.60	6.09%		8
Diesel after P117	5.11	3087.50	5.11	3087.50	0.00	0%		9
P129	7.19	3049.14	6.22	2897.15	0.94	15.19%	7 in pulley shakey, doesn't run smoothly, misses	10
Diesel after P129	7.51	3139.31	7.05	3090.69	0.45	6.37%	alcohol clean before test low pressure 7 in pulley	11
P130	8.92	3047.64	8.60	3016.38	0.32	3.68%	possibly did not see full power because ran after diesel with pressure 7 in pulley	12

Diesel after P130	5.43	2882.66	4.90	2575.32	0.75	15.29%	alcohol clean before test (last test) (needs fuel injection clean) low pressure 7 in pulley	13

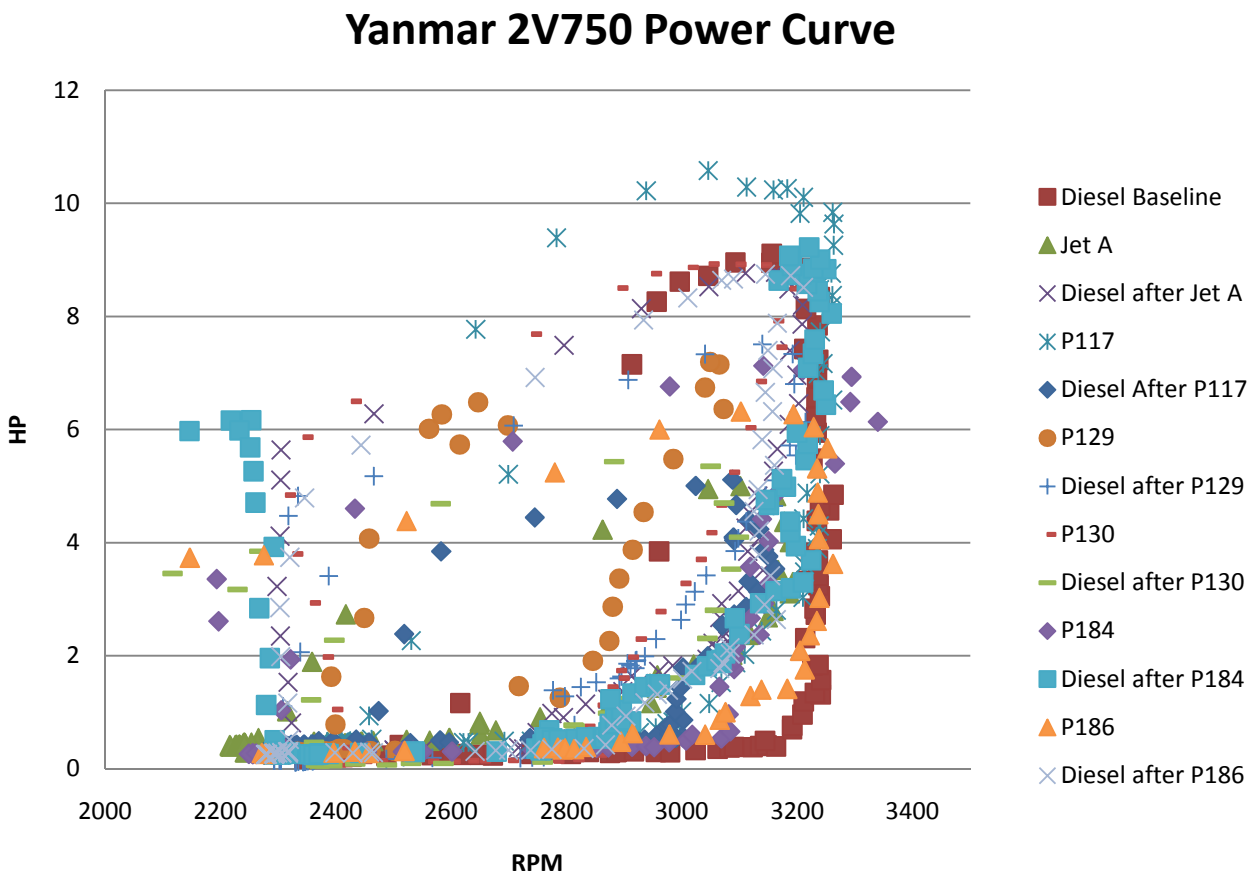

Figure 84. Power curve for Yanmar 2V750 engine tests for each fuel tested. Each curve shows the peak load curve for each fuel tested.

Appendix E: Engine Testing Computer Aided Design Parts

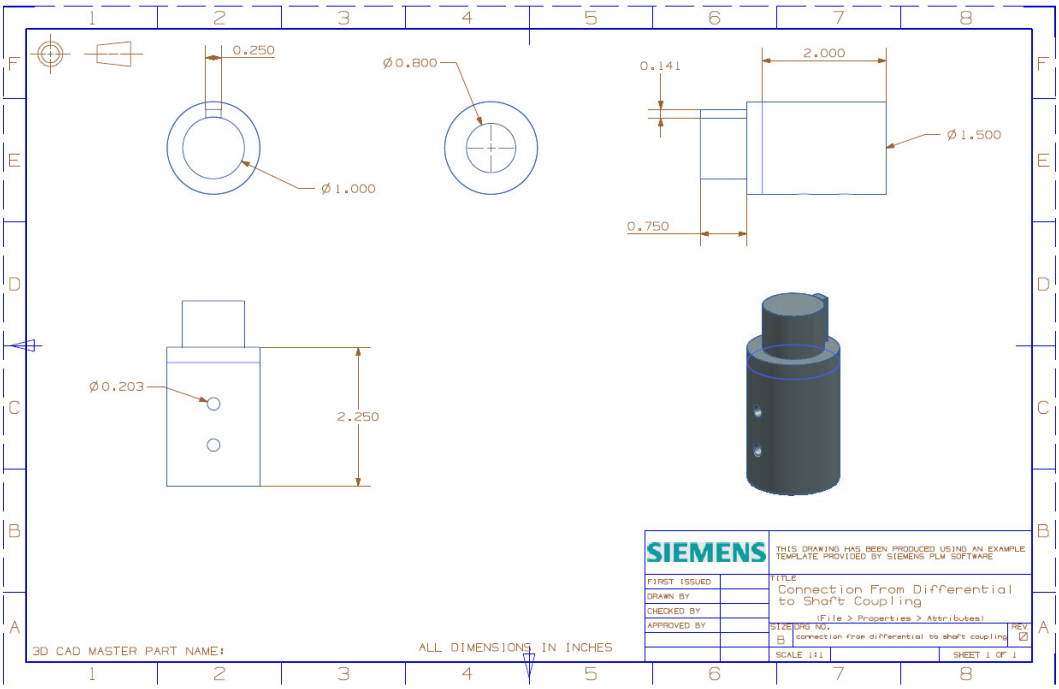

Figure 85. Connection piece between the motorcycle differential and the shaft coupling.

V-notches were cut into the differential shaft with an angle grinder to be used as seats for the bolts to hold the two pieces together. The top this piece had a standard key way and key to connect to the shaft coupling piece purchased from McMasterCarr.

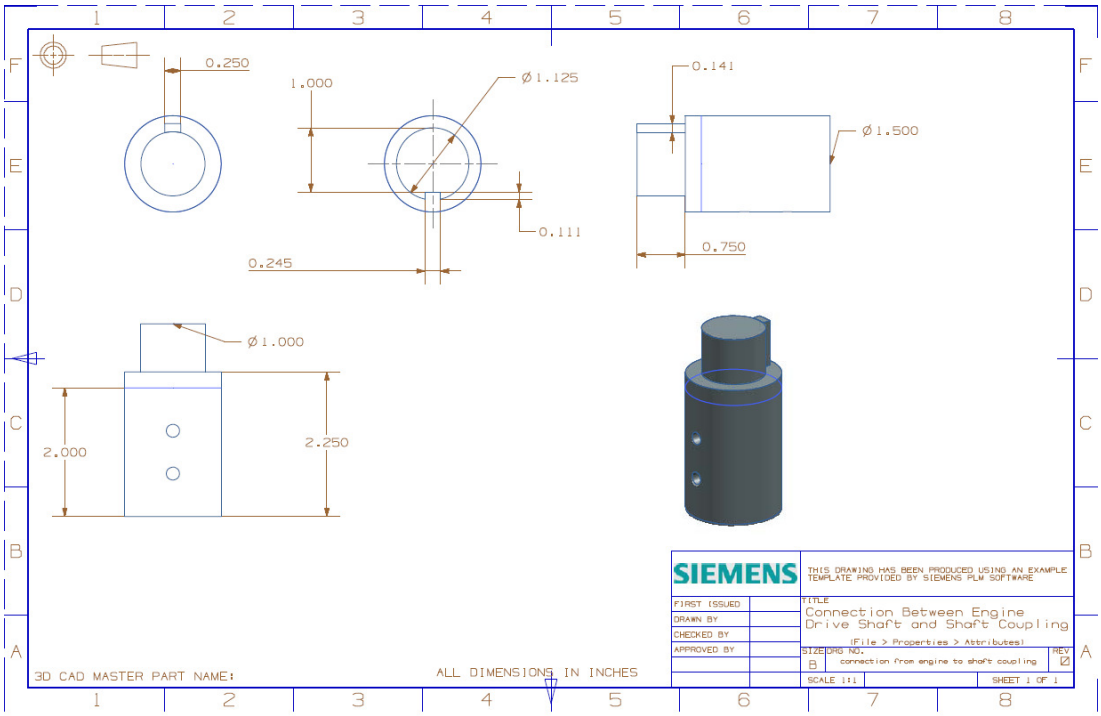

Figure 86. Connection piece between the Yanmar engine and the shaft coupling.

The through holes located vertically were tapped 1/4-20. The inside of this piece contains a standard key way and key to be interlocked with the keyed vertical engine driveshaft. The top this piece had a standard key way and key to connect to the shaft coupling piece purchased from McMasterCarr.

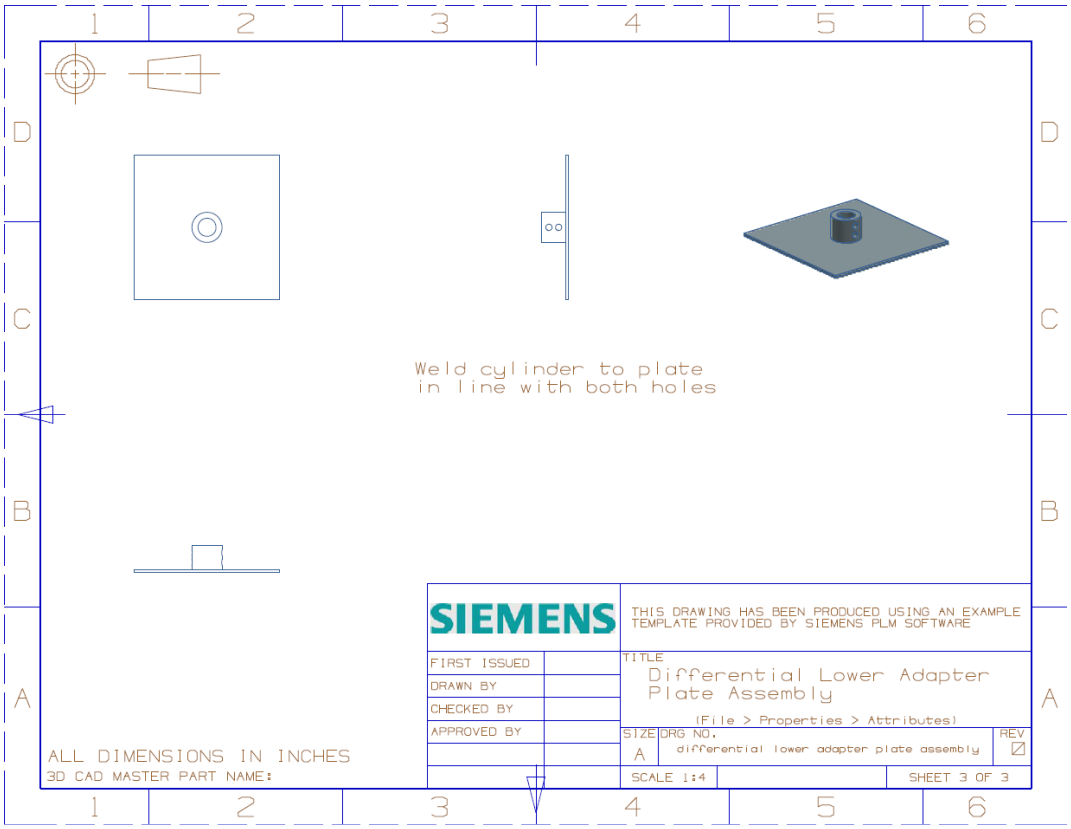

Figure 87. The lower adapter plate assembly for the horizontal differential drive shaft.

This piece is used to connect the differential to the horizontal drive shaft, which connects to the gear box. This piece also contains a circular pattern of mounting holes drilled into the quarter inch steel plate, which match with bolts located on the differential. The cylindrical piece protruding from the top of the plate is welded to the plate and used to hold the drive shaft. A matching hole to the top through hole on the cylindrical piece was drilled in the drive shaft and a bolt was pushed through both and used to restrain the shaft.

Appendix F: Engine Data Acquisition

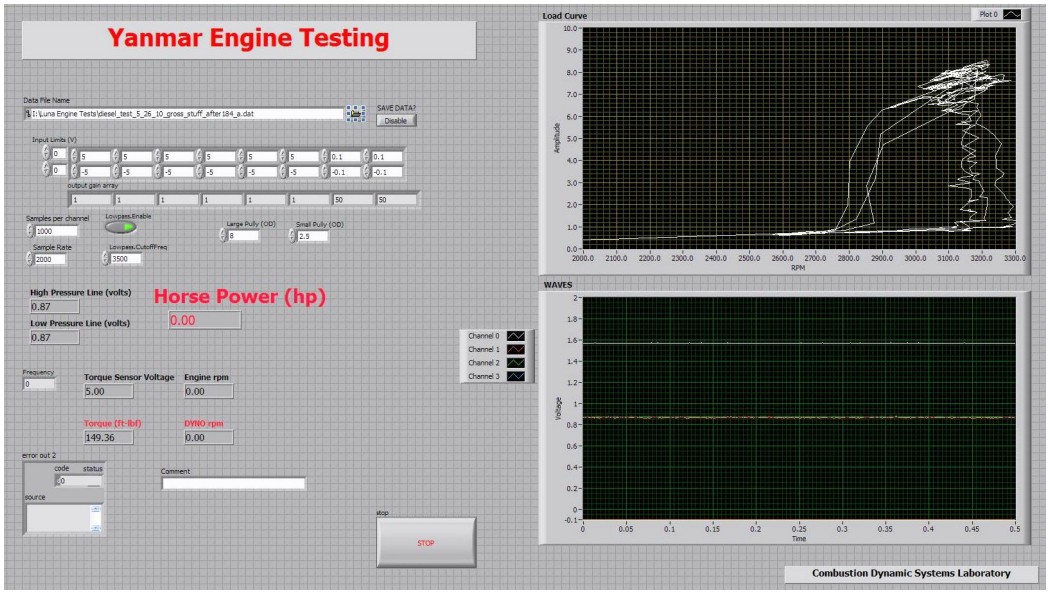

Figure 88. Front diagram for engine test LabView VI.

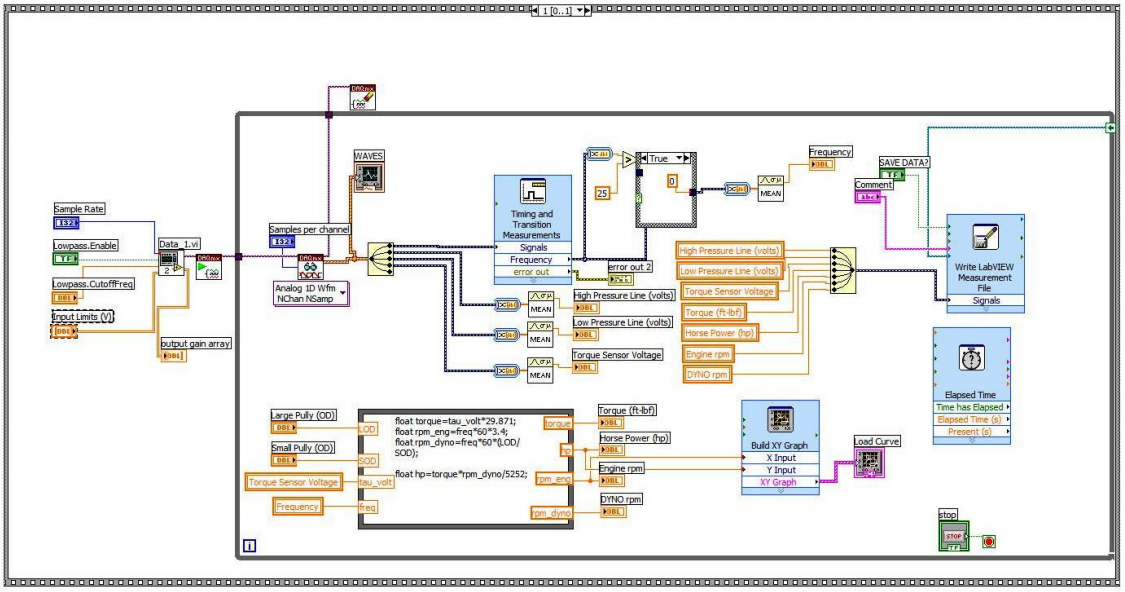

Figure 89. lock diagram for engine test LabView VI.

Appendix G: Rotary Atomizer Test Results

Table 9. Atomization Test Comparison Chart for Droplet Stream Body Angle

Fuel	Image #	Angle from exit (Degrees)	Average Angle	Standard Deviation	% Difference	Atomization, Ligamentation, Elongation	Average Condition of streams
Diesel	1	30.7				Atomization	
Diesel	2	39.6	34.57	4.56	13.20%	Atomization	Atomization
Diesel	3	33.4				Atomization	
Jet A	1	43.4				Atomization	
Jet A	2	40.95	39.42	4.93	12.51%	Atomization	Atomization
Jet A	3	33.9				Atomization	
P184	1	31.2				Atomization	
P184	2	28.5	30.43	1.69	5.54%	Atomization	Atomization
P184	3	31.6				Atomization	
P186	1	31.5				Atomization	
P186	2	29.5	29.93	1.40	4.68%	Atomization	Atomization
P186	3	28.8				Atomization	
P117	1	79.1				Elongation	
P117	2	56.8	68.27	11.16	16.35%	Ligamentation	Ligamentation
P117	3	68.9				Ligamentation	
P129	1	34.1				Ligamentation	
P129	2	59.9	44.20	13.78	31.18%	Ligamentation	Ligamentation
P129	3	38.6				Ligamentation	
P130	1	96.6				Elongation	
P130	2	93.4	98.83	6.83	6.91%	Elongation	Elongation
P130	3	106.5				Elongation	
Atomization		Qualifies as having more than 50 droplets per stream					
Ligamentation		Separation of the fuel but less than 50 droplets (i.e. ligaments)					
Elongation		No visible separation of the fuel stream					

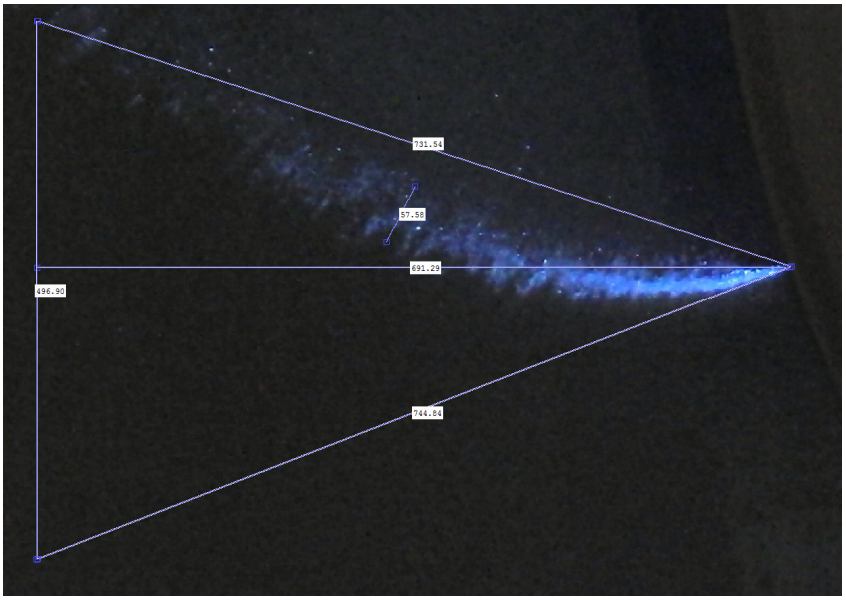

Figure 90. Jet A image processing to determine spray angle.

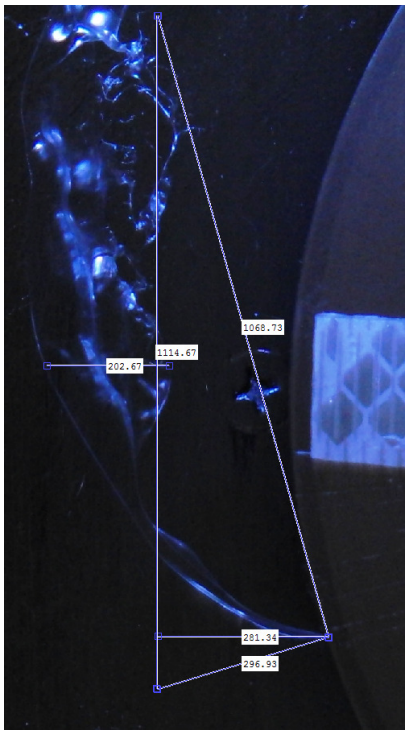

Figure 91. P130 image processing to determine spray angle.

Table 10. Droplet Diameter results for the fuels which were able to atomize. These results do not include P117, P129 and P130.

Fuel	Test #	Droplet Diameter (meters)	Average	St Dev	% Diff
Diesel	1	2.72E-04	2.84E-04	4.94E-05	17.40%
Diesel	2	3.38E-04			
Diesel	3	2.41E-04			
Jet A	1	2.32E-04	2.21E-04	3.83E-05	17.28%
Jet A	2	2.54E-04			
Jet A	3	1.79E-04			
P184	1	1.74E-04	1.90E-04	2.41E-05	12.66%
P184	2	2.18E-04			
P184	3	1.79E-04			
P186	1	2.03E-04	2.13E-04	2.48E-05	11.66%
P186	2	1.95E-04			
P186	3	2.41E-04			

Table 11. Droplet instantaneous velocity results for the fuels which were able to atomize.

Fuel	Initial Instantaneous Velocity (m/s)	Average	St Dev	% Diff
Diesel	72.20	72.70	1.614	2.22%
Jet A	74.77			
P184	70.91			
P186	72.93			

Table 12. Ignition Test Results

Fuel	Propagation Time (sec)	Circumference (inch)	Propagation Rate (inch/sec)	Propagation Rate (m/s)
Diesel	0.25	16.5	66	1.68
Jet A	0.15	16.5	110	2.79
P184	0.35	16.5	47.14	1.20
P186	0.25	16.5	66	1.68
P117	0	16.5	0	0
P129	0	16.5	0	0
P130	0	16.5	0	0

Flame Propagation Rate: time for flame to travel circumference of disk once lit

Appendix H: Rotary Atomizer Velocity Calculations

Image Blur Technique

Example Diesel Test 1

RPM = 8445

Disk Circumference: pi*5.25" = 16.5" = 1 revolution

Tape Circumference = pi*(5.25-2*31pixels/480pixels per inch) = 16.088"

Linear Velocity of end of tape: 135,863.16 inch/min = 2264.3 in/s

Reflective tape: 246 pixels = 0.5125"

Average blur across length of tape: 124 pixels = 0.2583"

Tape blur time delay: 0.2583inch / (2264.3inch/sec) = 1.14E-4 sec

(Averaged 3 droplets around set distance from disk)
Average droplet diameter at 800 pixels (1 and 2/3 inches) linearly from disk exit:

5.32pixels = 0.011 inches

Average Droplet blur: 0.285 inches (with diameter subtracted off)

Velocity of Droplet: 0.285inches / 1.14E-4 sec = 2401.46 inches/sec = **61 m/s**

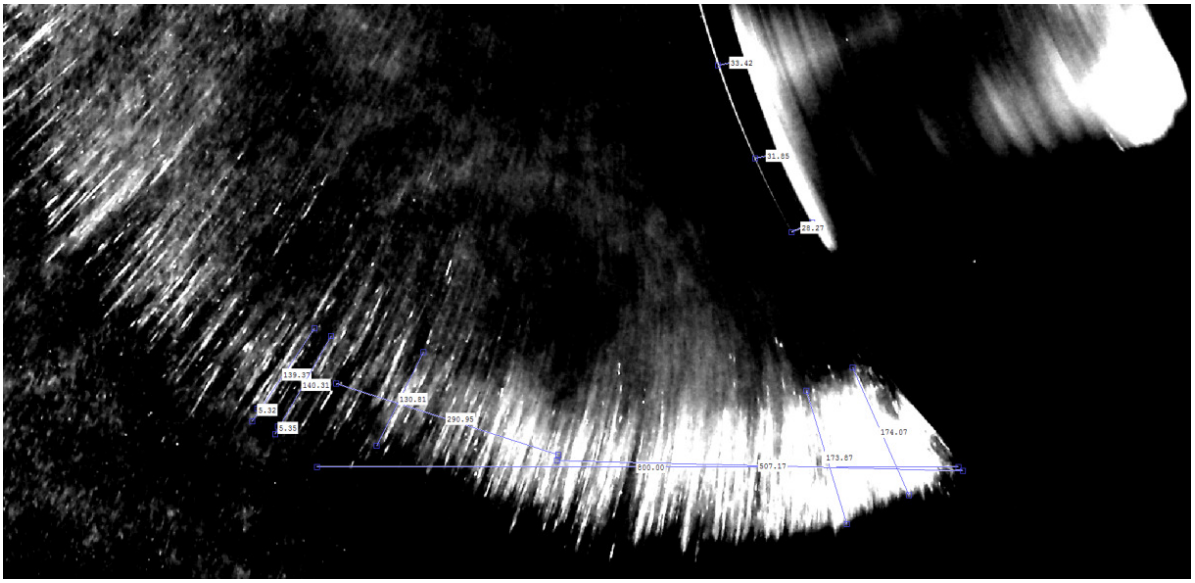

Figure 92. Diesel test 1 image used for velocity calculation. This image has been modified and analyzed using MATLAB's image processing toolbox.

Stream Angle Technique

Example Diesel Test 1

```
function [distplotd1,angles1] = Velocity_calc_by_angle_diesel1
%This program is used to analyze the angle that exists between each fuel
%stream and the disk exit point.  This program begins by importing a
%desired image and both enhancing the contrast of the image as well as a
%black and white image of the original photo with the natural background
%subtracted out.  Additional contrast can be achieved by using the
imtool
%feature that first appears after the program is initiated.

%The program prompts for inputs for both the disk exit location as well
as
%the location of both the top and bottom points of a fuel stream.  Upon
%entering the coordinates in the prompt window, Matlab generates and
image
%that connects the points as well as plotting the stream's radial and
%tangential velocity components.  Currently the program assumes that the
%tangential velocity of each fuel stream is the same as the disk at the
%disk exit point.  The program determines the angle between the
tangential
%velocity component and the overall velocity vector.  With the
assumption
%of a constant tangential velocity, the overall velocity and radial
%component are determined.  Currently the program is setup to analyze 4
%fuel streams.

%Steps to using program.
%1) Run program
%2) From either of the two images that are then displayed, choose
%coordinates (coordinates can be found by highlighting pixel with mouse
%and values are located in bottom left of imtool window)
%3) Enter values into the window prompt

clear all

%%
%Load Image from Directory
A = imread('steve_flash_diesel1.jpg');

B = rgb2gray(A);
%imtool(B)

c = imadjust(B);

%%
%Create Background approximation to subtract from image and enhance
%contrast
background = imopen(c,strel('disk',10,4));

c2 = c - background;

c3 = imadjust(c2);
```

```
x = graythresh(c3);

x1 = im2bw(c3,x);

W2 = bwareaopen(x1, 300);
imtool(W2)

%%
%Enter stream postion points and disk exit point
%{
angular_velocity = 8445;

xlocation = 1930;
ylocation = 1543;

stream1_xtop = 1717;
stream1_ytop = 1499;
stream1_xbot = 1708;
stream1_ybot = 1648;
dia1 = 2.2;

stream2_xtop = 1400;
stream2_ytop = 1497;
stream2_xbot = 1355;
stream2_ybot = 1614;
dia2 = 2.2;

stream3_xtop = 840;
stream3_ytop = 1216;
stream3_xbot = 799;
stream3_ybot = 1261;
dia3 = 2.2;

stream4_xtop = 685;
stream4_ytop = 1032;
stream4_xbot = 631;
stream4_ybot = 1073;
dia4 = 2.2;
%}
angular_velocity = input('Please Input the disk angular velocity  ');

xlocation = input('Please Input the disk exit point x coordinate  ');
ylocation = input('Please Input the disk exit point y coordinate  ');

stream1_xtop = input('Please Input the 1st fuel stream (right to left)
top x coordinate  ');
stream1_ytop = input('Please Input the 1st fuel stream (right to left)
top y coordinate  ');
stream1_xbot = input('Please Input the 1st fuel stream (right to left)
bottom x coordinate  ');
stream1_ybot = input('Please Input the 1st fuel stream (right to left)
bottom y coordinate  ');

stream2_xtop = input('Please Input the 2nd fuel stream (right to left)
top x coordinate  ');
```

```
stream2_ytop = input('Please Input the 2nd fuel stream (right to left)
top y coordinate  ');
stream2_xbot = input('Please Input the 2nd fuel stream (right to left)
bottom x coordinate  ');
stream2_ybot = input('Please Input the 2nd fuel stream (right to left)
bottom y coordinate  ');

stream3_xtop = input('Please Input the 3rd fuel stream (right to left)
top x coordinate  ');
stream3_ytop = input('Please Input the 3rd fuel stream (right to left)
top y coordinate  ');
stream3_xbot = input('Please Input the 3rd fuel stream (right to left)
bottom x coordinate  ');
stream3_ybot = input('Please Input the 3rd fuel stream (right to left)
bottom y coordinate  ');

stream4_xtop = input('Please Input the 4th fuel stream (right to left)
top x coordinate  ');
stream4_ytop = input('Please Input the 4th fuel stream (right to left)
top y coordinate  ');
stream4_xbot = input('Please Input the 4th fuel stream (right to left)
bottom x coordinate  ');
stream4_ybot = input('Please Input the 4th fuel stream (right to left)
bottom y coordinate  ');

%%
%Creating a contour plot around disk edge

dim = size(x1);

col = round(dim(2)/2)+335;

row = find(x1(:,col), 1);

connectivity = 8;
num_points = 1300;
contour = bwtraceboundary(x1, [row, col], 'N', connectivity,
num_points);

figure;
imshow(x1);
hold on;

plot(contour(:,2),contour(:,1),'g','LineWidth',4);
%%
%Completing the Circle outline of the Disk
x = contour(:,2);
y = contour(:,1);

% solve for parameters a, b, and c in the least-squares sense by
% using the backslash operator
abc = [x y ones(length(x),1)] \ -(x.^2+y.^2);
a = abc(1); b = abc(2); c = abc(3);

% calculate the location of the center and the radius
xc = -a/2;
```

```
yc = -b/2;
radius  =  sqrt((xc^2+yc^2)-c);

% display the calculated center
plot(xc,yc,'yx','LineWidth',2);

% plot the entire circle
theta = 0:0.01:2*pi;

% use parametric representation of the circle to obtain coordinates
% of points on the circle
Xfit = radius*cos(theta) + xc;
Yfit = radius*sin(theta) + yc;

A = zeros(length(Xfit),2);
A(:,1) = round(Xfit);
A(:,2) = round(Yfit);
%display(A)
plot(Xfit, Yfit,'LineWidth',2);

message = sprintf('Diesel Test 1');
text(2000,2050,message,'Color','y','FontWeight','bold');

message = sprintf('The analyzed streams are right to left 1-4');
text(2000,2000,message,'Color','m','FontWeight','bold');



%%
%Fuel Stream Lines: tangential and radial gradients as well as overall

%Fuel Stream 1

%creates a line from the fuel stream back to exit point on disk
tvs1 = (stream1_ytop - stream1_ybot)/(stream1_xtop - stream1_xbot);
%total velocity slope

bstream1 = stream1_ytop - tvs1*stream1_xtop;  %intercept

%Creates a line from the top of the fuel stream to x = 1900 (xstream1 =
%stream1_xtop)
xstream1 = stream1_xtop:1:1900;
ystream1 = zeros(1,length(xstream1));
for n = 1:length(xstream1)

    ystream1(n) = tvs1*xstream1(n) + bstream1;

end
B1 = zeros(length(xstream1),2);
B1(:,1) = round(xstream1);
B1(:,2) = round(ystream1);

%plots line
plot(xstream1,ystream1,'LineWidth',2)

X1 = zeros(2,1);
```

```
%calculates the intersection point between line and circle
%analytical solution results in two quadratic equations which solves for
x
%values
z1 = bstream1 - yc;
aX1 = tvs1^2 + 1;
bX1 = 2*(tvs1*z1 - xc);
constX1 = xc^2 +z1^2 - radius^2;

X1(1) = (-bX1 + sqrt(bX1^2 - 4*constX1*aX1))/(2*aX1);
X1(2) = (-bX1 - sqrt(bX1^2 - 4*constX1*aX1))/(2*aX1);

%calculates the y coordinate for the minium x coordinate (quadratic
forms
%two solutions at both intersections along the circle
Y1 = tvs1*min(X1) + bstream1;
intersection1 = [min(X1),Y1];

%plots intersection point
plot(min(X1),Y1,'rx','Linewidth',4)

xline_angletop1 = [xc, intersection1(1)];
yline_angletop1 = [yc, intersection1(2)];

%creates line from intersection point to center of disk
line(xline_angletop1,yline_angletop1,'Color','g','LineWidth',2);

xline_anglebot = [xc, xlocation];
yline_anglebot = [yc, ylocation];

%creates line from exit hole to center of disk
line(xline_anglebot,yline_anglebot,'Color','g','LineWidth',2);

%calculates angle between intersection point and exit hole location
%vector(A)*vector(B)*cos(theta) = lAl*lBl
vect11 = [(xlocation-xc) (ylocation-yc)];
vect21 = [(intersection1(1)-xc) (intersection1(2)-yc)];
dp = dot(vect11, vect21)/norm(vect11)/norm(vect21);
angle1 = acos(dp)*180/pi;

%distance disk has traveled over angle/rotational speed/time disk has
%traveled in picture
circumdist1 = angle1/360*(2*pi*radius); %circumference in pixels
linear_rot_velocity = angular_velocity*2*pi*radius/60;  %linear velocity
in pixels
time1 = circumdist1/linear_rot_velocity;

%distance fuel has traveled in picture (intersection point to bottom of
%fuel stream
stream1_dist = sqrt(abs(intersection1(1) - stream1_xbot)^2 +
abs(intersection1(2) - stream1_ybot)^2) - dia1; %stream linear distance
in pixels

%total velocity
vel1 = (stream1_dist/480*.0254)/time1;
```

```
%Tangent and Radial slopes for fuel stream 1
tangent_slope1 = -(intersection1(1)-xc)/(intersection1(2)-yc);
xintersectfinal1 = intersection1(1) - 200;

xcoord1 = xintersectfinal1:intersection1(1);
yint1 = (intersection1(2)-tangent_slope1*intersection1(1));

tangent_line1 = tangent_slope1*xcoord1+yint1;
plot(xcoord1,tangent_line1,'r','LineWidth',2);

perpendicular_slope1 = -1/tangent_slope1;
yintp1 = (intersection1(2)-perpendicular_slope1*intersection1(1));
perpendicular_line1 = perpendicular_slope1*xcoord1+yintp1;

plot(xcoord1,perpendicular_line1,'r','LineWidth',2);

%Draws the Radial and Tangential velocity vectors connected to total
%velocity vector
xline = [stream1_xtop, stream1_xbot];
yline = [stream1_ytop, stream1_ybot];
line(xline,yline,'Color','y','LineWidth',2);

tanline_intercept = stream1_ytop - tangent_slope1*stream1_xtop;
perpline_intercept = stream1_ybot - perpendicular_slope1*stream1_xbot;

xintersect_point = -(perpline_intercept - tanline_intercept)/(-
tangent_slope1 + 1/-tangent_slope1);
yintersect_point = tangent_slope1*xintersect_point + tanline_intercept;

xline_tan = [stream1_xtop, xintersect_point];
yline_tan = [stream1_ytop, yintersect_point];
xline_perp = [stream1_xbot, xintersect_point];
yline_perp = [stream1_ybot, yintersect_point];
line(xline_tan,yline_tan,'Color','y','LineWidth',2);
line(xline_perp,yline_perp,'Color','y','LineWidth',2);

fs1 = sqrt((stream1_xtop-stream1_xbot)^2 + (stream1_ytop-
stream1_ybot)^2);
fs1_perp = sqrt((stream1_xtop-xintersect_point)^2 + (stream1_ytop-
yintersect_point)^2);
fs1_tan = sqrt((stream1_xbot-xintersect_point)^2 + (stream1_ybot-
yintersect_point)^2);

anglet1 = atan(fs1_perp/fs1_tan)*180/pi;  %Stream angle in degrees
anglet1rad = atan(fs1_perp/fs1_tan); %Stream angle in radians

%tangential and radial velocities
vel1tan = sin(anglet1rad)*vel1;
vel1rad = cos(anglet1rad)*vel1;

%print results
fprintf('Intersection point on disk (stream exit point)
%6.2f \n',intersection1);
fprintf('Angle between fuel stream exit and end exit hole position
%6.2f \n',angle1);
```

```
fprintf('Rotational distance of disk over time fuel stream 1 has
traveled (m) %6.2f \n',circumdist1/480*.0254);
fprintf('Fuel stream 1 travel time (s)
%2.8f \n',time1);
fprintf('Fuel Stream 1 Tangential Angle of fuel stream is (deg)
%6.2f \n\n',anglet1);
fprintf('Fuel Stream 1 Tangential Velocity is (m/s)
%6.2f \n',vel1tan);
fprintf('Fuel Stream 1 Radial Velcoity is (m/s)
%6.2f \n',vel1rad);
fprintf('Fuel Stream 1 Total Velocity is (m/s)
%6.2f \n\n\n',vel1);
%%
%Fuel Stream 2

%creates a line from the fuel stream back to exit point on disk
tvs2 = (stream2_ytop - stream2_ybot)/(stream2_xtop - stream2_xbot);
%total velocity slope

bstream2 = stream2_ytop - tvs2*stream2_xtop;  %intercept

%Creates a line from the top of the fuel stream to x = 1900 (xstream1 =
%stream1_xtop)
xstream2 = stream2_xtop:1:1900;
ystream2 = zeros(1,length(xstream2));
for n2 = 1:length(xstream2)
    ystream2(n2) = tvs2*xstream2(n2) + bstream2;
end

plot(xstream2,ystream2,'LineWidth',2)

X2 = zeros(2,1);

%calculates the intersection point between line and circle
%analytical solution results in two quadratic equations which solves for
x
%values
z2 = bstream2 - yc;
aX2 = tvs2^2 + 1;
bX2 = 2*(tvs2*z2 - xc);
constX2 = xc^2 +z2^2 - radius^2;

X2(1) = (-bX2 + sqrt(bX2^2 - 4*constX2*aX2))/(2*aX2);
X2(2) = (-bX2 - sqrt(bX2^2 - 4*constX2*aX2))/(2*aX2);

%calculates the y coordinate for the minium x coordinate (quadratic
forms
%two solutions at both intersections along the circle
Y2 = tvs2*min(X2) + bstream2;
intersection2 = [min(X2),Y2];

plot(min(X2),Y2,'rx','Linewidth',4)

xline_angletop2 = [xc, intersection2(1)];
yline_angletop2 = [yc, intersection2(2)];
```

```
%creates line from intersection point to center of disk
line(xline_angletop2,yline_angletop2,'Color','g','LineWidth',2);

%calculates angle between intersection point and exit hole location
%vector(A)*vector(B)*cos(theta) = lAl*lBl
vect12 = [(xlocation-xc) (ylocation-yc)];
vect22 = [(intersection2(1)-xc) (intersection2(2)-yc)];
dp2 = dot(vect12, vect22)/norm(vect12)/norm(vect22);
angle2 = acos(dp2)*180/pi;

%distance disk has traveled over angle/rotational speed/time disk has
%traveled in picture
circumdist2 = angle2/360*(2*pi*radius); %circumference in pixels
time2 = circumdist2/linear_rot_velocity;

%distance fuel has traveled in picture (intersection point to bottom of
%fuel stream
stream2_dist = sqrt(abs(intersection2(1) - stream2_xbot)^2 +
abs(intersection2(2) - stream2_ybot)^2) - dia2; %stream linear distance
in pixels

%total velocity
vel2 = (stream2_dist/480*.0254)/time2;

%Tangent and Radial slopes for fuel stream 2
tangent_slope2 = -(intersection2(1)-xc)/(intersection2(2)-yc);
xintersectfinal2 = intersection2(1) - 200;

xcoord2 = xintersectfinal2:intersection2(1);
yint2 = (intersection2(2)-tangent_slope2*intersection2(1));

tangent_line2 = tangent_slope2*xcoord2+yint2;
plot(xcoord2,tangent_line2,'r','LineWidth',2);

perpendicular_slope2 = -1/tangent_slope2;
yintp2 = (intersection2(2)-perpendicular_slope2*intersection2(1));
perpendicular_line2 = perpendicular_slope2*xcoord2+yintp2;

plot(xcoord2,perpendicular_line2,'r','LineWidth',2);

%Draws the Radial and Tangential velocity vectors connected to total
%velocity vector
xline2 = [stream2_xtop, stream2_xbot];
yline2 = [stream2_ytop, stream2_ybot];
line(xline2,yline2,'Color','c','LineWidth',2);

tanline_intercept2 = stream2_ytop - tangent_slope2*stream2_xtop;
perpline_intercept2 = stream2_ybot - perpendicular_slope2*stream2_xbot;

xintersect_point2 = -(perpline_intercept2 - tanline_intercept2)/(-
tangent_slope2 + 1/-tangent_slope2);
yintersect_point2 = tangent_slope2*xintersect_point2 +
tanline_intercept2;

xline_tan2 = [stream2_xtop, xintersect_point2];
yline_tan2 = [stream2_ytop, yintersect_point2];
```

```
xline_perp2 = [stream2_xbot, xintersect_point2];
yline_perp2 = [stream2_ybot, yintersect_point2];
line(xline_tan2,yline_tan2,'Color','c','LineWidth',2);
line(xline_perp2,yline_perp2,'Color','c','LineWidth',2);

fs2 = sqrt((stream2_xtop-stream2_xbot)^2 + (stream2_ytop-
stream2_ybot)^2);
fs2_perp = sqrt((stream2_xtop-xintersect_point2)^2 + (stream2_ytop-
yintersect_point2)^2);
fs2_tan = sqrt((stream2_xbot-xintersect_point2)^2 + (stream2_ybot-
yintersect_point2)^2);

anglet2 = atan(fs2_perp/fs2_tan)*180/pi; %Stream angle in degrees
anglet2rad = atan(fs2_perp/fs2_tan);  %Stream angle in radians

%tangential and radial velocities
vel2tan = sin(anglet2rad)*vel2;
vel2rad = cos(anglet2rad)*vel2;

%print results
fprintf('Intersection point on disk (stream exit point)
%6.2f \n',intersection2);
fprintf('Angle between fuel stream exit and end exit hole position
%6.2f \n',angle2);
fprintf('Rotational distance of disk over time fuel stream 2 has
traveled (m) %6.2f \n',circumdist2/480*.0254);
fprintf('Fuel stream 2 travel time (s)
%2.8f \n',time2);
fprintf('Fuel Stream 2 Tangential Angle of fuel stream is (deg)
%6.2f \n\n',anglet2);
fprintf('Fuel Stream 2 Tangential Velocity is (m/s)
%6.2f \n',vel2tan);
fprintf('Fuel Stream 2 Radial Velcoity is (m/s)
%6.2f \n',vel2rad);
fprintf('Fuel Stream 2 Total Velocity is (m/s)
%6.2f \n\n\n',vel2);
%%

%Fuel Stream 3

%creates a line from the fuel stream back to exit point on disk
tvs3 = (stream3_ytop - stream3_ybot)/(stream3_xtop - stream3_xbot);
%total velocity slope

bstream3 = stream3_ytop - tvs3*stream3_xtop;  %intercept

xstream3 = stream3_xtop:1:1900;
ystream3 = zeros(1,length(xstream3));
for n3 = 1:length(xstream3)
    ystream3(n3) = tvs3*xstream3(n3) + bstream3;
end

plot(xstream3,ystream3,'LineWidth',2)

X3 = zeros(2,1);
```

```
z3 = bstream3 - yc;
aX3 = tvs3^2 + 1;
bX3 = 2*(tvs3*z3 - xc);
constX3 = xc^2 +z3^2 - radius^2;

X3(1) = (-bX3 + sqrt(bX3^2 - 4*constX3*aX3))/(2*aX3);
X3(2) = (-bX3 - sqrt(bX3^2 - 4*constX3*aX3))/(2*aX3);

Y3 = tvs3*min(X3) + bstream3;
intersection3 = [min(X3),Y3];

plot(min(X3),Y3,'rx','Linewidth',4)

xline_angletop3 = [xc, intersection3(1)];
yline_angletop3 = [yc, intersection3(2)];

%creates line from intersection point to center of disk
line(xline_angletop3,yline_angletop3,'Color','g','LineWidth',2);

%calculates angle between intersection point and exit hole location
%vector(A)*vector(B)*cos(theta) = lAl*lBl
vect13 = [(xlocation-xc) (ylocation-yc)];
vect23 = [(intersection3(1)-xc) (intersection3(2)-yc)];
dp3 = dot(vect13, vect23)/norm(vect13)/norm(vect23);
angle3 = acos(dp3)*180/pi;

%distance disk has traveled over angle/rotational speed/time disk has
%traveled in picture
circumdist3 = angle3/360*(2*pi*radius); %circumference in pixels
time3 = circumdist3/linear_rot_velocity;

%distance fuel has traveled in picture (intersection point to bottom of
%fuel stream
stream3_dist = sqrt(abs(intersection3(1) - stream3_xbot)^2 +
abs(intersection3(2) - stream3_ybot)^2) - dia3; %stream linear distance
in pixels

%total velocity
vel3 = (stream3_dist/480*.0254)/time3;

%Tangent and Radial slopes for fuel stream 2
tangent_slope3 = -(intersection3(1)-xc)/(intersection3(2)-yc);
xintersectfinal3 = intersection3(1) - 200;

xcoord3 = xintersectfinal3:intersection3(1);
yint3 = (intersection3(2)-tangent_slope3*intersection3(1));

tangent_line3 = tangent_slope3*xcoord3+yint3;
plot(xcoord3,tangent_line3,'r','LineWidth',2);

perpendicular_slope3 = -1/tangent_slope3;
yintp3 = (intersection3(2)-perpendicular_slope3*intersection3(1));
perpendicular_line3 = perpendicular_slope3*xcoord3+yintp3;

plot(xcoord3,perpendicular_line3,'r','LineWidth',2);
```

```
%Draws the Radial and Tangential velocity vectors connected to total
%velocity vector
xline3 = [stream3_xtop, stream3_xbot];
yline3 = [stream3_ytop, stream3_ybot];
line(xline3,yline3,'Color','g','LineWidth',2);

tanline_intercept3 = stream3_ytop - tangent_slope3*stream3_xtop;
perpline_intercept3 = stream3_ybot - perpendicular_slope3*stream3_xbot;

xintersect_point3 = -(perpline_intercept3 - tanline_intercept3)/(-
tangent_slope3 + 1/-tangent_slope3);
yintersect_point3 = tangent_slope3*xintersect_point3 +
tanline_intercept3;

xline_tan3 = [stream3_xtop, xintersect_point3];
yline_tan3 = [stream3_ytop, yintersect_point3];
xline_perp3 = [stream3_xbot, xintersect_point3];
yline_perp3 = [stream3_ybot, yintersect_point3];
line(xline_tan3,yline_tan3,'Color','g','LineWidth',2);
line(xline_perp3,yline_perp3,'Color','g','LineWidth',2);

fs3 = sqrt((stream3_xtop-stream3_xbot)^2 + (stream3_ytop-
stream3_ybot)^2);
fs3_perp = sqrt((stream3_xtop-xintersect_point3)^2 + (stream3_ytop-
yintersect_point3)^2);
fs3_tan = sqrt((stream3_xbot-xintersect_point3)^2 + (stream3_ybot-
yintersect_point3)^2);

anglet3 = atan(fs3_perp/fs3_tan)*180/pi;  %Stream angle in degrees
anglet3rad = atan(fs3_perp/fs3_tan);    %Stream angle in radians

%tangential and radial velocities
vel3tan = sin(anglet3rad)*vel3;
vel3rad = cos(anglet3rad)*vel3;

%print results
fprintf('Intersection point on disk (stream exit point)
%6.2f \n',intersection3);
fprintf('Angle between fuel stream exit and end exit hole position
%6.2f \n',angle3);
fprintf('Rotational distance of disk over time fuel stream 3 has
traveled (m) %6.2f \n',circumdist3/480*.0254);
fprintf('Fuel stream 3 travel time (s)
%2.8f \n',time3);
fprintf('Fuel Stream 3 Tangential Angle of fuel stream is (deg)
%6.2f \n\n',anglet3);
fprintf('Fuel Stream 3 Tangential Velocity is (m/s)
%6.2f \n',vel3tan);
fprintf('Fuel Stream 3 Radial Velcoity is (m/s)
%6.2f \n',vel3rad);
fprintf('Fuel Stream 3 Total Velocity is (m/s)
%6.2f \n\n\n',vel3);
%%
%Fuel Stream 4

%creates a line from the fuel stream back to exit point on disk
```

```
tvs4 = (stream4_ytop - stream4_ybot)/(stream4_xtop - stream4_xbot);
%total velocity slope

bstream4 = stream4_ytop - tvs4*stream4_xtop;  %intercept

xstream4 = stream4_xtop:1:1900;
ystream4 = zeros(1,length(xstream4));
for n4 = 1:length(xstream4)
    ystream4(n4) = tvs4*xstream4(n4) + bstream4;
end

plot(xstream4,ystream4,'LineWidth',2)

X4 = zeros(2,1);

z4 = bstream4 - yc;
aX4 = tvs4^2 + 1;
bX4 = 2*(tvs4*z4 - xc);
constX4 = xc^2 +z4^2 - radius^2;

X4(1) = (-bX4 + sqrt(bX4^2 - 4*constX4*aX4))/(2*aX4);
X4(2) = (-bX4 - sqrt(bX4^2 - 4*constX4*aX4))/(2*aX4);

Y4 = tvs4*min(X4) + bstream4;
intersection4 = [min(X4),Y4];

plot(min(X4),Y4,'rx','Linewidth',4)

xline_angletop4 = [xc, intersection4(1)];
yline_angletop4 = [yc, intersection4(2)];

%creates line from intersection point to center of disk
line(xline_angletop4,yline_angletop4,'Color','g','LineWidth',2);

%calculates angle between intersection point and exit hole location
%vector(A)*vector(B)*cos(theta) = lAl*lBl
vect14 = [(xlocation-xc) (ylocation-yc)];
vect24 = [(intersection4(1)-xc) (intersection4(2)-yc)];
dp4 = dot(vect14, vect24)/norm(vect14)/norm(vect24);
angle4 = acos(dp4)*180/pi;

%distance disk has traveled over angle/rotational speed/time disk has
%traveled in picture
circumdist4 = angle4/360*(2*pi*radius); %circumference in pixels
time4 = circumdist4/linear_rot_velocity;

%distance fuel has traveled in picture (intersection point to bottom of
%fuel stream
stream4_dist = sqrt(abs(intersection4(1) - stream4_xbot)^2 +
abs(intersection4(2) - stream4_ybot)^2) - dia4; %stream linear distance
in pixels

%total velocity
vel4 = (stream4_dist/480*.0254)/time4;
```

```
%Tangent and Radial slopes for fuel stream 2
tangent_slope4 = -(intersection4(1)-xc)/(intersection4(2)-yc);
xintersectfinal4 = intersection4(1) - 200;

xcoord4 = xintersectfinal4:intersection4(1);
yint4 = (intersection4(2)-tangent_slope4*intersection4(1));

tangent_line4 = tangent_slope4*xcoord4+yint4;
plot(xcoord4,tangent_line4,'r','LineWidth',2);

perpendicular_slope4 = -1/tangent_slope4;
yintp4 = (intersection4(2)-perpendicular_slope4*intersection4(1));
perpendicular_line4 = perpendicular_slope4*xcoord4+yintp4;

plot(xcoord4,perpendicular_line4,'r','LineWidth',2);

%Draws the Radial and Tangential velocity vectors connected to total
%velocity vector
xline4 = [stream4_xtop, stream4_xbot];
yline4 = [stream4_ytop, stream4_ybot];
line(xline4,yline4,'Color','m','LineWidth',2);

tanline_intercept4 = stream4_ytop - tangent_slope4*stream4_xtop;
perpline_intercept4 = stream4_ybot - perpendicular_slope4*stream4_xbot;

xintersect_point4 = -(perpline_intercept4 - tanline_intercept4)/(-
tangent_slope4 + 1/-tangent_slope4);
yintersect_point4 = tangent_slope4*xintersect_point4 +
tanline_intercept4;

xline_tan4 = [stream4_xtop, xintersect_point4];
yline_tan4 = [stream4_ytop, yintersect_point4];
xline_perp4 = [stream4_xbot, xintersect_point4];
yline_perp4 = [stream4_ybot, yintersect_point4];
line(xline_tan4,yline_tan4,'Color','m','LineWidth',2);
line(xline_perp4,yline_perp4,'Color','m','LineWidth',2);

fs4 = sqrt((stream4_xtop-stream4_xbot)^2 + (stream4_ytop-
stream4_ybot)^2);
fs4_perp = sqrt((stream4_xtop-xintersect_point4)^2 + (stream4_ytop-
yintersect_point4)^2);
fs4_tan = sqrt((stream4_xbot-xintersect_point4)^2 + (stream4_ybot-
yintersect_point4)^2);

anglet4 = atan(fs4_perp/fs4_tan)*180/pi; %Stream angle in degrees
anglet4rad = atan(fs4_perp/fs4_tan);  %Stream angle in radians

%tangential and radial velocities
vel4tan = sin(anglet4rad)*vel4;
vel4rad = cos(anglet4rad)*vel4;

%print results
fprintf('Diesel Test 1 Results');
fprintf('Intersection point on disk (stream exit point)
%6.2f \n',intersection4);
```

```
fprintf('Angle between fuel stream exit and end exit hole position
%6.2f \n',angle4);
fprintf('Rotational distance of disk over time fuel stream 4 has
traveled (m) %6.2f \n',circumdist4/480*.0254);
fprintf('Fuel stream 4 travel time (s)
%2.8f \n',time4);
fprintf('Fuel Stream 4 Tangential Angle of fuel stream is (deg)
%6.2f \n\n',anglet4);
fprintf('Fuel Stream 4 Tangential Velocity is (m/s)
%6.2f \n',vel4tan);
fprintf('Fuel Stream 4 Radial Velcoity is (m/s)
%6.2f \n',vel4rad);
fprintf('Fuel Stream 4 Total Velocity is (m/s)
%6.2f \n\n\n',vel4);


angles1 = [anglet1rad; anglet2rad; anglet3rad; anglet4rad];
%%
%Displays a figure of the fuel stream distance from the disk exit as a
%function of time

distplotd1 = zeros(5,2);
distplotd1(:,1) = [0,time1,time2,time3,time4];
distplotd1(:,2) =
[0,stream1_dist/480*.0254,stream2_dist/480*.0254,stream3_dist/480*.0254,
stream4_dist/480*.0254];
```

Example Overall Diesel Comparison (Tests 1-3)

```
function
[ave_diesel_lead_pos,ave_diesel_lead_vel,ave_diesel_lead_time,td1,td2,td
3,vd1,vd2,vd3,pd1,pd2,pd3,ttd1,ttd2,ttd3,cd,cipd] =
overall_diesel_results

%This m-file is used to compiled all of the Diesel test results for
%comparison and to show reproducibility

%Outputs from this m-file include a comparison plots for the leading
edge
%of the trajectory curve as position versus time as well as the
instantaneous velocity versus time

[distplotd1,angles1] = Velocity_calc_by_angle_diesel1;
[distplotd2,angles2] = Velocity_calc_by_angle_diesel2;
[distplotd3,angles3] = Velocity_calc_by_angle_diesel3;

%Position

figure;
hold on
plot(distplotd1(:,1),distplotd1(:,2),'-
or',distplotd2(:,1),distplotd2(:,2),'-
og',distplotd3(:,1),distplotd3(:,2),'-ob')
```

```
legend('Diesel 1','Diesel 2','Diesel 3');
xlabel('Time (sec)')
ylabel('Position (m)')
title('Diesel comparison of results (position)')

%%
% Velocity

%Test 1
x1 = distplotd1(:,2);
t1 = distplotd1(:,1);

%s1 = fitoptions('method','nonlinearleastsquares','lower',[0
0],'upper',[Inf, Inf]);
f1 = fittype('1/a * log(a*b*x+1)');
[temp1,r1] = fit(t1,x1,f1);  %curve fitting the custom fit f1 to diesel
test 1 data points

c1 = temp1.a;
v01 = temp1.b;
time1 = linspace(0,1.2e-3,100);
v1 = 1./(c1*time1 + 1/v01); %instanteous velocity curve
%Tangential and Radial velocity components
tan1 = sin(mean(angles1(1:end)))*v1;
rad1 = cos(mean(angles1(1:end)))*v1;

%Test 2
x2 = distplotd2(:,2);
t2 = distplotd2(:,1);

%s2 = fitoptions('method','nonlinearleastsquares','lower',[0
0],'upper',[Inf, Inf]);
f2 = fittype('1/a * log(a*b*x+1)');
[temp2,r2] = fit(t2,x2,f2);

c2 = temp2.a;
v02 = temp2.b;
time2 = linspace(0,1.2e-3,100);
v2 = 1./(c2*time2 + 1/v02);

%Tangential and Radial velocity components
tan2 = sin(mean(angles2(1:end)))*v2;
rad2 = cos(mean(angles2(1:end)))*v2;

%Test 3
x3 = distplotd3(:,2);
t3 = distplotd3(:,1);

%s3 = fitoptions('method','nonlinearleastsquares','lower',[0
0],'upper',[Inf, Inf]);
f3 = fittype('1/a * log(a*b*x+1)');
[temp3,r3] = fit(t3,x3,f3);

c3 = temp3.a;
v03 = temp3.b;
time3 = linspace(0,1.2e-3,100);
```

```
v3 = 1./(c3*time3 + 1/v03);

%Tangential and Radial velocity components
tan3 = sin(mean(angles3(1:end)))*v3;
rad3 = cos(mean(angles3(1:end)))*v3;

%Combined
X = [distplotd1;distplotd2;distplotd3];
xX = X(:,2);
tX = X(:,1);

%sX = fitoptions('method','nonlinearleastsquares','lower',[0
0],'upper',[Inf, Inf]);
fX = fittype('1/a * log(a*b*x+1)');
[tempX,rX] = fit(tX,xX,fX);
ciX = confint(tempX);
time = linspace(0,1E-3,11);
cipd = predint(tempX,time,0.95,'functional','on'); %creates confidence
intervals for combined curve

cX = tempX.a;
v0X = tempX.b;
timeX = linspace(0,1.2e-3,100);
vX = 1./(cX*timeX + 1/v0X);

%plot of three diesel curves

figure;
hold on
plot(temp1,'b')
plot(temp2,'r')
plot(temp3,'g')

legend('Diesel 1','Diesel 2','Diesel 3');
xlabel('Time (sec)')
ylabel('Position (m)')
title('Diesel comparison of position fitted curves')

figure;
plot(time1,v1,'b',time1,tan1,'b-.',time1,rad1,'b--
',time2,v2,'g',time2,tan2,'g-.',time2,rad2,'g--',...
time3,v3,'r',time3,tan3,'r-.',time3,rad3,'r--')

legend('Diesel 1 Total','Diesel 1 Tangential','Diesel 1 Radial','Diesel
2 Total',...
'Diesel 2 Tangential','Diesel 2 Radial','Diesel 3 Total','Diesel 3
Tangential','Diesel 3 Radial');
xlabel('Time (sec)')
ylabel('Velocity (m/s)')
title('Diesel comparison of results (instantaneous velocity)')


%plot of average of all three diesel curves
figure;
hold on
for n = 1:length(tX)
```

```
plot(tX(n),xX(n),'o','MarkerEdgeColor','k','MarkerFaceColor','g','Marker
Size',5)
end
plot(tempX)
plot(time,cipd,'b--')
axis([0 1E-3 0 0.08])

xlabel('Time (sec)')
ylabel('Position (m)')
title('Diesel Average Position Curve')

figure;
plot(timeX,vX)

xlabel('Time (sec)')
ylabel('Velocity (m/s)')
title('Diesel Average Instantaneous Velocity Curve')

td1 = distplotd1(:,1);
td2 = distplotd2(:,1);
td3 = distplotd3(:,1);

ttd1 = time1;
ttd2 = time2;
ttd3 = time3;

pd1 = distplotd1(:,2);
pd2 = distplotd2(:,2);
pd3 = distplotd3(:,2);

vd1 = v1;
vd2 = v2;
vd3 = v3;

cd = X;

ave_diesel_lead_pos = tempX;
ave_diesel_lead_vel = vX;
ave_diesel_lead_time = timeX;

xlswrite('ci.xls', {'Results', '', 'Upper Bound','Lower
Bound';'a',tempX.a ciX(1) ciX(2); 'b',tempX.b ciX(3) ciX(4)},
'diesel','A1')
xlswrite('ci.xls', {'R2';rX.rsquare}, 'diesel','E1')
```

Example Overall Comparison For All Fuels

```
function overall_fuel_comparison
%This m-file is used to compile all of the fuel test for comparison.
%Outputs from this m-file are position and instantaneous velocity curves
%along the leading edge of the trajectory for all of the tests as well
as
%position and instantaneous velocity curves along the leading edge of
the
```

```
%trajectory for combined curves i.e. all of the diesel tests form one
curve
%Also output from this m-file is a figure that containes 4 subplots with
%each combined fuel curve along with its 95% confidence interval and
%original data points

[ave_diesel_lead_pos,ave_diesel_lead_vel,ave_diesel_lead_time,td1,td2,td
3,vd1,vd2,vd3,pd1,pd2,pd3,ttd1,ttd2,ttd3,cd,cipd] =
overall_diesel_results;
[ave_jeta_lead_pos,ave_jeta_lead_vel,ave_jeta_lead_time,tjf1,tjf2,tjf3,v
jf1,vjf2,vjf3,pjf1,pjf2,pjf3,ttjf1,ttjf2,ttjf3,cj,cipj] =
overall_jeta_results;
[ave_p184_lead_pos,ave_p184_lead_vel,ave_p184_lead_time,t184_1,t184_2,t1
84_3,v184_1,v184_2,v184_3,p184_1,p184_2,p184_3,tt184_1,tt184_2,tt184_3,c
p184,cipp184] = overall_P184_results;
[ave_p186_lead_pos,ave_p186_lead_vel,ave_p186_lead_time,t186_1,t186_2,t1
86_3,v186_1,v186_2,v186_3,p186_1,p186_2,p186_3,tt186_1,tt186_2,tt186_3,c
p186,cipp186] = overall_P186_results;


%plots of each of the 3 test curves for position and velocity for each
%fuel

%position
figure;
hold on

plot(td1,pd1,'-og',td2,pd2,'-og',td3,pd3,'-og')
plot(tjf1,pjf1,'-ob',tjf2,pjf2,'-ob',tjf3,pjf3,'-ob')
plot(t184_1,p184_1,'-or',t184_2,p184_2,'-or',t184_3,p184_3,'-or')
plot(t186_1,p186_1,'-oy',t186_2,p186_2,'-oy',t186_3,p186_3,'-oy')

% pd1,pd2,pd3
% pjf1,pjf2,pjf3
% p184_1,p184_2,p184_3
% p186_1,p186_2,p186_3


legend('Diesel 1','Diesel 2','Diesel 3','Jet-A 1','Jet-A 2','Jet-A
3','P184 1','P184 2','P184 3','P186 1','P186 2','P186 3')
xlabel('Time (sec)')
ylabel('Position (m)')
title('Fuel Lead Edge Trajectory Position Comparison')

figure;
hold on

%velocity
plot(ttd1,vd1,'-g',ttd2,vd2,'-g',ttd3,vd3,'-g')
plot(ttjf1,vjf1,'-b',ttjf2,vjf2,'-b',ttjf3,vjf3,'-b')
plot(tt184_1,v184_1,'-r',tt184_2,v184_2,'-r',tt184_3,v184_3,'-r')
plot(tt186_1,v186_1,'-m',tt186_2,v186_2,'-m',tt186_3,v186_3,'-m')

legend('Diesel 1','Diesel 2','Diesel 3','Jet-A 1','Jet-A 2','Jet-A
3','P184 1','P184 2','P184 3','P186 1','P186 2','P186 3')
xlabel('Time (sec)')
```

```
ylabel('Velocity (m/s)')
title('Fuel Lead Edge Trajectory Instantaneous Velocity Comparison')

%plots of the average position and velocity curves for each fuel
figure;
hold on

plot(ave_diesel_lead_pos,'g')
plot(ave_jeta_lead_pos,'b')
plot(ave_p184_lead_pos,'r')
plot(ave_p186_lead_pos,'m')

axis([0 1.2E-3 0 0.1])
legend('Diesel','Jet-A','P184','P186')
xlabel('Time (sec)')
ylabel('Position (m)')
title('Average Fuel Lead Edge Trajectory Position Comparison')

figure;
hold on

plot(ave_diesel_lead_time, ave_diesel_lead_vel,'g')
plot(ave_jeta_lead_time, ave_jeta_lead_vel,'b')
plot(ave_p184_lead_time, ave_p184_lead_vel,'r')
plot(ave_p186_lead_time, ave_p186_lead_vel,'m')

legend('Diesel','Jet-A','P184','P186')
xlabel('Time (sec)')
ylabel('Velocity (m/s)')
title('Average Fuel Lead Edge Trajectory Instantaneous Velocity
Comparison')

%plots 1 subplot of 4 plots that have the CI for each average fuel curve
xd = cd(:,2);
td = cd(:,1);

xj = cj(:,2);
tj = cj(:,1);

x184 = cp184(:,2);
t184 = cp184(:,1);

x186 = cp186(:,2);
t186 = cp186(:,1);

time = linspace(0,1E-3,11);

figure;

%Diesel
subplot(2,2,1)
hold on
for n = 1:length(td)

plot(td(n),xd(n),'o','MarkerEdgeColor','k','MarkerFaceColor','g','Marker
Size',5)
```

```
end
plot(ave_diesel_lead_pos)
plot(time,cipd,'b--')
axis([0 1E-3 0 0.08])

xlabel('Time (sec)')
ylabel('Position (m)')
title('Diesel Average Position Curve')

%JetA
subplot(2,2,2)
hold on
for n = 1:length(tj)

plot(tj(n),xj(n),'o','MarkerEdgeColor','k','MarkerFaceColor','g','Marker
Size',5)
end
plot(ave_jeta_lead_pos)
plot(time,cipj,'b--')
axis([0 1E-3 0 0.08])

xlabel('Time (sec)')
ylabel('Position (m)')
title('Jet-A Average Position Curve')

%P184
subplot(2,2,3)
hold on
for n = 1:length(t184)

plot(t184(n),x184(n),'o','MarkerEdgeColor','k','MarkerFaceColor','g','Ma
rkerSize',5)
end
plot(ave_p184_lead_pos)
plot(time,cipp184,'b--')
axis([0 1E-3 0 0.08])

xlabel('Time (sec)')
ylabel('Position (m)')
title('P184 Average Position Curve')

%P186
subplot(2,2,4)
hold on
for n = 1:length(t186)

plot(t186(n),x186(n),'o','MarkerEdgeColor','k','MarkerFaceColor','g','Ma
rkerSize',5)
end
plot(ave_p186_lead_pos)
plot(time,cipp186,'b--')
axis([0 1E-3 0 0.08])

xlabel('Time (sec)')
ylabel('Position (m)')
title('P186 Average Position Curve')
```

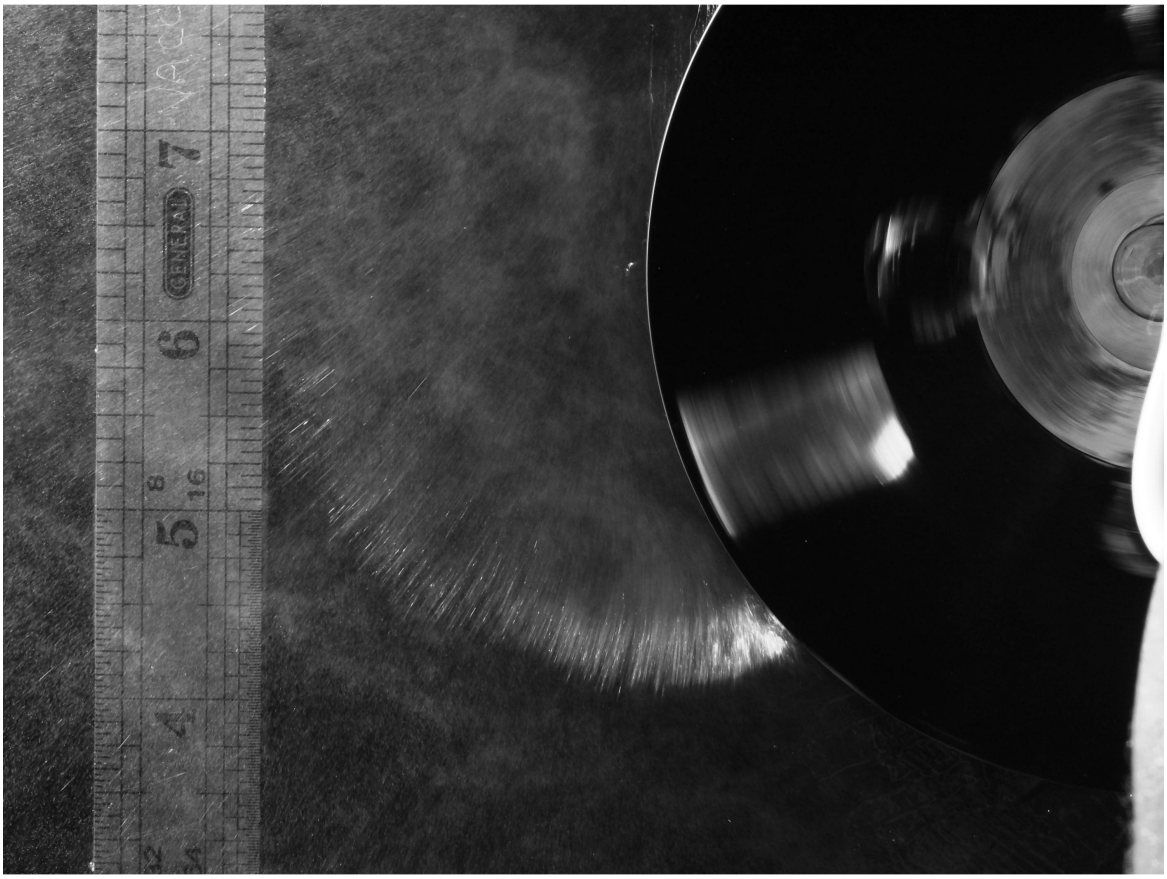

Figure 93. Grayscale version of the original diesel test 1 image. This image is displayed with imtool and used to pick out the top and bottom points along the chosen fuel streams.

Diesel Test 1 Angle Technique Results
Note: Velocities calculated are average velocities

Intersection point on disk (stream exit point)	1730.20
Intersection point on disk (stream exit point)	1280.53
Angle between fuel stream exit and end exit hole position	15.03
Rotational distance of disk over time fuel stream 1 has traveled (m)	0.02
Fuel stream 1 travel time (s)	0.00029670
Fuel Stream 1 Tangential Angle of fuel stream is (deg)	56.79
Fuel Stream 1 Tangential Velocity is (m/s)	54.93
Fuel Stream 1 Radial Velocity is (m/s)	35.97
Fuel Stream 1 Total Velocity is (m/s)	65.66
Intersection point on disk (stream exit point)	1603.47
Intersection point on disk (stream exit point)	967.97
Angle between fuel stream exit and end exit hole position	30.41
Rotational distance of disk over time fuel stream 2 has traveled (m)	0.04
Fuel stream 2 travel time (s)	0.0006
Fuel Stream 2 Tangential Angle of fuel stream is (deg)	54.58
Fuel Stream 2 Tangential Velocity is (m/s)	49.74
Fuel Stream 2 Radial Velocity is (m/s)	35.38
Fuel Stream 2 Total Velocity is (m/s)	61.04
Intersection point on disk (stream exit point)	1591.90
Intersection point on disk (stream exit point)	390.74
Angle between fuel stream exit and end exit hole position	56.88
Rotational distance of disk over time fuel stream 3 has traveled (m)	0.07
Fuel stream 3 travel time (s)	0.0011
Fuel Stream 3 Tangential Angle of fuel stream is (deg)	59.75
Fuel Stream 3 Tangential Velocity is (m/s)	47.94
Fuel Stream 3 Radial Velcoity is (m/s)	27.96
Fuel Stream 3 Total Velocity is (m/s)	55.50
Intersection point on disk (stream exit point)	1605.71
Intersection point on disk (stream exit point)	332.94
Angle between fuel stream exit and end exit hole position	59.58
Rotational distance of disk over time fuel stream 4 has traveled (m)	0.07
Fuel stream 4 travel time (s)	0.0012
Fuel Stream 4 Tangential Angle of fuel stream is (deg)	52.00
Fuel Stream 4 Tangential Velocity is (m/s)	43.40
Fuel Stream 4 Radial Velocity is (m/s)	33.91
Fuel Stream 4 Total Velocity is (m/s)	55.08

Additional Position and Instantaneous Velocity Results

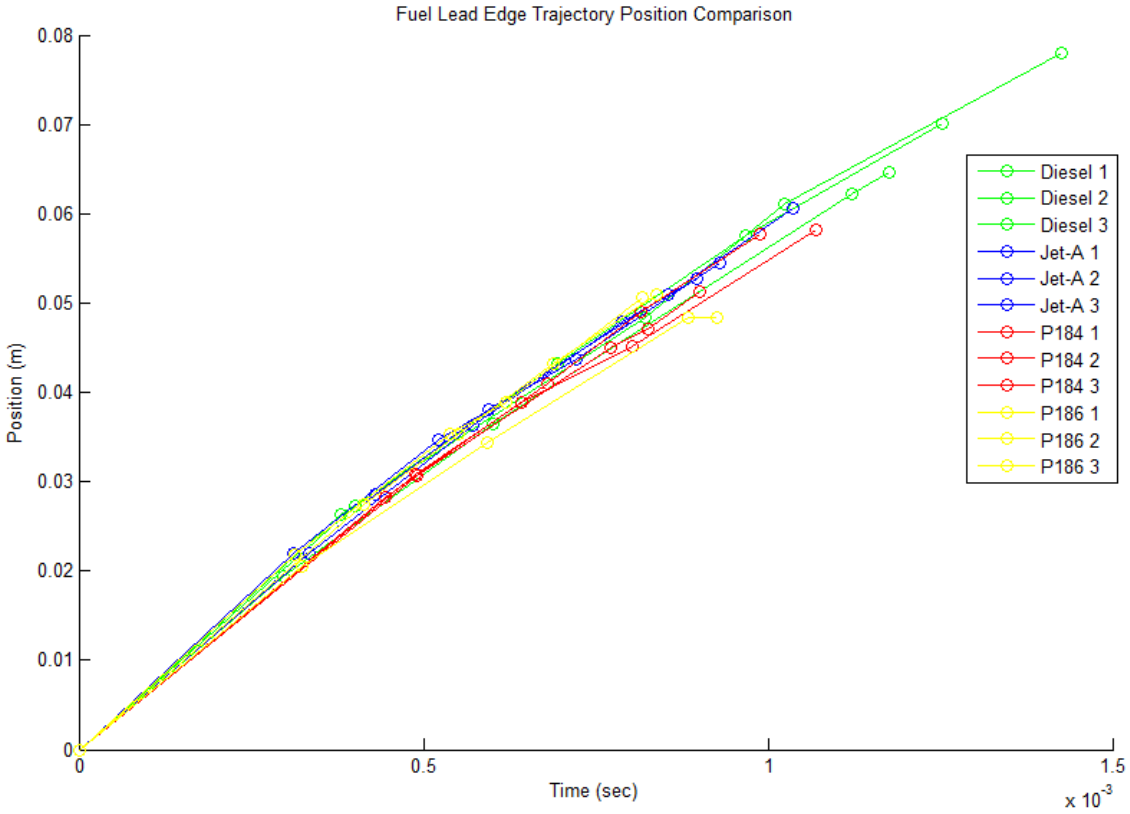

Figure 94. Comparison of leading edge fuel trajectory position curves using original data points.

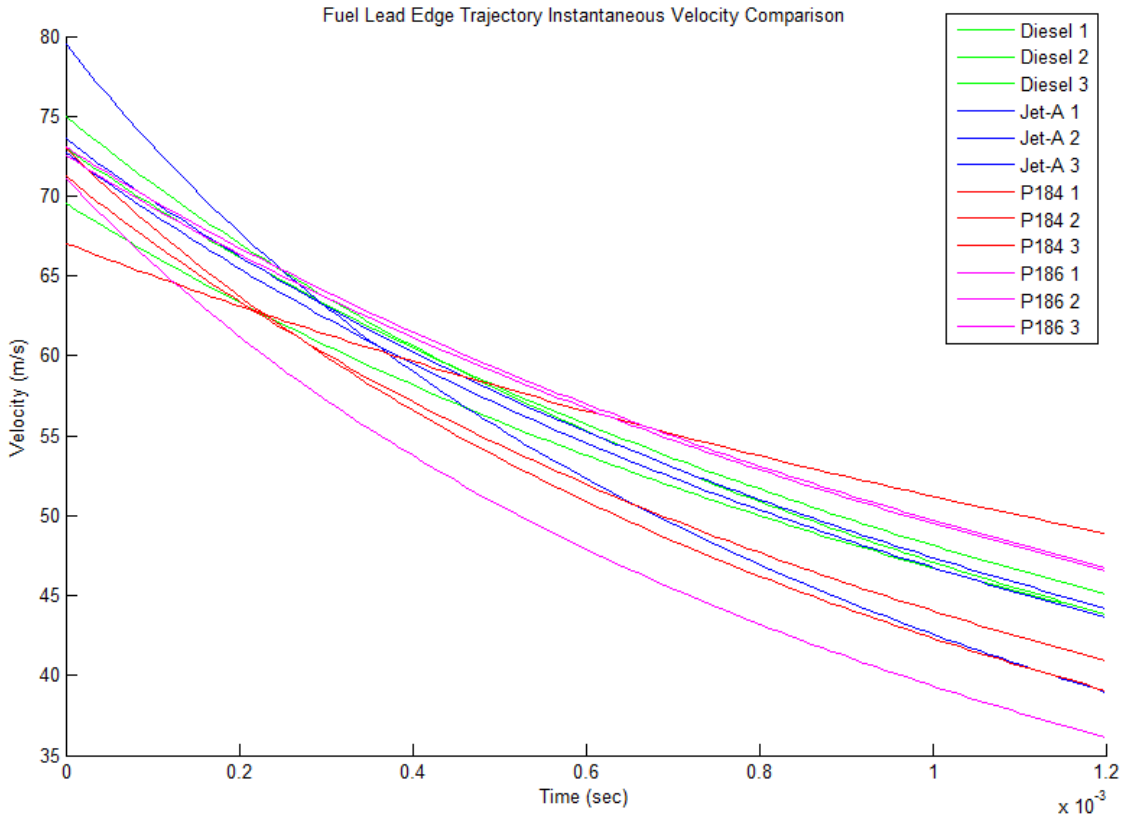

Figure 95. Comparison of leading edge fuel trajectory instantaneous velocity curves.

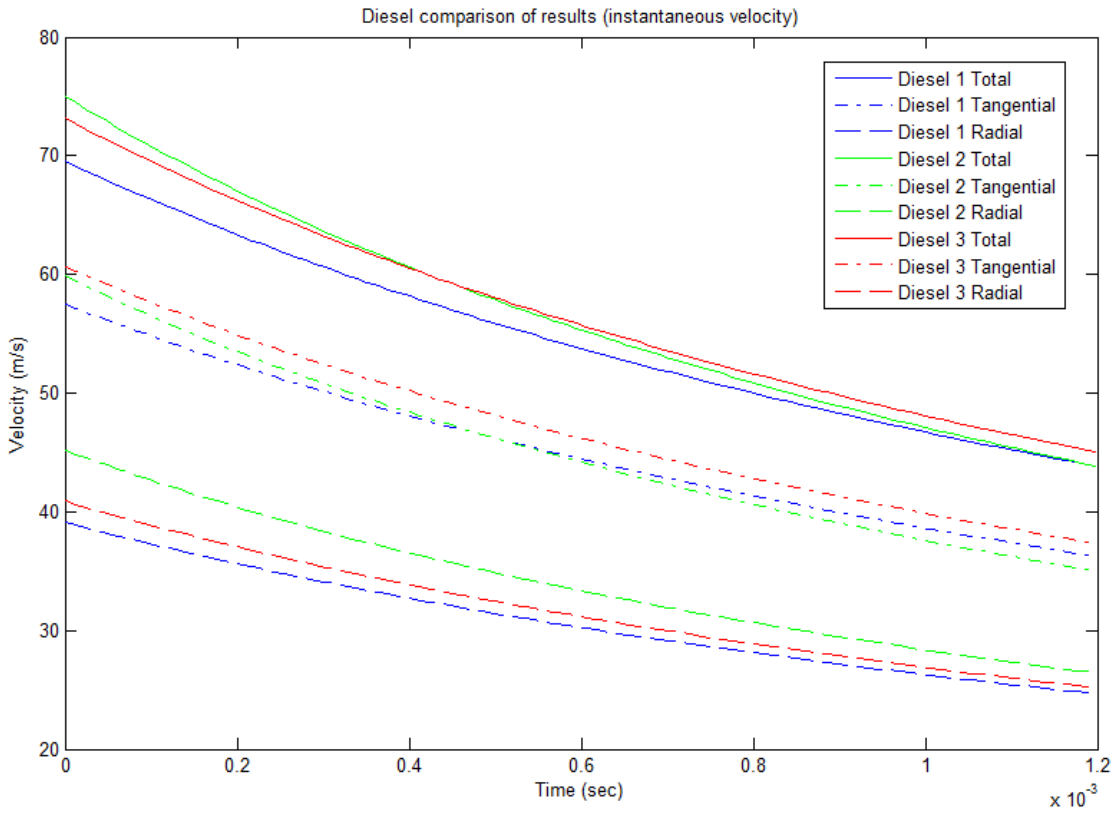

Figure 96. Instantaneous velocity component comparison of the three Diesel tests. The tangential velocity vector magnitude is the major contributor to the total velocity vector magnitude.

Appendix I: Trigger Circuit Design Written by and placed in document with permission of Dr. Christopher Martin, Post Doctoral Fellow, Virginia Active Combustion Control Group, Virginia Tech, 2010

Introduction

When collecting data in systems that have repeating processes such as rotating machinery or a periodic signal (such as in system ID), it is not unusual to take measurements that are sufficiently quick to be characterized as "instantaneous," but that cannot be "resampled" fast enough to take multiple measurements per process cycle. Most frequently, this has applications in high-speed photography, wherein the shutter speed is very fast, but images can only be taken at low frequencies due to data rate or mechanical limitations.

The solution is to collect data only once in a process cycle, but to time the instant in which the measurement is taken relative to the repetition of the cycle. Called "phase locking," this is commonly accomplished by producing a periodic TTL trigger from that signal, waiting some period of time, and outputting a TTL trigger to initiate the measurement process.

Figure 95 shows an example period process that has been transduced to a periodic logic signal, and the delayed trigger that can be used to initiate a phase-locked measurement process. Since the measurement may take many cycles before it is ready to repeat, the example shows only a single output signal.

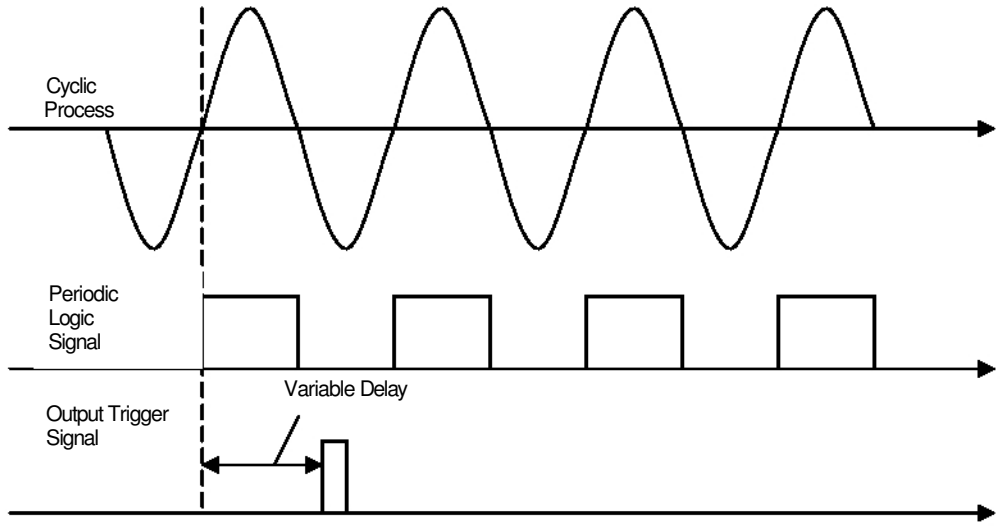

Figure 97. The cyclic process, logical signal, and single delayed output trigger that initiates a flash.

Connection & Operation

The front panel two sets of identical controls connecting to two sets of identical circuitry; each set representing one of the channels. Shown in Figure 2, each channel has three BNC connections labeled INPUT, OUTPUT, and DISABLE, a dial potentiometer and decade switch for setting the delay, a RESET button and corresponding READY LED. The only connections on the front panel that are not duplicated for the two channels is the POWER connection on the far right. The following sections address the function and proper use of each element.

INPUT (BNC): This is the logical input signal. Normally, a raw sensor signal needs to be fed to a device such as a Schmidt trigger before being fed into the input, but a sensor signal with sufficient amplitude will suffice as a trigger signal. The logical circuitry inside uses a single-ended voltage range determined by the power. If the power is supplied with +5V, then a "high" input is near +5V.

OUTPUT (BNC): The delayed trigger signal is output on this connector. The trigger signal is nominally 0V, but toggles high for a constant-width (~0.1ms) pulse. The pulse

voltage is determined by the POWER connection.

DISABLE (BNC): It is not uncommon that a trigger event should wait until some critical event in the process. When there is a voltage present on the DISABLE pin, the INPUT pin is pulled low, disabling the trigger circuitry. It is important to note that the DISABLE threshold is lower than standard TTL thresholds, but it will respond well to TTL inputs.

0-1ms (knob): The delay is tuned via a potentiometer. By default, the delay can be tuned between 0 and a nominal 1ms delay. It is important to note that, the circuit has occasionally exhibited difficulties at very small delays. This is related to the amount of time allowed for various capacitances to discharge. When that time is too short, sometimes there is residual charge that causes unexpected behaviors.

1x / 10x (switch): To allow the circuit to be tuned accurately for a wider variety of delays, the decade selector can be toggled between 1x and 10x modes. When in 1x mode, the delay range is 0-1ms as labeled. When in 10x mode, the delay range is twice that; 0-10ms. This allows smaller delays to be more finely tuned, while also providing the option for longer delays.

READY (LED): The READY LED indicates when the channel is armed and waiting for a trigger. It does not indicate when the circuit is disabled by the DISABLE input. When lit, the output trigger will be executed after the first input trigger event. Only one output pulse will be generated until the circuit is reset and the READY LED is lit.

RESET (button): The RESET button re-arms the circuit after it has already triggered. When the button is first pressed, the internal logic is re-armed to await an input pulse, and the READY LED is lit. While the RESET button is down, the INPUT signal is disabled in much the same manner as if there is a voltage present on the DISABLE connector. This prevents unexpected triggers during the reset process. A trigger will not be allowed until the RESET button is released.

POWER (banana/screw terminals): The power terminals are red and black, representing

positive and negative power connections respectively. These are rated on the front panel for 5-15V, but can realistically be powered for a wider range than that. This voltage determines the voltage of the "high" and "low" outputs. The inputs are spaced to accept a standard BNC-to-banana adapter.

WARNING The POWER terminals CANNOT be wired backwards. That will destroy the circuit.

WARNING Though the circuit can realistically accept a wider range of voltages than 5-15V, it has not been tested outside of that range. Before powering it with a voltage outside of that range, the data sheets for each of the internal IC's should be consulted to ensure that they can operate safely at those voltages.

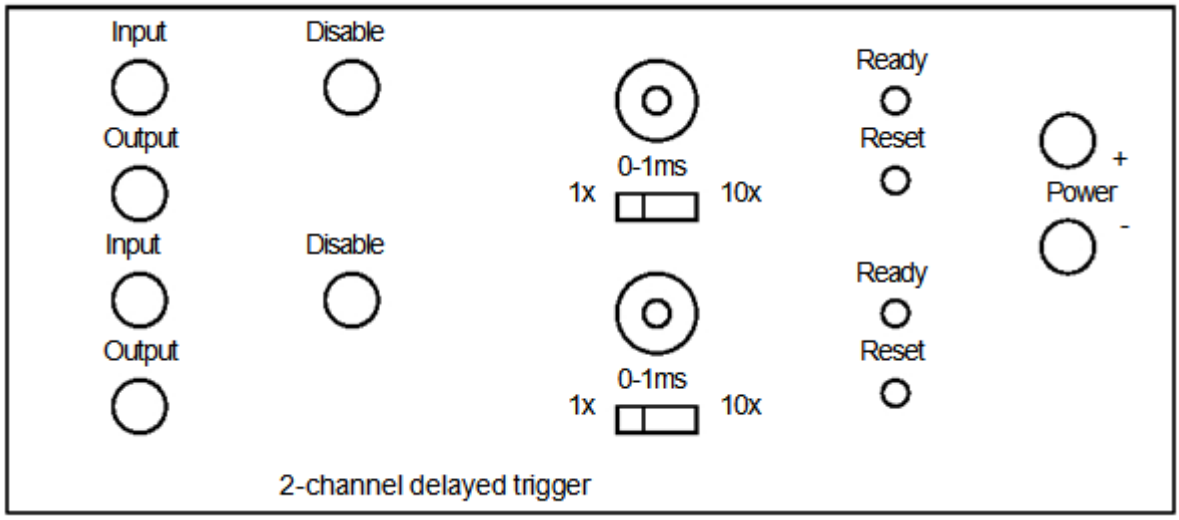

Figure 98. 2-channel delayed trigger front panel.

Operating Principals

Each channel of the 2-channel delayed trigger circuit is driven by two identical circuits. Shown in Figure 97, each channel consists of an R-S flip-flop and two 555 timers with various connecting circuitry and logic.

INPUT DISABLE MODE

The INPUT signal is passed into the circuit through a 10k resistor, after which the signal can be grounded by either of two BJTs (bi-polar-junction transistor). When a Voltage is present on the DISABLE pin, it quickly saturates the BJT to which it is connected, tying the collector to ground. In this mode, the 10k resistor serves as an input impedance to limit the current into the INPUT pin. When the DISABLE pin is not powered, the high-input impedance of the flip-flop draws minimal current, making the 10k resistor irrelevant.

The RESET button performs an identical operation on a separate BJT to disable the INPUT signal while the circuit is being reset.

R-S Flip-Flop

The R-S flip-flop serves as the channel's "memory," to allow only a single trigger. When reset, the nQ (or not-Q) output pin is high. Since the S-pin is connected through a 10k resistor to the INPUT connector, when the INPUT transitions high, nQ toggles high and stays there regardless of the INPUT until the flip- flop is reset. Thus, the R-S flip flop also serves as an inverter because the nQ pin is used rather than the Q pin.

The R-pin is tied directly to the reset switch and a pull-down resistor to prevent accidental resets. Thus, when the reset button is pressed, not only is the INPUT signal disabled, but the nQ pin is toggled high again. Because the nQ pin discharges through the READY LED, the LED will light whenever the flip-flop will toggle on a pulse on the S-pin.

555 Timer A

The first of the two 555 timers is responsible for generating the tunable delay. The 555 timer toggles the OUTPUT pin high when the TRIGER pin transitions below one third the power voltage, and then toggles the OUTPUT low again when the THRESHOLD pin

transitions above two thirds the power voltage. While the OUTPUT pin is low, the DISCHARGE pin is tied to ground via a transistor.

Thus, when the timer is awaiting a trigger input, OUTPUT pin is low and the DISCHARGE pin ties RC circuit to ground. When the TRIGGER pin transitions low, the OUTPUT toggles high, and the DISCHARGE pin is allowed to float. At that instant, current flowing through the potentiometer is allowed to charge the capacitor, and the voltage on the THRESHOLD pin begins to rise. When it reaches two- thirds the supply voltage, the OUTPUT pin will transition low, the DISCHARGE pin will drain the capacitor, and the circuit will be ready for the next trigger event.

The delay is tunable through the 100k potentiometer and the selection of one of the two capacitors. There is a 1k resistor installed to prevent a dead short through the DISCHARGE pin when the potentiometer is at 0-ohms.

The RC circuit buffering the output of the R-S flip-flop and the first 555 allows the initial transition to reach the timer, but is then pulled high by the pull-up resistor with a 0.1ms time constant. This prevents the TRIGGER pin from being low at the same time that the THRESHOLD pin is high at the end of the time cycle. This case results in a-typical operation.

555 Timer B

The second timer circuit is responsible for generating the output pulse. It operates on an identical principal to that of Timer A, only its trigger determines the width of the output pulse; which is not tunable. The OUTPUT pulse width is set to a constant nominal 0.11ms. Similar to the Timer A, the TRIGGER is buffered by an RC circuit, only the time constant is 0.01ms.

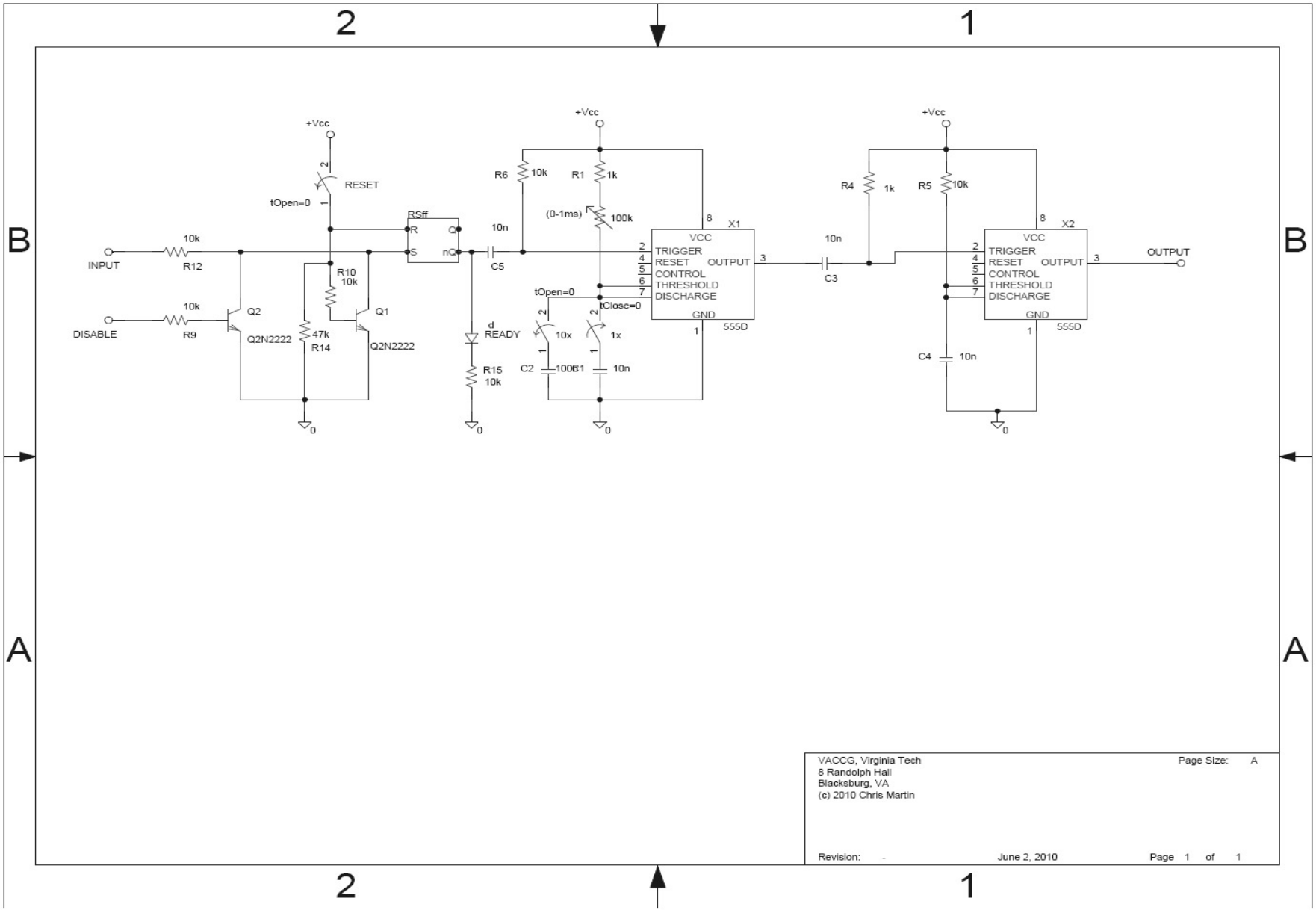

Figure 99. Circuit diagram for flash bulb trigger circuit.